

Electric Field Controlled Synthesis of Carbon Nanotubes

Alexandre Vaz Gamboa Sanches

Thesis to obtain the Master of Science Degree in

Mechanical Engineering

Supervisor(s): Prof. Edgar Caetano Fernandes
Doutora Luísa Maria Leal da Silva Marques

Examination Committee

Chairperson: Prof. Carlos Bettencourt da Silva
Supervisor: Prof. Edgar Caetano Fernandes
Members of the Committee: Prof. Daniel Cardoso Vaz
Prof. Teodoro José Pereira Trindade

December 2019

The author dedicates this report to his mother.

Acknowledgments

The completion of this report would not have been possible without the support of other people.

First and foremost, I would like to thank my research supervisors, Professor Edgar Fernandes and Dr. Luísa Marques, for all the guidance, counselling and trust provided from the start. Their motivation was essential to overcome the difficulties and obstacles that arose during my work. Also, a word of appreciation for the laboratory supervisor Dr. Sandra Dias.

In addition, I also want to say thank you to all my lab colleagues for the companionship and help throughout the realization of this study: Francisco Vaz, Miguel Santos, Miguel Fechado, Mohammad Modarres, and Mafalda Medeiros.

A special thanks to all my close friends that accompanied me during these years at IST. To André Korolev for all the help provided, and to my group of friends "ARM" that made these years feel short, with the most amazing moments and memories. To Inês for all the patience, friendship and extensive motivation demonstrated not only during these months but during the past years.

Finally, without the intensive support of my closest family, my mother, my sister and my grandfather, it would have been impossible to achieve this: Cristina Gamboa, Ana Gamboa and António Gamboa.

This work was developed at the Thermofluids, Combustion and Energy Systems laboratory of the IN+ - Center for Innovation, Technology and Policy Research.

Resumo

Desde a descoberta dos nanotubos de carbono em 1991, o interesse neste material aumentou exponencialmente. Existem alternativas no que toca a métodos de produção, no entanto, são normalmente caros e demorados. A síntese por chamas surgiu como uma alternativa com enorme potencial, uma vez que é energeticamente eficiente, escalável, económica e rápida.

Uma chama de pré-mistura Propano/Ar com co-fluxo de inerte foi utilizada juntamente com um campo eléctrico DC moderado para avaliar o efeito na produção mássica e na morfologia dos CNT sintetizados.

Reynolds de 250, 300 e 400 foram analisados, visto que estes valores permitem uma chama de envelope favorável à produção de nanotubos. Uma chapa de aço inoxidável 303L atuou como substrato.

As medições de massa realizadas levaram à conclusão de que a aplicação de voltagem ao substrato resulta em aumento da produção. Para todas as condições testadas, aplicar 30V ao substrato provou ser a situação ideal para melhorar a produção mássica. Em contrapartida, voltagens negativas não mostraram sinais de ganhos em termos de massa e revelaram alguma inconsistência, com uma evolução mássica exibindo comportamentos diferentes para Reynolds distintos. Concluiu-se também que o diâmetro esperado diminui com a voltagem aplicada e que a atividade catalítica é melhorada.

Medições de temperatura e análise de PIV mostraram que a presença do campo eléctrico não afeta o escoamento da mistura. Adicionalmente, o mecanismo da taxa de crescimento mássico revelou ser idêntico independentemente da presença de E e um modelo analítico monomolecular foi sugerido para o descrever.

Palavras-chave: Nanotubos de Carbono, síntese por chama, campo eléctrico, chama envelope, crescimento mássico, velocimetria de imagem de partículas, chama de pré-mistura.

Abstract

Since the discovery of CNT in 1991, research in this material has risen exponentially. There are several alternatives when it comes to production methods, however, these are generally very costly and time consuming. Flame synthesis emerged as an alternative, seeing that cost-effectiveness is class leading, it is scalable, energy efficient and fast.

A premixed Propane/Air flame with inert co-flow was employed, along with a moderate DC electric field to assess the effect on mass production and morphology of CNT yielded with electric bias.

Reynolds numbers of 250, 300 and 400 were analysed, seeing that these values provide an envelope flame shape favourable towards CNT production. A supported plate of 303L stainless steel acted as the substrate.

Mass measurements were performed, and it was concluded that applying voltage to the substrate results in increase of mass production. For all the conditions tested, applying 30V to the substrate proved to be the optimal situation regarding mass production improvements. On the other hand, negative voltages showed no signs of significant mass gains and revealed some inconsistency, showing different behaviours for distinct Reynolds. It was observed that the expected diameter decreases when voltage is applied to the substrate and that catalytic activity is enhanced.

Temperature measurements and PIV analysis lead to the conclusion that the presence of the electric field does not affect the mixture flow. Moreover, the mechanism of mass growth rate revealed to be similar whether E is present or not and a monomolecular model was proposed for its description.

Keywords: Carbon Nanotubes, flame synthesis, electric field, envelope flame, mass growth, particle image velocimetry, premixed flame.

Contents

Acknowledgments	v
Resumo	vii
Abstract	ix
List of Tables	xiii
List of Figures	xv
Nomenclature	xix
1 Introduction	1
1.1 Motivation	1
1.2 Literature Review	2
1.2.1 Overview	2
1.2.2 Structure of Carbon Nanotubes	3
1.2.3 Properties of Carbon Nanotubes	5
1.2.4 Applications of Carbon Nanotubes	7
1.2.5 Growth Mechanisms of Carbon Nanotubes	8
1.2.6 Methods for Synthesis of Carbon Nanotubes	10
1.2.7 Flame Synthesis	12
1.2.8 CNT Growth Under Electric Field Bias	16
1.3 Objectives	20
1.4 Thesis Outline	20
2 Experimental Setup	21
2.1 Combustion System	21
2.1.1 Bunsen Burner	22
2.1.2 Mass Flow Controllers	23
2.1.3 Combustion Gases	24
2.2 Sampling System	24
2.2.1 Coordinate system	24
2.3 Acquisition System	25
2.3.1 Thermocouple	25
2.3.2 Analytical Balance	25

2.3.3	Camera and Lens	25
2.3.4	Particle Implementation Velocimetry	25
2.4	Electric System	27
2.4.1	Power Supply	27
2.5	Carbon Nanotubes Production	29
2.5.1	Premixed Flame	29
2.5.2	Sample Preparation	29
2.5.3	Electrodeposition of Zinc and Cobalt	29
2.5.4	Working Conditions	31
2.6	Characterization of CNT	33
2.7	Uncertainties	34
2.7.1	Flow Meters	34
2.7.2	Equivalence Ratio	35
2.7.3	Reynolds Number	36
2.7.4	Thermocouple Measurements	36
2.7.5	Mass Measurements	37
2.7.6	Height and Distance	37
2.7.7	Electric Field Equipment	37
3	Results and Discussion	39
3.1	Substrate Analysis	39
3.2	CNT Synthesized Without Electric Field	40
3.3	Electric Field Simulation	42
3.4	Influence of Electric Field on Production of CNT	43
3.4.1	Mass Yield	43
3.4.2	Morphology of CNT	49
3.4.3	Vertical Alignment	56
3.4.4	Time Analysis	56
3.4.5	Deposited Substrates	61
4	Conclusions	63
4.1	Achievements	65
4.2	Future Work	66
	Bibliography	67
A	Velocity Plots	75

List of Tables

1.1	Experimental results for the Young's modulus of MWCNT.	5
1.2	Properties of Carbon Nanotubes compared to other common materials in engineering. Modified from [19]	5
2.1	Experimental conditions to evaluate voltage effect at different Reynolds numbers.	32
2.2	Experimental conditions to evaluate mass yield versus time with electric field bias of 20 and 30 volts.	33
2.3	Uncertainties and relative error for measurements made while using $Re = 250$	34
2.4	Uncertainties and relative error for measurements made while using $Re = 300$	35
2.5	Uncertainties and relative error for measurements made while using $Re = 400$	35
2.6	ϕ uncertainties and relative errors associated.	36
2.7	Re uncertainties and relative errors associated.	36
2.8	Voltage uncertainties and relative errors associated.	37
2.9	E magnitude uncertainties and relative errors associated.	38
3.1	Mass measurements without electric field for $Re=300$	40
3.2	Mass and deposition area measurements without electric field for $Re=250, 300$ and 400 . .	41
3.3	Average magnitude of E for the different voltages applied based on simulation results. . .	43
3.4	Deposition areas calculated for $\pm 1, \pm 10, \pm 20$ and ± 30 volts for a Reynolds number of 250, 300 and 400.	48
3.5	Expected diameters and diameter intervals for $\Delta V=5, 20$ and 30	50

List of Figures

1.1	Carbon Nanotubes production, annual publications and patents issued between 2004 and 2011. Adapted from [2].	1
1.2	Carbon Nanotube formation from graphene sheet. Adapted from [7].	2
1.3	Carbon Nanotube, Carbon Nanofibre and Carbon Fibre. Adapted from [7].	3
1.4	Chirality of CNT, defined by the chiral vector (C_h) and chiral angle (Θ) . Adapted from [9].	3
1.5	Different anatomic types of Carbon Nanotubes: a)Armchair, b)Zig-Zag. Adapted from [9].	4
1.6	Single-Walled and Multi-Walled Carbon Nanotubes. Adapted from [11].	4
1.7	Growth mechanisms for CNT: (a) tip-growth model, (b) base-growth model. Adapted from [41].	9
1.8	Arc-Discharge method for CNT synthesis. Adapted from [51].	11
1.9	Laser Ablation method for CNT synthesis. Adapted from [51].	11
1.10	Chemical Vapour Deposition method for CNT synthesis. Adapted from [19].	12
1.11	Flame synthesis of CNT. a) Premixed Flame b) Counter-flow Diffusion Flame c) Co-flow diffusion flame d) Inverse diffusion Flame. Adapted from [19].	12
1.12	Electrostatic force acting on CNT. Adapted from [55].	17
1.13	Electric field effect on the morphology of synthesized CNT. Adapted from [86].	18
1.14	Electrostatic forces acting on CNT and catalyst particles. Adapted from [88].	19
2.1	Combustion system schematic.	21
2.2	Real experimental setup.	22
2.3	CAD model of the Bunsen burner.	22
2.4	Outlet nozzle drawing.	23
2.5	Flame coordinates (r, z) in millimetres. The coordinates for each point (r,z) are: A(0,10), B(5,10), C(10,10), D(15,10), E(20,10), F(25,10)	24
2.6	Type R thermocouple used for measurements.	25
2.7	PIV experimental setup.	27
2.8	DC Power supply and oscilloscope.	28
2.9	Real setup for the electrodeposition of the zinc and cobalt materials on the substrate. . .	30
2.10	Real image of the stainless steel plate after cobalt electrodeposition.	31
2.11	Envelope flame shape adopted for this work.	31

3.1	Result of the X-ray diffraction of the stainless steel substrate.	39
3.2	SEM image of the stainless steel substrate.	40
3.3	SEM image at 10K magnification of CNT produced without electric field and respective normal distribution of the diameters.	41
3.4	Binarized photographs of deposited substrates for the different Re and 0V. The black areas correspond to deposited CNT.	41
3.5	Result of the X-ray diffraction of the carbon nanotubes produced.	42
3.6	Mass measurements for production of carbon nanotubes with ± 1 , ± 10 , ± 20 and ± 30 V, for a Re number of 250.	43
3.7	Mass measurements for production of carbon nanotubes with ± 1 , ± 10 , ± 20 and ± 30 V, for a Re number of 300.	44
3.8	Mass measurements for production of carbon nanotubes with ± 1 , ± 10 , ± 20 and ± 30 V, for a Re number of 400.	45
3.9	Binarized photographs of deposited substrates for the different voltages and $Re=250$. The black areas correspond to deposited CNT.	46
3.10	Binarized photographs of deposited substrates for the different voltages and $Re=300$. The black areas correspond to deposited CNT.	47
3.11	Binarized photographs of deposited substrates for the different voltages and $Re=400$. The black areas correspond to deposited CNT.	47
3.12	SEM image and diameter distribution for 5V.	49
3.13	SEM image and diameter distribution for 20V.	50
3.14	SEM image and diameter distribution for 30V.	50
3.15	Locations for temperature measurements. The coordinates for each point (r,z) are: A(0,10), B(5,10), C(10,10), D(15,10), E(20,10), F(25,10).	52
3.16	Temperatures measured at the six different locations with 0V, 20V and 30V applied to the substrate.	53
3.17	2D velocity map for the flow characterized by Reynolds number of 300 and 0, 30 and -30 V.	54
3.18	Velocity plots near the substrate for 0V, 30V and -30V.	55
3.19	Mass measurements vs sampling time for 0, 20 and 30V.	57
3.20	Normalized mass measurements vs sampling time for 0, 20 and 30V.	59
3.21	Fitment of the monomolecular analytical model to the results obtained in the experiments.	60
3.22	SEM image of Cobalt deposited substrate after flame exposure with 1K magnification.	61
3.23	SEM image of Cobalt deposited substrate after flame exposure with 5K magnification.	62
A.1	2D velocity plot obtained from PIV for 1V.	75
A.2	2D velocity plot obtained from PIV for 10V.	75
A.3	2D velocity plot obtained from PIV for 20V.	76
A.4	2D velocity plot obtained from PIV for -1V.	76
A.5	2D velocity plot obtained from PIV for -10V.	76

A.6	2D velocity plot obtained from PIV for -20V.	77
-----	--	----

Nomenclature

Symbols

ΔH_{fusion} Latent heat of fusion.

ΔV Voltage.

\dot{m} Mass flow rate.

τ Initial time.

a_1, a_2 Unit vectors.

A_{burner} Area of the section at the burner outlet.

C_h Chiral vector.

D_{burner} Diameter at the burner outlet.

E Electric field.

e_i Relative error.

F_e Electrostatic force.

F_{AF} Axial force.

F_{TF} Tangential force.

h Distance between electrodes.

k Reaction rate.

q Charge.

Q_i Volumetric flow rate.

Re Reynolds number.

T Temperature.

U_i Uncertainty.

V Velocity.

x_i	Mole fraction.
m	Mass.
m*	Normalized mass.
t	Time.
t*	Normalized time.

Greek symbols

2θ	Scattering angle.
α	Asymptotic final mass growth constant.
λ	Wavelength.
μ	Dynamic viscosity.
ϕ	Equivalence ratio.
ρ	Density.
ρ_l	Density of the liquid metal.
ρ_s	Density of the solid metal.
σ_l	Surface energy of the liquid.
σ_{sl}	Solid-liquid interfacial energy.
Θ	Chiral angle.
θ	Carbon nanotube deviation angle.

Subscripts

s	Solid state.
m	Measured value.
max	Maximum.
mix	Mixture.
st	Stoichiometric.
total	Total.

Superscripts

air	Atmosphere at sea level.
-----	--------------------------

Chemical Species

γ -Fe	Austenite.
Ar	Argon.
C ₂ H ₂	Acetylene.
C ₂ H ₄	Ethylene.
C ₃ H ₈	Propane.
CH ₄	Methane.
CO	Carbon monoxide.
Co	Cobalt.
CO ₂	Carbon dioxide.
CoCl ₂	Cobalt chloride
Cr	Chromium.
Fe	Iron.
H ₂	Hydrogen.
H ₂ O	Water.
Li	Lithium.
N ₂	Nitrogen.
NaCl	Sodium chloride
NH ₃	Ammonia.
NH ₄ Cl	Ammonium chloride
Ni	Nickel.
O ₂	Oxygen.
Pt	Platinum.
Rh	Rhodium.
Si	Silicon.
Zn	Zinc.
ZnCl ₂	Zinc chloride

Acronyms

1D	One-dimensional.
----	------------------

2D	Two-dimensional.
3D	Three-dimensional.
AAO	Anodic aluminum oxide.
AD	Arc discharge.
AFM	Atomic force microscope.
C60	Buckminsterfullerene.
CAD	Computer aided design.
CDF	Counter diffusion flame.
CF	Carbon Fibres.
CNF	Carbon nanofibres.
CNT	Carbon nanotubes.
CVD	Chemical vapor deposition.
DC	Direct current.
EDS	Energy dispersive spectrometer.
FPM	Floating probe mode.
GPM	Grounded probe mode.
HAB	Height above burner.
IA	Interrogation area.
IDF	Inverse diffusion flame.
LA	Laser ablation.
LPM	Liters per minute.
MWCNT	Multi-walled carbon nanotubes.
NDF	Normal diffusion flame.
PIV	Particle implementation velocimetry.
SEM	Scanning electron microscopy.
SS	Stainless steel.
SWCNT	Single-walled carbon nanotubes.
TEM	Transmission electron microscopy.

VLS Vapour liquid solid.

VSS Vapour solid solid.

XRD X-ray diffraction.

Chapter 1

Introduction

1.1 Motivation

Nanoscience and nanotechnology have emerged in the last decade as a promising area, opening a wide spectrum of technologies and applications to the world of science and engineering. The estimations available expect that this sector will be valued at 125 billion USD by the year 2024 while still following an increasing tendency. Between the years 2000 and 2015, investment in nanotechnology related research worldwide reached the 250 billion USD mark [1].

Carbon Nanotubes (CNT) are amongst the most promising novel nanomaterials with a wide collection of applications. Therefore, it comes as no surprise that investigation in the field of CNT is raising and of great relevancy. In the period between 2004 and 2011 the annual publications issued worldwide tripled as visible in Figure 1.1, however, the knowledge and technical understanding related to growth control of carbon nanotubes in bulk and large scale applications is still a hurdle to overcome [2].

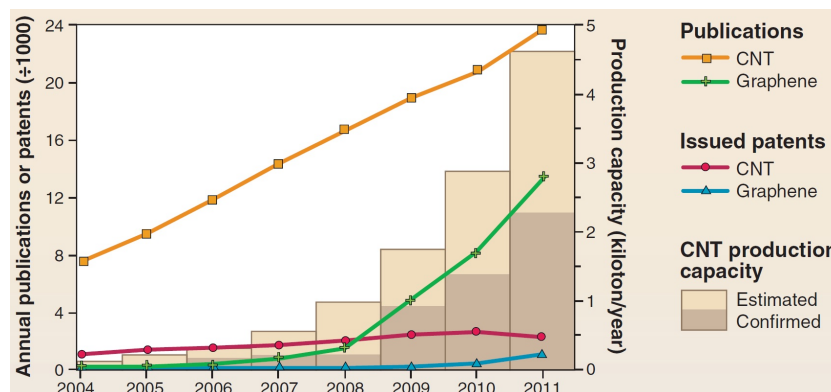


Figure 1.1: Carbon Nanotubes production, annual publications and patents issued between 2004 and 2011. Adapted from [2].

There are a few methods currently available for production of carbon nanotubes with different characteristics such as Chemical Vapour Deposition (CVD), Laser Ablation (LA), Electric Arc Discharge (AD) and Flame Synthesis. It is of utmost importance to refer that the first three methods mentioned have one drawback in common, an external source of energy has to be present, therefore, making them costly

processes. Fuel synthesis appears amongst the methods mentioned as a novelty, nonetheless, production of CNT through this method has tremendous potential. The flame environment provides an ideal scenario while being cost and energy efficient, scalable and a continuous process [3].

Controlling and understanding the growth process of CNT is important to definitely establish flame synthesis as an accredited production method. The application of an electric field has emerged as a possibility to enhance the quantity and the properties of the yielded products, meaning that the actuation and details of this method require research.

1.2 Literature Review

1.2.1 Overview

In 1985, Smalley and colleagues established the chemistry of fullerenes [4]. Fullerenes can be defined as geometric 3D structures, composed of carbon atoms, with hexagonal and pentagonal faces. C60 (buckminsterfullerene) was the first of these closed molecules to be disclosed. This discovery set the trend for carbon nanomaterials such as carbon nanotubes, first observed by Ijima in 1991 [5].

Carbon hybridization is very important for the morphology of carbon structures. A sp^3 configuration, where the four valence electrons are evenly shared, results in the well-known diamond isotropic structure. However, when only three of the valence electrons are shared, the bonding assumes a sp^2 configuration, which results in graphene. Graphene is a type of carbon structure whose morphology was only described theoretically at first and was thought to be impossible to synthesize. However, in 2004 Konstantin Novoselov, Andre Geim and their collaborators were able to isolate a single layer of carbon atoms arranged in a honeycomb lattice [6]. Carbon nanotubes can be visualized as graphene sheets that rolled themselves into a tube shape, somewhat resembling an elongated C60, as visible in Figure 1.2.

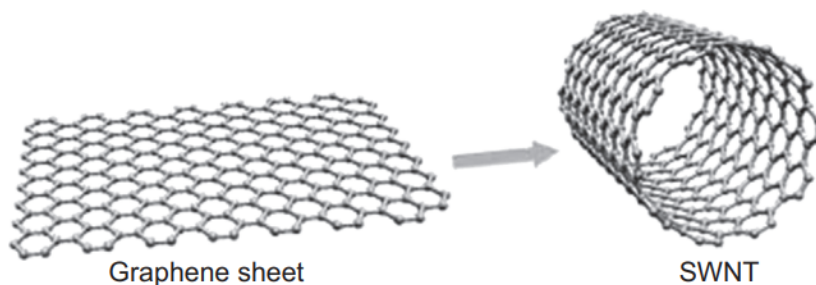


Figure 1.2: Carbon Nanotube formation from graphene sheet. Adapted from [7].

There are different structures of CNT, but mainly and sufficiently for our work we can divide them into Single Walled Carbon Nanotubes (SWCNT) and Multi Walled Carbon Nanotubes (MWCNT) which together account for 80% of the publications disclosed between 2000 and 2010 [8].

Carbon nanofibres (CNF) are other form of nanostructures with higher diameters (around 100 nm), with a slightly different structure than carbon nanotubes. These started to be synthesized as an alternative to the expensive carbon fibres found in composites due to their great mechanical, electrical and thermal

properties. Properties however that are inferior to those of carbon nanotubes [7]. CNT and CNF along with their characteristic diameters are visible in Figure 1.3.

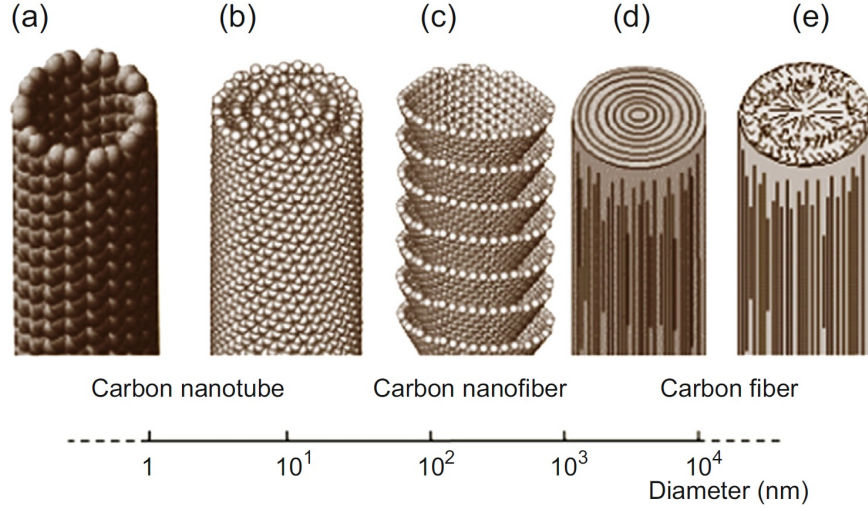


Figure 1.3: Carbon Nanotube, Carbon Nanofibre and Carbon Fibre. Adapted from [7].

1.2.2 Structure of Carbon Nanotubes

The anatomic structure of CNT is described by their chirality, which in turn is defined by two variables. The first one is the chiral vector (C_h) and the second is the chiral angle (Θ), both visible in Figure 1.4.

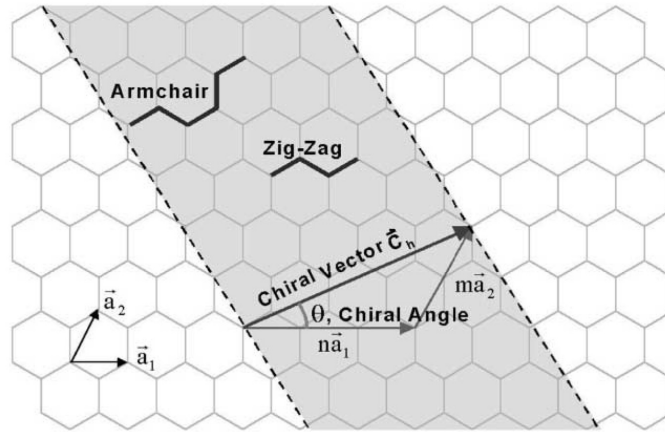


Figure 1.4: Chirality of CNT, defined by the chiral vector (C_h) and chiral angle (Θ). Adapted from [9].

The vector C_h can be interpreted in Figure 1.4 as a perimeter of the nanotube, rolled in a way that the dotted lines coincide, so that the tip touches the tail. Different chiral orientations, i.e different Θ , lead to different CNT geometries. The vector is mathematically defined by Equation 1.1.

$$C_h(n, m) = na_1 + ma_2 \quad (1.1)$$

The integers n and m account for the number of steps along the carbon bonds of the hexagonal pattern, with a_1 and a_2 representing unit vectors. The chiral angle (Θ) is measured from the unit vector

a_1 to the chiral vector and determines the amount of twist in the carbon nanotube. Its value is given by Equation 1.2.

$$\Theta = \arcsin \frac{\sqrt{3m}}{2(n^2 + nm + m^2)} \quad (1.2)$$

Based on the variables mentioned before, carbon nanotubes can be classified as one of three different types, two of those represent the limit scenarios when the chiral angle is 0 and 30 degrees. These limits are perfectly adequate due to the honeycomb hexagonal symmetry. If the indices are equal ($n = m$) the nanotube is called armchair (Figure 1.5a) and the chiral angle is 30°. On the other hand, if m is zero the nomenclature is zig-zag (Figure 1.5b) with the chiral angle being 0°. In all other cases with ($n \neq m$), the nanotubes are named chiral and the angle lies in the interval between 0 and 30 degrees [10].

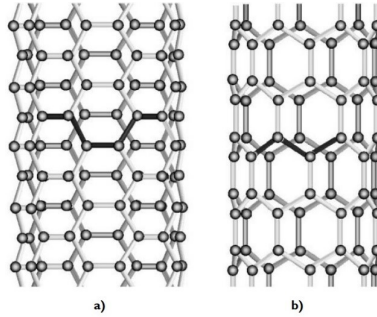


Figure 1.5: Different anatomic types of Carbon Nanotubes: a)Armchair, b)Zig-Zag. Adapted from [9].

As mentioned before, beyond the anatomic classification, CNT are also divided into SWCNT and MWCNT. The former consists of a single layer of graphene forming a hollow cylinder, usually with diameters in the order of 1 nm. MWCNT are the most common and effortlessly synthesized. These consist of several concentric layers of hollow cylinders with a separation between tubes similar to the inter-planar distance observed in graphite (0.34 nm). The diameters of these nanotubes range from 2 to 100 nm. SWCNT are highly sought after due to exceptional properties [11]. Both types are clearly represented in Figure 1.6.

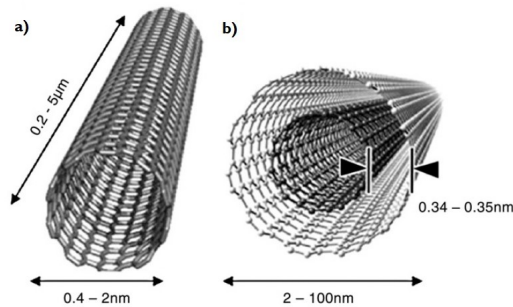


Figure 1.6: Single-Walled and Multi-Walled Carbon Nanotubes. Adapted from [11].

1.2.3 Properties of Carbon Nanotubes

Production of CNT has maintained an yearly increase rate of 60% for over 10 years [12] and the projections point to a total market value of 8 billion USD in 2024 [13]. The reason behind this are the exceptional properties that CNT possess and inherently the significant expectations those properties bring along.

Mechanical Properties

Being very pure carbon structures, excellent mechanical properties of carbon nanotubes derive from the C-C bond between atoms. Specifically because of their sp² hybridisation, the strength and stiffness CNT have exhibited are above any material tested before. Several values have been reported from both theoretical and experimental models. The first experimental measurements were performed by Treacy et al. [14] on MWCNT. By evaluating the amplitude of the nanotubes intrinsic thermal vibrations inside a transmission electron microscope (TEM), extrapolation of values for the Young's modulus was possible. Values between 0.41 and 4.15 TPa were reported, being the average 1.8 TPa. Direct measurements were pioneered by Wong et al. in 1997 [15] through the use of an atomic force microscope (AFM). Studying MWCNT pinned at one end resulted in an average value for the Young's modulus of 1.28 TPa. The most remarkable research regarding CNT mechanical properties was carried out by Yu et al. [16] in 2000. For the first time the mechanical properties of individual MWCNT were evaluated under tensile stress inside a scanning electron microscope (SEM). Their results concluded that tensile strengths range from 11 to 63 GPa while the Young's modulus is in the interval between 270 and 950 GPa. Giving sequence to their initial work, Yu and his colleagues determined the same properties for SWCNT, obtaining strengths stretching between 13 and 52 GPa and Young's modulus of 320-1470 GPa [17]. However, in the radial direction CNT are rather soft compared to the axial direction. Minari et al. [18] demonstrated nevertheless that CNT have remarkable ability to undergo reversible radial deformation. Table 1.1 compiles the previous results and Table 1.2 compares properties of CNT with other materials.

Table 1.1: Experimental results for the Young's modulus of MWCNT.

Year	Method	Young's Modulus [TPa]
1996	Thermal Vibrations – TEM	0.4-4.15 (avg 1.8)
1998	Thermal Vibrations – TEM	0.9-1.7 (avg 1.25)
1999	AFM, both ends clamped	0.8 ± 0.41
2000	Tensile test	0.27-0.95

Table 1.2: Properties of Carbon Nanotubes compared to other common materials in engineering. Modified from [19]

Material	Young's Modulus (GPa)	Tensile strength (GPa)	Electrical Resistivity ($\sigma.m$)	Thermal Conductivity (W/m.K)
SWCNT	320-1470	13-52	10^{-6}	>200
MWCNT	≈ 1000	11-63	$0.1 \cdot 10^{-3}$	>3000
Diamond	1000	1.2	$1 \cdot 10^{-12}$ to $1 \cdot 10^{-14}$	1000-2600
Steel (carbon low alloy)	200	0.4	$12 \cdot 10^{-8}$ to $170 \cdot 10^{-8}$	43
Copper	110	0.207 (Hard Drawn)	$1.7 \cdot 10^{-8}$ to $2.65 \cdot 10^{-8}$	390

Electrical Properties

CNT possess quite unique electrical properties allowing them to be remarkable conductors. Researchers have demonstrated that chirality, defects, degree of crystallinity and diameter strongly affect their electronic characteristics [20, 21]. The theory behind electronic band structure predicts that SWCNT can be either metallic or semiconductors (with very low energy gaps) according to the n and m integers. While metallic SWCNT are classified as quantum wires, that is not the case for MWCNT. These are complex in structure and composed of multiple SWCNT with different properties making their analysis difficult. Metallic CNT are able to transport an electric current with density of $4 \cdot 10^9$ (A/cm²), a value 1000 times higher than the one for copper [22].

Thermal Properties

Carbon nanotubes exhibit excellent properties along their tube and thermal characteristics are no exception. Direct measurements at nanoscales are hard to achieve, thus many of the results available derive from theoretical simulations or indirect experiments. Usually, the thermal conductivity reported for CNT ranges between 2000 and 6000 W/m.K [23]. For SWCNT, Yu et al. [24] examined the thermal conductivity on isolated SWCNT grown by vapour deposition, claiming a value greater than 2000 W/m.K. Hone et al. [25] performed analysis on mats of SWCNT, obtaining values in the interval between 1750 and 5800 W/m.K. Berber et al. [26] evaluated thermal conductivity and its temperature dependence for SWCNT. At room temperature the value indicated is 6600 W/m.K, with this value increasing for lower temperatures, allegedly 37000 W/m.K at 100K. Regarding MWCNT, Kim et al. [11] found that the thermal conductivity at room temperature was over 3000 W/m.K for individual MWCNT. Other experiments show values ranging between 200 and 3000 W/m.K, with lower conductivities for bulk and tangled MWCNT due to high resistivity induced by contact between tubes [23].

Chemical Properties

Graphite is known to be one of the most stable and inert materials. However, CNT have their reactivity enhanced mainly because of topological defects such as the pentagonal structures observed in the tips of the CNT. This defect accentuates the curvature of the carbon nanotube thus improving reactivity. When oxidation occurs, the tip is in fact etched leaving the CNT with open ends [27, 28]. This means that CNT can be filled relatively easy, providing an excellent carrier. Functionalization of CNT can also be highly valuable. This can be achieved either by covalent or non-covalent binding, with the intent of developing excellent carbon nanotube based materials or the use of solubilized carbon nanotubes as a starting point for further modifications [29].

1.2.4 Applications of Carbon Nanotubes

Given the excellent properties described above, there is a multitude of applications for carbon nanotubes.

Perhaps one of the most popular is the use of CNT as fillers in order to create nanocomposites so that the mechanical, electric and thermal properties of the matrix material are improved. The most common material for a matrix is a polymer and multiple studies have been conducted. Qian et al. [30] synthesized a nanocomposite by adding 1 wt.% of MWCNT to polystyrene. Testing of the material through tensile tests and verification of the nanotube loading by in situ TEM was performed. From the data it could be extrapolated that elastic modulus and break stress increased between 36-42% and 25%, respectively. Increasing the concentration of carbon nanotubes past a critical point can, however, decrease the properties of the matrix material. The dispersion and alignment of the filler is very important, with the formation process having high impact on the overall effects. A homogenous dispersion provides good spread of filler material and better load distribution, ultimately granting better properties [31]. Velasco-Santos et al. [32] integrated 1 wt.% of MWCNT into a polymer matrix by in situ polymerization rather than mixing by other methods and achieved an outstanding 1135% increase in the storage modulus of the material.

Other application for CNT is in electronic equipment as field-emission sources. Because of the curved pentagon tips of carbon nanotubes, emission of electrons from the tips is easy [33]. Therefore, the use of CNT to produce flat-panel displays, intense light sources, lamps and x-ray sources is possible and beneficial, as there is not only an increase on the lifetime of components, but also allows high current densities and low emission thresholds [34].

Other use found for carbon nanotubes is to improve lithium ions batteries. Through the intercalation of lithium ions within carbon nanotubes, high irreversible capacities can be achieved. Furthermore, the loss of efficiency characteristic of lithium-only batteries can be avoided [35].

Owing to their large surface area and high electrical conductivity, CNT are the perfect candidates for use as supercapacitors and actuators. Supercapacitors of CNT are used in applications that require both high power and high capacity, such as the electric systems of hybrid vehicles providing fast acceleration and storage of energy while braking. Power densities are in the order of 20 kW/Kg and energy densities of 7 Wh/kg. Regarding the actuators, the leading characteristic of using carbon nanotubes is the ability to maintain efficiency at high temperatures [34].

Other potential application for carbon nanotubes is as sensors. Collins et al. [36] stated that SWCNT possess extreme sensitivity to air and vacuum conditions due to experiencing ample variations in their electrical resistance. Also, they claim that MWCNT can sense the presence of gases such as NH_3 , H_2O , CO_2 and CO . This means they can be used as leak detectors in chemical plants for instance.

Their hollow structure allows them to be employed as gas or metal containers. Several processes have been tested for the introduction of metals, metal carbides and oxides into CNT [34]. Also, storage of Ar and H_2 inside carbon nanotubes seems to be possible. The possibility of accumulating hydrogen in CNT [37, 38] could be useful for fuel cells, however, further testing must be conducted as the uptake levels are not yet clear.

CNT have also been employed as scanning probe tips, providing better image quality [39] and in other

areas such as medicine, being used as novel and efficient drug carriers [40].

1.2.5 Growth Mechanisms of Carbon Nanotubes

For a system to be capable of synthesizing carbon nanotubes there are three compulsory components [19]: (i) source of carbon, (ii) source of heat and finally (iii) metal catalytic particles.

When it comes to the growth mechanism of this relatively recent material there is yet to be consensus and absolute certainty as of how it all occurs. Despite this, the most accepted general mechanism has the following outline [41].

As the vaporous hydrocarbon contacts the hot catalyst metallic particles it decomposes to form hydrogen and a carbon species. The former remains as vapour in the environment, but the latter gets dissolved into the metal. When the solubility limit for the catalytic metallic particle is reached at that specific temperature, the dissolved carbon precipitates towards the outside and crystallizes in an energetically stable cylindrical configuration. Hydrocarbon decomposition, being an exothermal reaction, releases heat which in turn is consumed in the crystallization process. Therefore, these thermal gradients keep the process continuous.

From this point the growth follows one of two possibilities widely reported in the literature. If the interaction between substrate and the metal catalyst is weak, upon hydrocarbon decomposition, carbon diffuses through the metal and crystallizes on the bottom of the particle, effectively lifting the particle from the substrate. As long as the top surface of the metal is clear and there is a sufficient concentration gradient to sustain diffusion, the carbon nanotube will continue to grow. Once the surface is fully covered and no diffusion occurs, the catalytic site is said to be deactivated and growth ceases. This is recognised as the “tip growth model”.

On the opposite hand, if the interaction between the substrate and the metal particle is strong, hydrocarbon decomposition and diffusion initially occur as in the method above, however, precipitation fails to lift the metal particle from the substrate. The precipitation tends to emerge from the particle base onto the farthest section from the substrate and at first carbon crystallizes as a hemispherical dome. This structure then grows as a graphitic cylinder. Subsequent hydrocarbon decomposition takes place on the lower outer surface of the metal catalyst and dissolved carbon diffuses in an upward direction. This model is named “base growth model”. Both alternatives are depicted in Figure 1.7.

Regarding the general method described above there are a few points which cause debate. There is no certainty about the physical state of the metal, liquid or solid, whether the catalyst is the pure metal or metal carbide, the details of the diffusion process, etc. The first one is briefly discussed below.

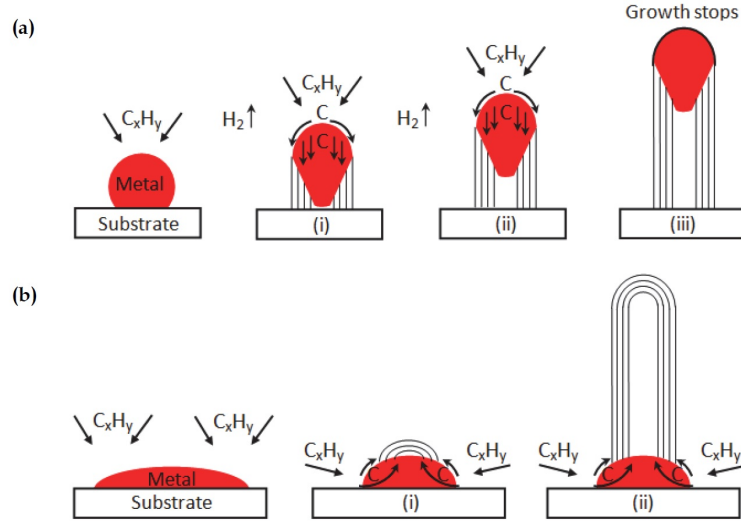


Figure 1.7: Growth mechanisms for CNT: (a) tip-growth model, (b) base-growth model. Adapted from [41].

Physical state of the metal catalyst:

Baker et al. [42] was the first to observe carbonaceous fibres growth in-situ. For acetylene that decomposed on a nickel catalyst at 600°C it was clear that the metal particle changed its shape throughout the growth process. This led to the conclusion that the metal catalyst should be in liquid phase. Moreover, the activation energy of carbon decomposition in liquid nickel was coincident with the activation energy calculated for the growth process, meaning that carbon diffuses through bulk metal and the process is controlled by diffusion. Resemblances to this tip growth model were achieved when using Fe, Co and Cr catalysts again by Baker et al. [43].

However, when the same acetylene was used with a binary alloy (Pt-Fe) the catalyst was observed to remain static on the substrate and with no change in shape. This led to the development of the base growth model [44]. Later others reported the same base growth mechanism for Fe and Co catalysts [45, 46].

In 1984, Tibbets [47] not only explained the cylindrical shape assumed by crystalline carbonaceous fibres but also suggested a vapour-liquid-solid (VLS) method, firstly introduced for other materials, to explain the growth mechanism of CNT. Still, this model raises serious doubts especially because of the high melting points of the catalyst metals when compared to the temperature of synthesis. It is proven that the melting point of particles below 10 nm falls severely. The reduction in melting temperatures for nanoscales combined with the exothermic decomposition reaction leads to a general lean in favour of the liquid phase model, particularly for SWCNT. When the concern are MWCNT, the catalytic particles on which they are based tend to be of bigger dimensions than those for SWCNT (>20 nm) which in turn suggests the particles can not be in liquid phase at synthesis temperatures. Thus, the most probable model for MWCNT synthesis is the vapour-solid-solid (VSS). Therefore, it is likely that the growth mechanism differs according to the type of CNT formed and thus, the experiment conditions [41].

Solid Carbon Formation

Along with the growing mechanism, it is very important to understand the reactions that culminate in the appearance of solid carbon. There are three equations that explain this process. The cracking equation [48], Equation 1.3, that demonstrates the decomposition of the precursor hydrocarbon, the reduction equation [49], Equation 1.4, and finally the Boudouard equation [49], Equation 1.5.



Between these three equations there is no clear definition which one is the primary source of carbon. Several studies claim that both Equation 1.4 and Equation 1.5 are the primary sources of carbon, meaning that CO has a fundamental role in the deposition of CNT [49, 50]. Particularly, Olsson and Turkdogan [50] concluded that, for CO-H₂ flames, the concentration of Hydrogen was determinant for the rates of both the reduction and Boudouard reactions. However, the results available in the literature depend on temperature, precursor and catalyst used, without a clear consensus.

1.2.6 Methods for Synthesis of Carbon Nanotubes

CNT can be synthesized by several methods. Despite the basis of this work being flame synthesis, a brief description of alternative methods along with useful references is presented.

Arc-Discharge

Ijima first found MWCNT using an arc-discharge (AD) method [5]. This method is regarded as the simplest in terms of nanotubes synthesis. Also the products reveal less structural defects when compared to other low temperature methods such as Chemical Vapour Deposition (CVD) [51]. The resulting CNT require subsequent purification and thus the process is renowned as unsuitable for industrialized and mass production.

The arc discharge method involves the formation of high temperature plasma from the electrical breakdown of a gas. Two electrodes are used, the anode and the cathode. Usually, the anode is filled with carbon precursors along with catalytic particles. The cathode consists of a pure graphitic rod. When power supply is turned on, a stable arc is formed and high temperature plasma (resultant of inert gas that fills the chamber) sublimates the carbon precursors, which in turn drift towards the anode where cooling occurs and carbonaceous products are formed, including CNT. A schematic for the understanding of the mechanism is shown in Figure 1.8 and an extensive review on the method along with citations of the most important work involving AD can be found in the work done by Arora and Sharma [52].

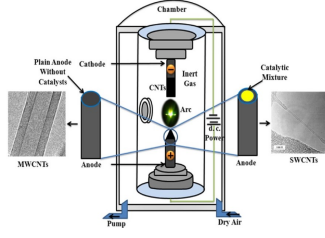


Figure 1.8: Arc-Discharge method for CNT synthesis. Adapted from [51].

Laser Ablation

With the intent to produce pure and uniform SWCNT, Laser Ablation (LA) was first introduced by Guo et al. [53] and uses a light source, a laser, to synthesize CNT. Laser vaporization grants greater control on the growth process as well as higher purity levels. In fact, LA is capable of producing SWCNT of 90% purity [51]. Despite the undeniable superiority of the resulting CNT, LA is a very costly process and goes beyond the quality required for most applications. A schematic of LA synthesis is presented below, Figure 1.9, and for a profound analysis of the process the work of Das et al. [51] is recommended. The physics behind LA are explained, as well as the reigning variables and its effects.

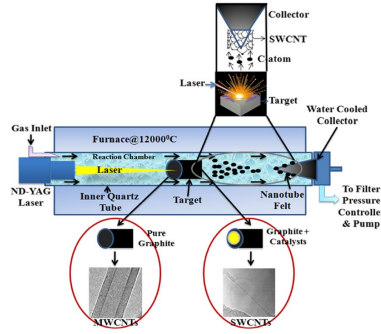


Figure 1.9: Laser Ablation method for CNT synthesis. Adapted from [51].

Chemical Vapour Deposition

Chemical Vapour Deposition (CVD) is an ancient process used to produce carbon microfibres and filaments. This technique involves the decomposition of a hydrocarbon vapour flowing through a reactor where a catalytic material at high temperature is held. It was in 1996 that CVD established itself as a reliable process to produce CNT in large quantities [54].

Hence, and associated with the relatively low price, CVD accounts for most of the CNT available in the world's market [55]. There are several types of CVD and their classification derives from the energy source used.

Despite the high yield, CVD produces relatively low quality CNT. Intense investigation is being carried out in order to improve quality and gain further knowledge on this technique. Again, a schematic is available below, Figure 1.10, and for further insight on CVD, Shah and Tali [56] wrote an extensive review on this technique.

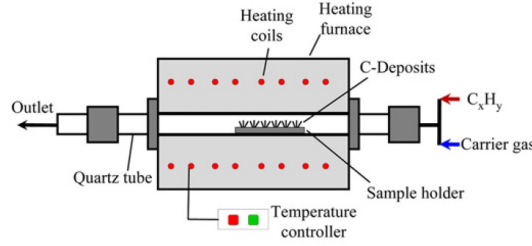


Figure 1.10: Chemical Vapour Deposition method for CNT synthesis. Adapted from [19].

1.2.7 Flame Synthesis

Production of carbon nanotubes using flames is a rather unusual method when compared to those listed above. It has been used to produce CNT for commercial purposes as it is a continuous process that can be readily exploited for large quantity production.

Contrarily to AD, LA and CVD, fuel synthesis does not use an external source of heat, hence the enormous interest it has generated. Through combustion of rich hydrocarbon flames, both the carbon precursors and heat sources are obtained inexpensively. Fundamentally, raising the efficiency while reducing production costs is essential for the future of CNT. Flame synthesis has shown great potential to become the ideal synthesis process even though further research is required to control the synthesized products.

The first tube shaped carbon structures observed by flame synthesis date to 1958 [57]. CNT can be synthesized using different types of flames. The literature focuses on the following ones: premixed flames, normal diffusion flames, counter flow diffusion flames, co-flow diffusion flames and inverse diffusion flames. The different flame types are available in Figure 1.11.

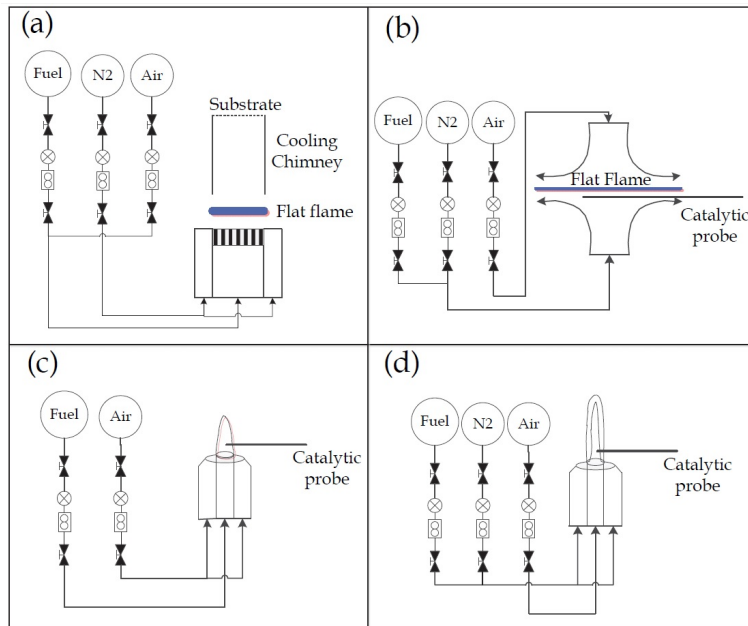


Figure 1.11: Flame synthesis of CNT. a) Premixed Flame b) Counter-flow Diffusion Flame c) Co-flow diffusion flame d) Inverse diffusion Flame. Adapted from [19].

Premixed Flames

In a premixed flame, oxidizer and fuel are mixed prior to ignition. These flames offer the following advantages when compared to diffusion flames:

- 1- Variety of fuels;
- 2- Adjustability of the reaction gases stoichiometry, allowing for greater flame control;
- 3- Flame temperature more freely controlled;
- 4- The burner system allows for good scalability;
- 5- Continuous/Multi-staged process.

Howard et al. achieved production of MWCNT in 1994 using very rich (sooting) premixed flames of different fuel types [58]. By this time there was specific interest in producing single walled carbon nanotubes and in the year 2000 Diener et al. achieved synthesis of SWCNT with premixed ethylene and acetylene flames, while claiming the unsuitability of benzene for SWCNT production [59].

It was in the early 2000s that Vander Wal et al. conducted substantial and detailed studies on the formation of CNT using premixed hydrocarbon flames [60–64]. In their first studies a pyrolysis flame, resultant of inert gas, catalyst particles and reactant gases (CO , H_2 and C_2H_2), heated by a pre-mixed hydrocarbon flame was tested. A significant variety of hydrocarbon fuels (e.g. methane, ethane, propane and ethylene) and metallic additives were tested. The effects on resultant CNT caused by reactant gas composition and flow was studied and important remarks on the role of H_2 and CO in nanotube synthesis were discussed. Different methods for introducing catalytic particles into the flame environment were also approached.

When using premixed flames directly aimed at a supported catalyst Vander Wal et al. achieved a synthesis temperature of 1100K with an ethylene flame. Through variation of the equivalence ratio (ϕ) the authors observed an increase in yield with increase in ϕ . Values started at $\phi=1.37$ with no production of CNT, and went to $\phi=1.82$ where, although there was synthesis of CNT, their morphology started to show defects. $\phi=1.62$ was found to be the optimum point [64].

More recently, Height et al. in 2004 [65] investigated parameters such as growth zone, time scales and structures of the CNT, under various operating conditions using a premixed flame of acetylene, oxygen and 15 mol% argon while using $\text{Fe}(\text{CO})_5$ as a catalyst. The conclusion was that CNT were synthesized between 40 and 70 mm above the burner with ϕ between 1.5 and 1.9, with better results near the bottom of the equivalence ratio window. They also determined with XRD (X-ray diffraction) analysis that the metal oxides were essential for carbon nanotubes formation.

One year after, Nakazawa and his colleagues [66] achieved production of MWCNT using an impinging premixed flame of ethylene and nitrogen as an inert. They described their deposition area as an annular ring coincident with where the unburnt gases were located. The important conclusion drawn from their experiments is the suitability of this method for mass production of carbon nanotubes. Later, Woo et al. followed the same route using a double faced wall stagnation flow (impinging on both sides). Again, the method was found to be eligible for mass production of MWCNT.

In 2017, Chong et al. [67] studied the formation of carbon nanotubes using a propane rich premixed flame. The objective was to study the morphology of CNT yielded when varying the equivalence ratio

from 1.8 to 2.2 and at a temperature ranging from 869 to 1014°C. Results proved that the method is suitable for MWCNT synthesis, with higher yield for increasing equivalence ratios.

Normal Diffusion Flames

While studying soot formation from a normal diffusion flame (NDF) with different hydrocarbons, Saito et al. [68] were the first to report the formation of elongated carbon fibres using this method. Given their discovery, Saito gave continuation to his previous work and set off to produce CNT using methane-air diffusion flames [69]. Catalytic supports of Ni-Cr wire were used to collect deposited CNT. From the experiments resulted MWCNT with diameters between 20 and 60 nm and a synthesis temperature around 1500K. The relevancy of the supported substrate was also highlighted, as only soot formation occurred when only Ni-Cr wire and no stainless-steel mesh was used, meaning it was somehow important for CNT yield. They also suggested that oxygen plays an important role on the whole process.

The same group then decided to use ethylene-air diffusion flames achieving relevant conclusions. When bare stainless-steel mesh was used as substrate, only soot formation occurred. Even so, when using a pre-oxidized substrate, nanotube growth was noticeable again, highlighting the importance of metal oxides for nanotube synthesis. Also, when introducing the same Ni-Cr wire they had used in methane flames on the ethylene flames amorphous carbon growth was noticeable leading to the assumption that carbon nanotubes formation is dependent on hydrocarbon fuel type. The addition of inert gas (N_2) lowered the synthesis temperature and more uniform nanotubes were obtained [70].

Vander Wal et al. also employed diffusion flames to synthesize SWCNT. For that purpose a flame of hydrocarbon diluted with inert gas conjugated with metallocene catalytic precursors was used. Again the importance of hydrocarbon fuel type was referenced and the use of inert gas up to a limit concentration proved to increase the yield. Upon analysis it was found that SWCNT with an average diameter of 1.4nm were obtained [71].

In 2002, Hu et al. [72] conducted an experiment using C_2H_4 (acetylene) and air co-flow diffusion flames with cobalt as catalyst on a solid support. The substrate was of particular interest in their studies, as the use of silicon substrates with anodic aluminium oxide (AAO) as a template was exploited. This unique substrate combined with depositions of cobalt as catalyst, enabled the production of well aligned MWCNT. More importantly, this type of substrate was praised for the ability to control the characteristics of the nanotubes according to substrate preparation.

In 2009, Li and his co-workers [73] took a similar approach to Hu and investigated the use of Si-AAO and Ni-Alloy substrates placed on a co-flow methane-air diffusion flame. Similarly, when using AAO templates the resultant MWCNT were orderly aligned and with very controllable diameters. On the other hand, for Ni-alloy substrates there is no organization whatsoever in the yield products deposition, which grows on random directions. Furthermore, when analysing the temperature, a value between 1023 and 1073 K was found to be desirable for optimum synthesis.

Camacho et al. [74] completed an extensive study on the influence of hydrocarbon precursor on carbon nanotube synthesis using a co-flow diffusion flame. Methane (CH_4), Propane (C_3H_8) and acetylene (C_2H_2) were subjected to analysis. For methane, MWCNT with diameters between 9 and 15 nm were produced,

however, the yield was reduced compared to the other fuels. Propane yielded MWCNT on a very limited range of fuel rates. The nanotubes produced using propane possess diameters between 30 and 80 nm and had no evidence of fractures or defects. Acetylene provided a wide range of carbon nanotubes with increase in production.

Counter Diffusion Flames

Counter Diffusion flames (CDF) offer the advantage of having a 1D geometry and were first employed with the intent of forming carbon nanotubes by Merchan-Merchan et al. [75] in 2002. An oxygen enriched (excess of 50%) diffusion flame without any catalyst was the chosen setup. The top nozzle of the burner provided the fuel (methane) as the bottom nozzle provided the oxidizer. Inert gas was used and MWCNT were in fact synthesized.

In a later study following upon their initial work, the same group used the same counterflow setup but introduced a Ni-based catalytic support on the fuel side [76]. By studying different flame locations (radially and vertically) with transmission electron microscope it was noticeable that flame location strongly influenced both the presence and the morphology of carbon structures even when the catalyst was maintained, due to the intense radial gradients found in this flame structure.

Despite the inconsistency that characterizes counter diffusion flames regarding the carbon structures produced within the flame region, Li et al. [77] produced outstanding work employing counterflow diffusion flames using methane as fuel and substrates including Silicon-AAO and Ni-alloys. Analysing temperature and carbon source effects, extremely good conditions were achieved to produce high quality VACNT (vertically aligned carbon nanotubes) in relatively short times compared to CVD methods.

Inverse Diffusion Flames

Inverse diffusion flames (IDF) differ from NDF in the way fuel and oxidizer are delivered. In IDF the oxidizer sits in the centre while the fuel is outside.

Nanotube synthesis by means of an inverse diffusion flame is the least common of all the flame types mentioned above. In the literature one of the forerunners of production using IDF was Lee et al. in 2004 [78]. The substrate used was stainless steel coated with nickel nitrate and they came to the conclusion the effective zone for MWCNT production was between 5 and 7 mm from the centre (radial direction) with diameters between 20 and 60 nm. As for the temperatures, only between 900 and 1300K the production of nanotubes was observed. For temperatures below those, nanofibres were dominant.

Two years later, Xu et al. [79] conducted another experiment using methane inverse diffusion flames. In this work substantial effort was made to gain insight on the nanotube growth mechanism in IDF environment. A varied array of catalytic probes were used, including binary and ternary alloys. The importance of catalytic material relative to local gas temperature and availability of carbon source species was explored. Many carbonaceous structures with different morphologies were obtained, however, it was observed that the ternary alloy (60%Ni + 16%Cr + 24%Fe) combined with 12 to 15 mm heights above the burner provided optimal conditions for nanotube growth. The differences obtained in morphology of carbonaceous structures when using varying catalysts at the same height and radial coordinates and

therefore, similar flame conditions, proved that the chemical composition of the catalyst plays a major role in carbon nanotubes synthesis. Other remarks are made regarding species concentration (CO , C_2H_2 and H_2) at the different heights.

Another relevant reference is the effort of Unrau et al. [80]. While employing a co-flow IDF, the authors claimed that controlling the equivalence ratio enabled the establishment of a “visibly” soot free inverse diffusion flame allowing the production of good quality SWCNT.

Hou et al. [81] studied the radial distribution of the concentration of species responsible for synthesizing CNT, mainly CO and C_2H_2 . The conclusion was that low levels of CO and C_2H_2 accounted for no synthesis of CNT. Also, for substrate temperatures under 400°C no production occurred. The ideal temperature reported for growth of CNT went up to 1300K , coincident with Lee et al. [78].

Catalyst and inert gas dilution

As mentioned before, the catalyst is an essential element of carbon nanotubes formation. Transition metals are usually the main choice because of their ability to catalytically break carbon molecules. Nano-sized particles composed of transition metals such as Nickel, Cobalt, Iron, etc. possess the appropriate characteristics suited to carbon nanotubes formation such as, melting temperature, solubility of carbon and carbon diffusion rates in the metal. Combinations of these metals as alloys usually provide better results [82]. Normally, the substrate is coated with a layer of the catalytic material through a diversity of methods such as physical vapour deposition, ultra-sonication, pulsed controlled plating method or electrodeposition. MWCNT formation on stainless steel has also been reported, direct substrate catalytic activity can be achieved by a variety of processes: grinding and polishing, metal etching with strong acids and also from surface breakup [55]. The last process is promoted by surface carbonization which leads to catalytically active nanoparticle formation. The catalytic sites generated are dispersed in a wide range of dimensions. Given that the diameter of the catalyst particle plays a foremost role on the dimensions and morphology of the carbonaceous structure produced, with direct substrate catalyst it is expected to have resultant CNT with a variety of diameters [83].

Inert gas dilution is a mechanism first utilized as a means of controlling flame temperature. Yuan et al. [70] introduced nitrogen in the ethylene-air flame medium. When comparing diluted vs undiluted flames, the temperature was 1244°C and 1547°C , respectively, and there was an increase in yield along with a narrower diameter distribution. In a different experiment, Li et al. investigated the effects of nitrogen presence in a counter diffusion methane flame. With increasing percentage of N_2 added to the flame the larger the mean diameter of the produced nanotubes. The addition of N_2 also synthesized straighter CNT [77].

1.2.8 CNT Growth Under Electric Field Bias

After the discovery of CNT the necessity for improved, more uniform and pure carbon nanotubes was immediate and the application of an electrical field capable of improving yield quantities and aligning the growth directions through electrostatic forces appeared as a possible route.

Nanotube synthesis with influence of an electric force was first introduced using flame synthesis by Merchan-Merchan et al. [84] who applied it when working with a counter diffusion methane flame. Their experimental procedure consisted of comparing nanotube yield with two different approaches which they named as FPM (Floating Potential Mode) and GPM (Grounded Probe Mode). The former refers to synthesis with electric field, established between the probe and the edges of the outlet nozzles, and originated from the transport of ions and electrons characteristic of the oxygen flame to the substrate. The latter refers to production without any electrical bias. Potentials of 300mV were achieved and the results confirmed that the presence of the electrical field was beneficial. Not only the presence of small aligned bundles of carbon nanotubes was detected in scanning electron microscopy images, those were more uniform in diameter. The growth rate and flame area suitable for nanotube production were also improved. A reduction in contamination was also achieved. Furthermore, the alignment mechanism of the carbon nanotubes was explained as follows.

Consider a single carbon nanotube, growing on a metal support, that can be characterized as a conductive cylinder of length L and radius R . Due to the presence of the electric field, polarization occurs and a bound charge is created on the tip of the carbon nanotube. It is known that a charge inserted in an electric field is subjected to an electrostatic force $F_e = qE$. For more details on the exact expression of the electrostatic force acting on a conductive cylinder attached to a plate is found in the work of Taylor [85]. In more simple terms, consider the carbon nanotube having a small deviation θ from the normal direction, the electrostatic force can be decomposed in axial and tangential components as per Figure 1.12.

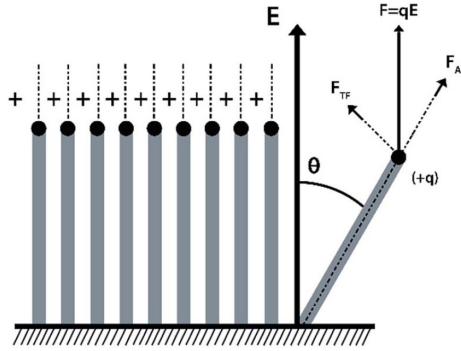


Figure 1.12: Electrostatic force acting on CNT. Adapted from [55].

The tangential force, $F_{TF} = qE \cos \theta$, has the role of orientating the CNT according to the electric field. As for the axial force, $F_{AF} = qE \sin \theta$, it stretches the CNT and dampens the thermal vibrations those are subjected to during the synthesis process. For an array of growing CNT there are subtle alterations on the actual values of the force. Also, repulsion forces resultant from same polarity surface charges must be contemplated. These are responsible for maintaining separation and aiding in the alignment of the CNT overcoming van der Waals attractive forces. Other important aspect mentioned by Merchan-Merchan is the fact that the electric field also polarizes the catalytic particles at the tip of the CNT (for tip growth), maintaining its orientation constant while avoiding helical or spiral nanotubes that derive from changes in

the orientation of the catalytic particles. Later, to continue upon their experiments, Merchan-Merchan et al. [86] proceeded to apply an external voltage supply and assess the effects inflicted on CNT formation. The experiment consisted of varying the voltage from 0.3V up to 3V and using SEM and TEM to analyse the products yielded. At low voltages, in the interval of 0.3V to 1V, a layer of high purity VACNT was observed. The average thickness of the array increased from 9 μm (0.3V) to 21 μm (1V), stagnating at the higher value when increasing the voltage to 3V. Above 3V the morphology of the CNT started to modify with the appearance of helical CNT. At 5V the phenomena visible in the TEM and SEM images was the breaking of the catalytic particles which formed a sprout, creating potential sites for growth of new nanotubes along the trunk of the initial ones. In fact, that was verified for 12V and up to 25V. The CNT yielded when under these voltages achieved what the authors called full Y-branching, T-branching and multi-branching. These results are summarized in Figure 1.13.

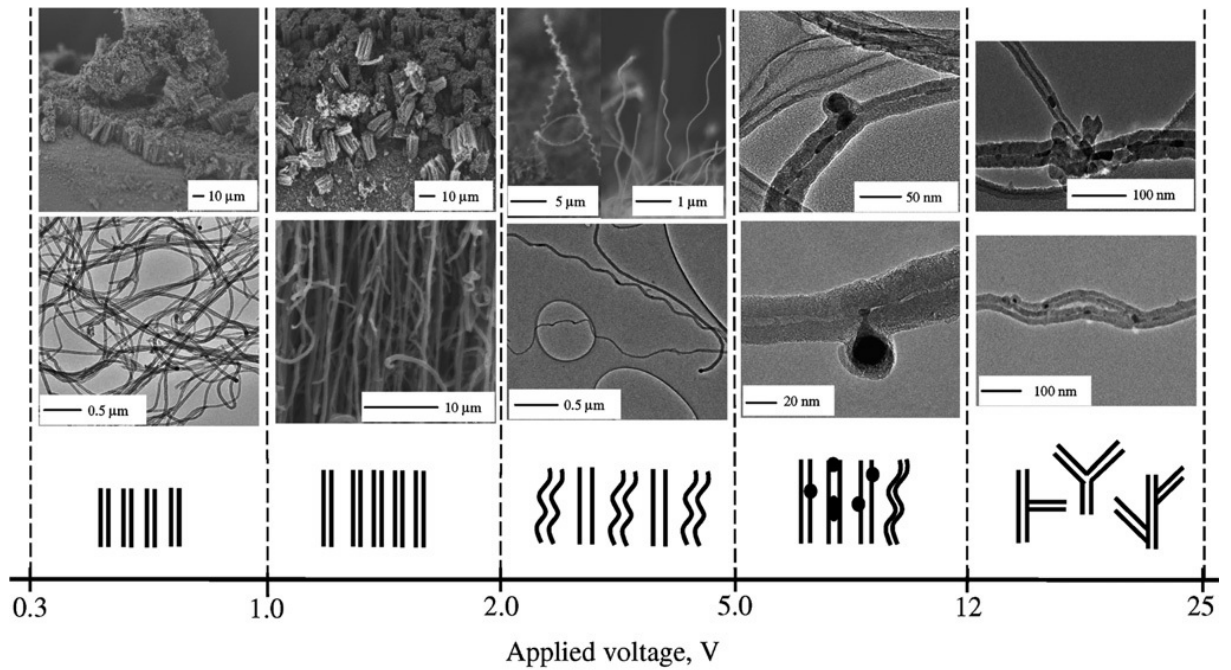


Figure 1.13: Electric field effect on the morphology of synthesized CNT. Adapted from [86].

A similar study was carried out by Xu and his colleagues [87] using a different fuel and flame configuration. An inverse diffusion flame with methane as fuel was selected and a voltage bias was applied on the various substrate probes tested. Both floating potential mode as employed by Merchan-Merchan [84] and external voltage supplies are addressed while the burner assembly is kept grounded at all times. The first step in their analysis is to vary the catalytic probe type and the height above the burner where the probe is placed, analysing the products and aiming to determine the best conditions for formation of CNT. Only afterwards the effects of electric bias were approached. Conclusions achieved are coincident with those of Merchan-Merchan [86] in what regards the beneficial effects concerning growth rates and alignment of the CNT. Moreover, electric field enhances the quality of the CNT by electrophoretically keeping soot particles and other contaminants away from the formation area. Also, a comparison between

positive and negative bias ($\pm 2V$) was carried, showing that negative voltages produced slightly better results, although a justification for that fact is not found. All the experiments mentioned report the same tip-growth mechanism.

In 2006, Bao and Pan [88] delved into the electric field application on premixed flames with some more detail. An external DC power supply provided a voltage of 25V creating an electric field with strength of $\approx 6.5 \cdot 10^2 V/m$. Using a simulation programme, it was claimed that in the central region the electric field was uniform and perpendicular to the substrate. From the experiment, orderly aligned carbon nanotubes arose, with few defects and with a narrow diameter distribution which is coincident with the studies previously mentioned. From the electronic microscopy analysis, the growing method is tip growth, as a layer of catalytic particles was visible on top of the CNT. Moreover, the application of the electric field greatly improves repeatability and controllability of carbon nanotubes growth. In addition, a simulation for the local electrostatic forces acting on the nanotubes and the catalytic particles was carried out based on a finite element method. An important conclusion drawn from the calculations is that the electrostatic force acting on the catalytic particle is considerably greater than that acting on the nanotubes themselves, as shown in Figure 1.14, meaning that a tip growth is essential towards the alignment of the CNT.

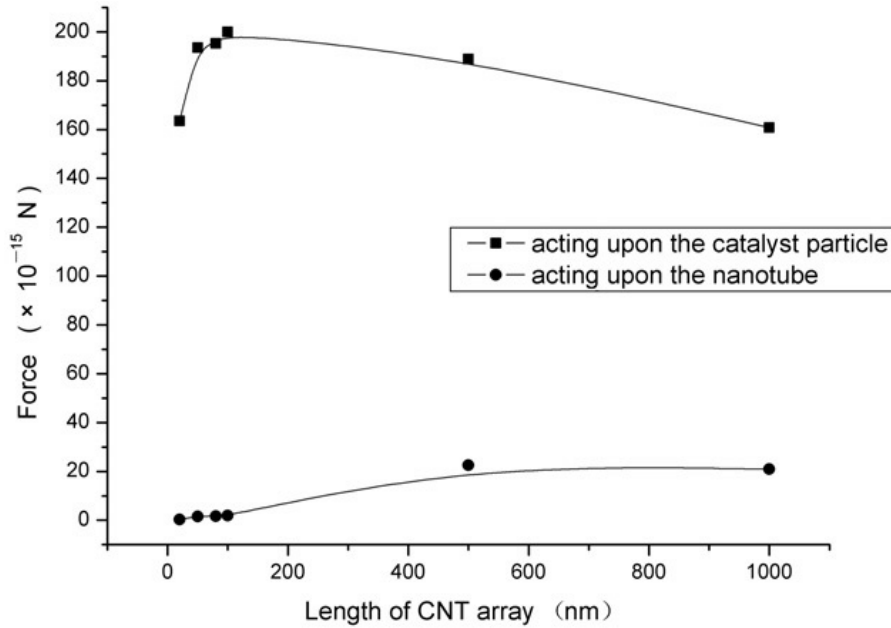


Figure 1.14: Electrostatic forces acting on CNT and catalyst particles. Adapted from [88].

Electric field was applied to a pyrolysis flame by Sun and his co-workers in 2013 [89]. The main chamber was heated by C_2H_2 flames while the pyrolysis flame was established using CO and H_2 . The electric field was implemented between a stainless steel substrate, coated with an alloy catalyst, and the pyrolysis chamber. The voltages applied were higher than the experiments mentioned before, ranging from 30 to 60V. The same results as mentioned before were achieved and, in addition, the authors claim an increase in the durability of the catalyst translated to gains in yield of carbon nanotubes.

1.3 Objectives

To establish flame synthesis as a prominent alternative to carbon nanotubes production it is important to clearly understand the growth mechanisms and the parameters influencing the synthesis process so that optimal conditions can be achieved. Electric fields have been employed to improve the morphology of deposited CNT, however, detailed studies on mass variations derived from moderate electric fields have not been performed. Furthermore, the dynamics of the mass growth rate of CNT produced by flame synthesis with application of E have not been previously described.

In this thesis, a premixed Propane/Air flame was employed along with a moderate electric field to investigate the growth of carbon nanotubes. The objective of this thesis is to understand the effect of moderate electric fields on the synthesis of carbon nanotubes regarding mass produced and morphology, while also investigating the mass growth rates in search for the characteristic laws of this process.

1.4 Thesis Outline

This document is segmented in four chapters, Introduction, Experimental Setup, Results and Discussion and finally, Conclusions. The introductory chapter provides the motivation behind this work, a state of art review on the subject, the objectives to be attained and the outline of the document is described. In chapter 2 all the experimental setup and methods are clearly described. The third chapter, Results and Discussion, presents all the results obtained along with a discussion of the outcomes. Finally, in chapter 4, some concluding remarks regarding all the work elaborated are presented, followed by some suggestions for future works.

Chapter 2

Experimental Setup

2.1 Combustion System

The combustion system utilized throughout this experiment consisted of a Bunsen burner, mass flow meters and all the reactant gases required to establish the premixed flame, a DC power supply and an oscilloscope. To analyse the flame temperature a thermocouple was installed and a digital camera was used to capture images of the flame. The schematic of the installation is provided in Figure 2.1. In addition, a pot with boiling water is placed above the burner to create the impinging flame.

The real experimental setup is visible in Figure 2.2

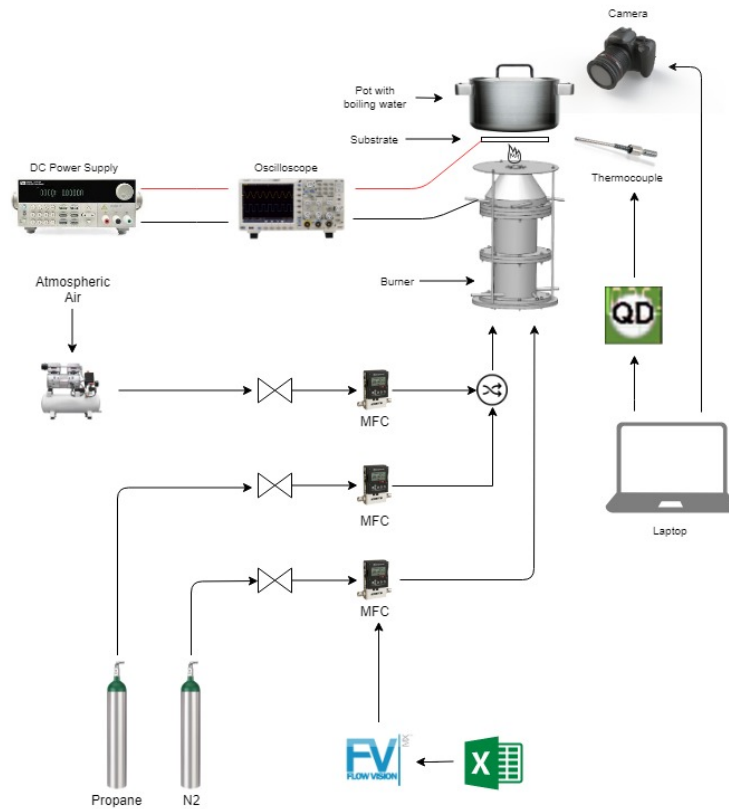


Figure 2.1: Combustion system schematic.

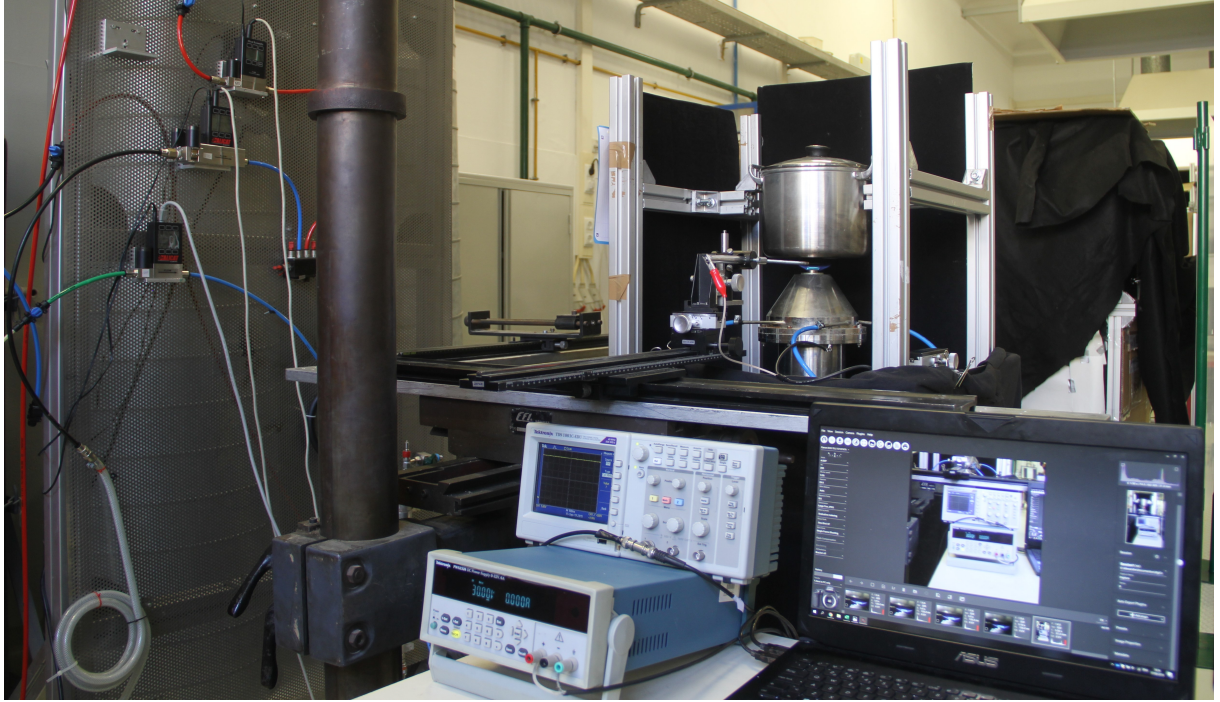


Figure 2.2: Real experimental setup.

2.1.1 Bunsen Burner

The burner used is denominated a Bunsen burner, constructed from 304 stainless steel and composed by three different sections bolted together. The outlet has a diameter of 20 mm and a thickness under 0.2 mm. A 3D model of the burner is depicted in Figure 2.3.

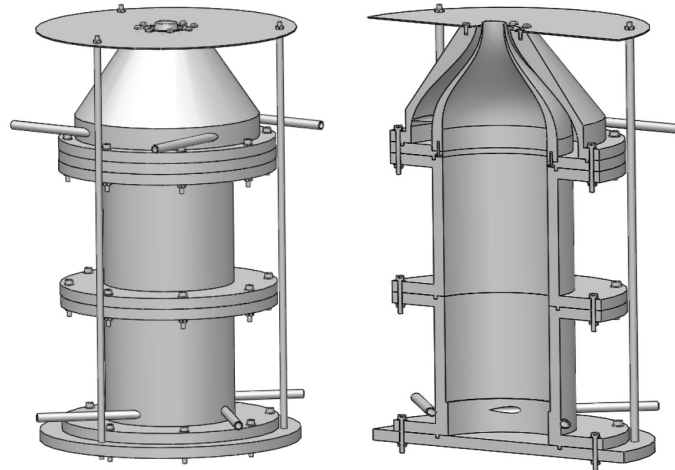


Figure 2.3: CAD model of the Bunsen burner.

The internal wall of the burner was designed so that the roughness is below $0.3 \mu\text{m}$ and the burner is able to sustain a stationary, laminar and plug flow. The lower sections have a diameter of 100 mm. The mixture enters the burner at the bottom through 4 tangential inlets that aid mixing. A co-flow of nitrogen

flows through an independent runner and also enters the burner through 4 other tangential inlets. The contraction on the last section of the burner allows for a top hat velocity profile while boundary layer effects can be neglected. At the outlet the minimum thickness provides negligible heat losses. In Figure 2.4 is shown a technical draw of the outlet nozzle section.

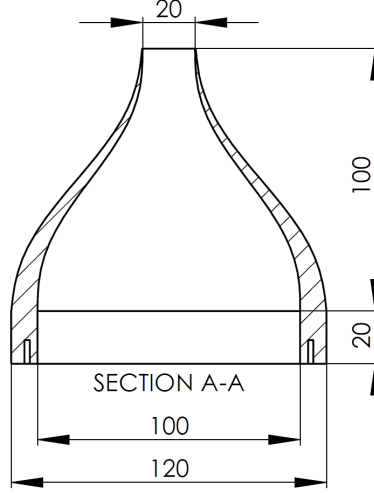


Figure 2.4: Outlet nozzle drawing.

2.1.2 Mass Flow Controllers

To control the flow rates of all the gases, Alicat Scientific flow controllers in conjunction with Flowvision software were used. For each gas one independent controller was available. MC-1SLPM-D (maximum capacity 1 LPM) for propane, MC-500SCCM-D (maximum capacity 0.5 LPM) for nitrogen and finally, MC-50SLPM-D (maximum capacity 50 LPM) for air. The values presented by these equipments had an uncertainty associated with readings ($\pm 0.8\%$) and scale ($\pm 0.2\%$).

The input values in LPM were calculated as a function of two parameters, equivalence ratio (ϕ) and Reynolds number (Re) relative to STP conditions. Based on these two values, the mass flow values were obtained. Reynolds number is defined by Equation 2.1:

$$Re = \frac{\rho_{mix} D_{burner} V_{mix}}{\mu_{mix}} \quad (2.1)$$

where ρ_{mix} stands for the volumetric mass density of the fuel-air mixture, D_{burner} is the outlet diameter, V_{mix} and μ_{mix} the mixture velocity at the exit and dynamic viscosity, respectively.

The equivalence ratio is calculated according to the stoichiometry of the combustion reaction, following Equation 2.2:

$$\phi = \frac{\dot{m}_{C_3H_8} / \dot{m}_{air}}{(\dot{m}_{C_3H_8} / \dot{m}_{air})_{st}} \quad (2.2)$$

where $\dot{m}_{C_3H_8}$ and \dot{m}_{air} refer to the mass flow rates of propane and air, respectively, while st means the values relate to stoichiometric conditions.

2.1.3 Combustion Gases

Throughout all the experiments the premixed flame was established by burning C_3H_8 and air, with a surrounding co-flow of N_2 . Both the propane and nitrogen were supplied in research grade bottles by Air Liquid (AlphagazTM N35) with a purity of at least 99.95% (V/V). Air is atmospheric and stored in an air compressor, then fed through specific lines to the flow controllers. All of the connections were threaded with Teflon and valves were implemented for security.

2.2 Sampling System

The stainless steel substrates were positioned in the flame by means of a three-way translator. This configuration allowed movement in the x,y and z directions, ensuring a correct and easy placement while handling the samples. This mechanism uses precision screws with gears for a precise control. A metal rod with a narrow slot at the end was used to secure the stainless steel plate and a similar mechanism is applied for positioning of the thermocouple.

2.2.1 Coordinate system

A coordinate system is crucial to properly define not only the position of the substrate, but also the positions where the temperature is measured. The Figure 2.5 depicts the coordinate system adopted for our experiments. The origin of our referential is coincident with the centre of the outlet nozzle and the height of the substrate is defined as height above burner (HAB). For $z=0$ corresponds $HAB=0$. The points A to F are the points of interest in this report, where temperatures were measured, and visible in Figure 2.5.

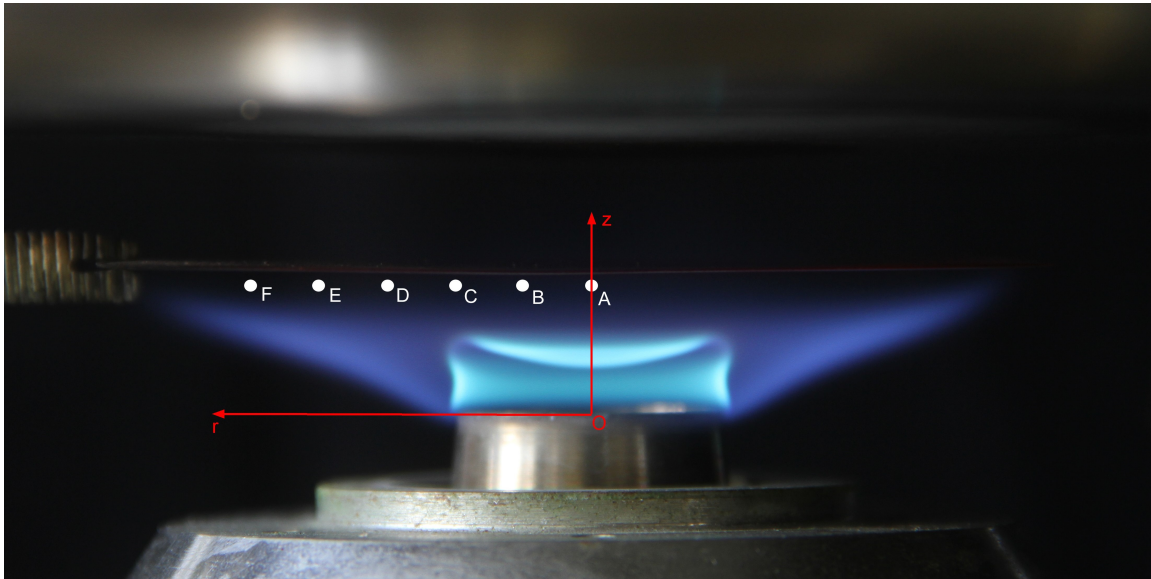


Figure 2.5: Flame coordinates (r , z) in millimetres. The coordinates for each point (r,z) are: A(0,10), B(5,10), C(10,10), D(15,10), E(20,10), F(25,10)

2.3 Acquisition System

2.3.1 Thermocouple

Thermal measurements were performed through a home-made, 65 μm Pt/Pt-13%Rh type R thermocouple. This device is rated for temperatures up to 1700°C, more than suitable for our experiments as no values above or near this limit were registered. The thermocouple was connected to a Data Translation DT9828 acquisition board that communicates with the computer via specific software, QuickDAQ 2013. Figure 2.6 displays the exact thermocouple used.



Figure 2.6: Type R thermocouple used for measurements.

2.3.2 Analytical Balance

The amount of deposited CNT was evaluated through mass measurements of the substrate prior to insertion over the flame and after completion of the experiment. An analytical balance was used, KERN ABS 80-4N, which operates under ISO 9001 certification.

2.3.3 Camera and Lens

To register photographs of all the experimental setup, the flame and substrate depositions a DSLR camera was used. The Canon EOS-7D along with an EF-S 18-135mm f/3.5-5.6 17 IS USM lens was the equipment provided for image acquisition.

2.3.4 Particle Implementation Velocimetry

In order to study the flow and better understand the influence of the electrostatic force on the molecules involved, the particle implementation velocimetry (PIV) is a very useful, precise and non-intrusive tool that measures velocity fields through image analysis of seeded flows. The system takes measurements by aiming a double pulsed laser at the seeding particles injected in the flow, thereby illuminating them. The laser can be described as a planar sheet of green light, with an approximate wave length of 530nm, aimed at the area of study, which in this case is our flame.

The double-pulsed laser, as the name states, illuminates the particles in two consecutive instants registered by a high-speed sCMOS camera synced with the laser. Therefore, two frames consisting of multiple images are obtained that allow the extrapolation of the mean velocity field. The time span

between frames is defined and the distance travelled is calculated from the difference between frames, meaning that a velocity field can be attained.

The density of particles introduced in the flow must be in tune with the density of the flow to be analysed. A correct seeding ensures gravitational errors are avoided [90]. Even with appropriate seeding, the particles themselves are of utmost importance, these should have good light-scattering properties, be non-volatile, non-abrasive and non-corrosive. For the purpose of our analysis, alumina seeding particles with diameter of 3 μm were selected. This material and diameter are adequate for high temperature gaseous flows [91]. The particles were placed in a small reservoir while being constantly agitated with the use of a mixer, so that adequate dispersion was achieved.

When the seeded flow is stable, the double pulsed laser is activated and starts illuminating the particles. The light sheet created by the laser is approximately 1mm thick at the focal point, focal point which is calibrated to the field of view of the camera.

The laser was a Dantec Dual Power 65-15 Yag, which has two cavities with 15 Hz of maximum laser pulse frequency each. The camera was perpendicular to the laser sheet for proper recording of images and the model used was a HiSense Zyla sCMOS, capable of resolutions of 2560x2160 pixels and a speed of 40 fps. To avoid excessive light and ensure only green radiation hits our target, a 532nm Melles Griot filter was placed appropriately. To accomplish synchronization between the laser and camera, a BNC 575 Series Pulse Generator combined with Dantec Dynamic Studio was utilized. The software also allowed the post-processing of the data obtained.

For correct dimensional analysis a scaling process has to be performed so that pixels can be related to millimetres. This is done by taking a frame with a millimetre graph paper that allows the creation of a relation. Another important aspect to take into consideration is the number of paired frames. If this number is too low there is insufficient and inconsistent information to obtain respectable results. On the other hand, if the number of paired images is excessive, computational time and memory uptake becomes unjustified. This parameter was set at 200 pairs of images captured.

The 2D velocity fields are obtained by an average correlation method. This means that, for each interrogation area (IA), a correlation function is averaged at each location for every image. Each image is subdivided into small rectangular areas of n by n pixels that are denominated as interrogation areas. For each of these interrogation areas, the pictures captured in the consecutive frames are correlated by averaging the particle displacement between frames. This process is done for all the pairs of images captured in each frame for each interrogation area, ultimately resulting in an average velocity field for each IA. As in every experiment, errors can appear and interfere with the results. These errors can be mitigated by eliminating the background of the image which reduces overall brightness or by applying a Range Validation to eliminate inconsistent velocity vectors. The IA used for our experiment was sized 32 by 32 pixels.

Another user input that must be defined is the time between pulses. An accurate selection is crucial to obtain trustworthy results. If the interval is set too low, the particles may not have enough time to move and very small vectors are extrapolated. On the other hand, if the time frame is set too high the particles may travel distances long enough that by the time the second frame is captured the particle is outside

the interrogation area. If this is the case, the measurements achieved are erroneous. It is important to note that in each IA, for the first frame, there will be particles close to the edge that unavoidably will dislocate to another IA. This aspect can be bypassed by setting an overlapping factor. In this experiment, an interval of $200\ \mu\text{s}$ and an overlapping factor of $50\% \times 50\%$ were selected.

The working conditions for PIV measurements were Reynolds number of 300 and the stainless steel substrate placed at $\text{HAB}=10\text{mm}$. In Figure 2.7 is displayed the schematic of the PIV installation.

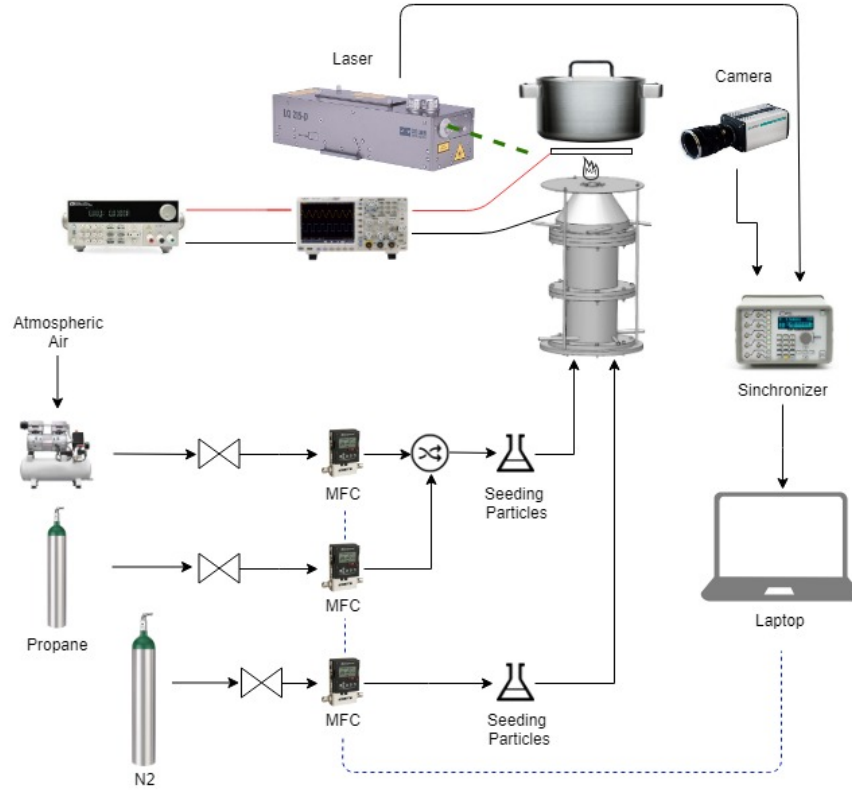


Figure 2.7: PIV experimental setup.

2.4 Electric System

For the purpose of this work an electric field had to be established between the substrate and the burner assembly. This meant that connections had to be set up and proper equipment had to be installed.

2.4.1 Power Supply

The voltage was supplied by a direct current power supply, branded Tektronix PWS2326. This equipment has voltage capabilities ranging from 0 to 32V and is in conformity with the Directive 2004/108/EC for Electromagnetic Compatibility. The power supply was connected using copper wires to an oscilloscope so that the voltage supplied could be constantly monitored. The oscilloscope model was Tektronix 1001C-EDU and also meets the intents of the normative mentioned for the power supply. From the oscilloscope, the substrate and the burner were connected according to specified experimental conditions, both the

substrate and burner could be charged or grounded for testing purposes. In Figure 2.8 are displayed the power supply, oscilloscope and all the connections. During this report, a positive voltage refers to the substrate being charged and the burner grounded while negative voltages refer to the opposite scenario.

For verification, a multimeter was also available to measure the voltage between the burner and substrate, thus confirming the connections were correct and the electric field was indeed being applied. The model used was a RANGE RE68.

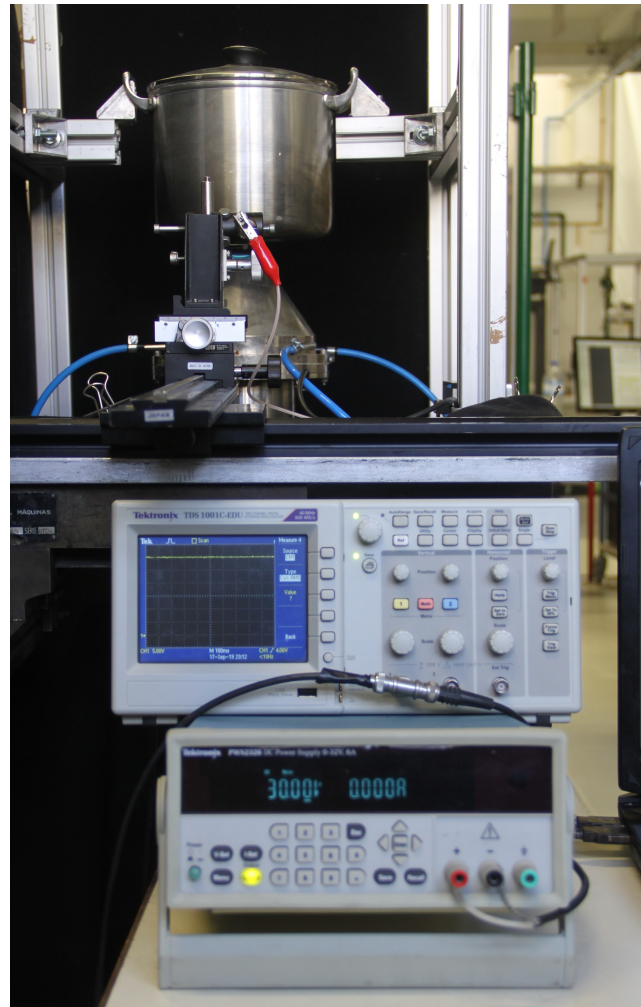


Figure 2.8: DC Power supply and oscilloscope.

2.5 Carbon Nanotubes Production

2.5.1 Premixed Flame

As mentioned before, a premixed flame of Propane (C_3H_8) and Air with co-flow of Nitrogen (N_2) was selected for CNT production. To establish the flame the following procedure was followed. Firstly, all the mass flow controllers are connected to the laptop, the software Flowvision is turned on, and the connection between laptop and flow meters is configured. Subsequently, all the security valves for C_3H_8 and air are opened. Then, the N_2 bottle is opened, with the pressure set to 2 bar. With all the valves opened, the values for all the mass flows are input to Flowvision, a few seconds are allowed so that the gas flow reaches the outlet and then the flame is ignited. From here, both the power supply and oscilloscope are turned on, followed by the introduction of the voltage selected for the trial. When the water in the pot is boiling, the substrate is placed in the three-way translator. The voltage between the substrate and the burner is checked with the multimeter, and if everything is in conformity to trial conditions the substrate is placed in the desired HAB and radial position over the flame. After the specified experimental time the substrate is removed from the flame and set aside for cooling. If there are no more trials to be conducted the flame is extinguished and all valves and handles are closed. The electrical equipments and flow meters are turned off for completion of the process.

2.5.2 Sample Preparation

Throughout the entirety of this work two types of substrates were used, stainless steel and coated stainless steel, both in the form of plates with dimensions of 50x40x1 mm. The former was annealed stainless steel (SS) that was sanded with 120 grit sandpaper (Dexter brand) and cleaned with acetone before every experiment. All these plates were used multiple times. The latter consisted of stainless steel coated with zinc and cobalt derived materials that were electrodeposited on stainless steel substrates. The details of the electrodeposition process are provided below.

2.5.3 Electrodeposition of Zinc and Cobalt

Surface manipulation processes are widely used in engineering for different purposes. Whether for protection or insulation, there are a variety of surface manipulation processes available. From Section 1.2 it was clear that metal catalyst particles are favourable towards production of CNT, so in that sense a thin layer of zinc and cobalt derived materials were deposited on the surface of our substrate.

Electrodeposition is a simple and versatile surface manipulation technique that allows the deposition of a metal or alloy coating on a conductive surface via electrolysis. No expensive equipment is required and it is feasible at low temperatures. This procedure involves an anode, a cathode, an electrolytic bath and a power supply. The chemical mechanism behind the technique is the reduction-oxidation reaction that occurs at both electrodes. This means that positive ions from the metal salt solution are transported to the cathode surface under the influence of the electric field. Electrons are released from the substrate surface being coated, thereby reducing metal ions to metal form [92].

The deposition characteristics depend on the metals used both in the salt and as substrate, however, the parameters available for user control are current density and deposition time. By using this process it is possible to obtain a quality coating of the cathode in under a few minutes.

The setup used for this work is displayed in Figure 2.9. The parameters used for both depositions were a current of 1 ampere and a working time of 2 minutes. The Power Supply also displayed a voltage of 3.4V.

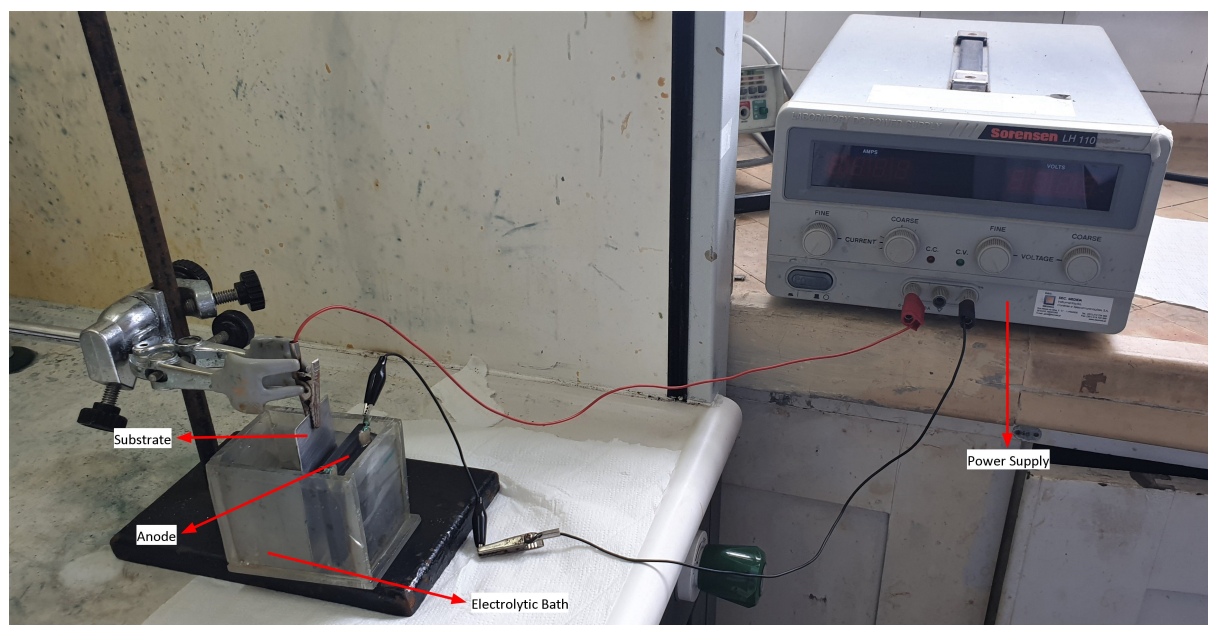


Figure 2.9: Real setup for the electrodeposition of the zinc and cobalt materials on the substrate.

Zinc and Cobalt Solutions

For both depositions, stainless steel plates were used. Prior to the procedure, both samples were polished with 120-grid sandpaper (Dexter), cleaned with acetone and dried carefully with lint free paper towels. This followed the same exact procedure carried out for every experiment.

All the experiments were carried out at room temperature, by connecting both the substrate (cathode) and the graphitic electrode (anode) to a Kikusui Electronics PAB32-3 power supply.

The solutions of zinc and cobalt were prepared using analytical grade chemicals and distilled water. For both electrolytic solutions 1L of solution was prepared. For zinc, 0.5M of ZnCl_2 (zinc chloride) and 2M of NH_4Cl (ammonium chloride) were present in the solution. For the cobalt solution, this was prepared with CoCl_2 (cobalt chloride), NH_4Cl and NaCl (sodium chloride). Figure 2.10 shows the stainless steel plate after the cobalt electrodeposition.

After electrodeposition, all residual materials were stored for proper disposal and all the containers used were washed and rinsed with distilled water.

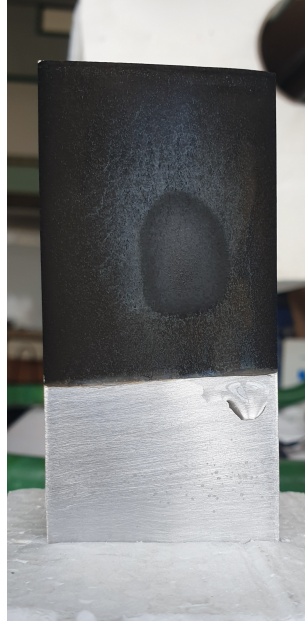


Figure 2.10: Real image of the stainless steel plate after cobalt electrodeposition.

2.5.4 Working Conditions

With the experimental apparatus correctly setup, initial tests were performed to evaluate how carbon nanotube formation occurred. HAB was varied from 4 mm to 16 mm and equivalence ratios of 1.6 and 1.8 were tested. Inert dilution of nitrogen was set at 0.1 LPM. From visual and mass measurements the same conditions regarding HAB (10 mm) and ϕ (1.6) as previous work from Duarte [93] were adopted.

The study mentioned above [93] employed the same burner used for this work and from their results it was established that a specific flame configuration was favourable toward CNT production. For lower Reynolds numbers, the flame assumes a specific shape that is described by Fernandes and Leandro [94] as an envelope flame, visible in Figure 2.11. This particular shape has a central region where reaction is occurring, ultimately resulting in a wider deposition area, therefore this condition was adopted for all the experiments in this work. On the opposite hand, for higher values of Reynolds, a cool central core (tulip) flame is established, with no reaction in the central area, hence the cool core.



Figure 2.11: Envelope flame shape adopted for this work.

As in all flows, there is a convective force associated with the mass and movement of particles. This force may influence the growth direction of carbon nanotubes and compete with the alignment force exerted by the electric field, consequently the variation of Reynolds and Voltage applied had to be studied. The first step was to assess the conditions where it was possible to establish an envelope flame. Starting at $Re=150$ and up to $Re=430$ it was possible to have an envelope flame. However, for Reynolds lower than 250, the flashback risk was high as the flame front was located inside the burner outlet. For Reynolds higher than 400, the flame was not stable.

From Section 1.2 one can conclude that moderate electric fields are sufficient to affect the yield and orientation of carbon nanotubes synthesized in a flame environment. For this study, the voltage applied ranged between 1 and 30V (sign according to Section 2.4.1).

Given all the information above, three values of Reynolds, 250, 300 and 400, were selected to be tested at voltages ranging from -30V to 30V. All trials had a duration of 15 minutes and mass evaluations were performed to register the influence of voltage at each Reynolds number. In Table 2.1 are listed all the tests performed and the respective conditions. Measurements at 0V were registered to set an appropriate basis for comparison.

Table 2.1: Experimental conditions to evaluate voltage effect at different Reynolds numbers.

ϕ	HAB [mm]	t [min]	Re	Voltage [V]
1.6	10	15	250	1
1.6	10	15	250	10
1.6	10	15	250	20
1.6	10	15	250	30
1.6	10	15	250	-1
1.6	10	15	250	-10
1.6	10	15	250	-20
1.6	10	15	250	-30
1.6	10	15	300	1
1.6	10	15	300	10
1.6	10	15	300	20
1.6	10	15	300	30
1.6	10	15	300	-1
1.6	10	15	300	-10
1.6	10	15	300	-20
1.6	10	15	300	-30
1.6	10	15	400	1
1.6	10	15	400	10
1.6	10	15	400	20
1.6	10	15	400	30
1.6	10	15	400	-1
1.6	10	15	400	-10
1.6	10	15	400	-20
1.6	10	15	400	-30

In Chapter 3 it will be shown that for negative voltages, meaning that the positive lead is connected to the burner structure, for both 250 and 400 Reynolds values there is no clear tendency between mass produced and voltage. Also, only for positive voltages of 20V and 30V there seems to be an effect on mass production. However, for Re=300 it is presented that the variation is independent of polarity.

Due to the facts above, and also to compare with the results of Duarte [93] where no electric field was present, Re=300 was the condition chosen to perform a time analysis in order to examine how the implementation of an electric field affected the mass growth rate of CNT. Voltages of 20V and 30V were applied. The tests performed are listed in Table 2.2.

Table 2.2: Experimental conditions to evaluate mass yield versus time with electric field bias of 20 and 30 volts.

ϕ	HAB [mm]	Re	Voltage [V]	t [min]
1.6	10	300	20	5
1.6	10	300	20	10
1.6	10	300	20	15
1.6	10	300	20	20
1.6	10	300	20	30
1.6	10	300	20	40
1.6	10	300	20	50
1.6	10	300	20	60
1.6	10	300	20	70
1.6	10	300	20	90
1.6	10	300	30	5
1.6	10	300	30	10
1.6	10	300	30	15
1.6	10	300	30	20
1.6	10	300	30	30
1.6	10	300	30	40
1.6	10	300	30	50
1.6	10	300	30	60
1.6	10	300	30	70
1.6	10	300	30	90

Regarding the catalyst deposited substrates, these were tested for 10 minutes under a 30V bias. For economical and time reasons, only one test was performed with coated substrates. Without coatings, reusing the steel plates allows repeatable and affordable production. For PIV measurements, these were performed for Re=300 and for all the voltages tested. For comparison purposes, measurements at 0V were also registered.

2.6 Characterization of CNT

It is of utmost importance that the products obtained are fully characterized. To do so, scanning electron microscopy and X-ray diffraction were used to obtain images and structural informations that allow the description of the products as carbon nanotubes. Both the stainless steel substrate and deposited CNT

were subjected to XRD analysis. Removal of carbon nanotubes from the plates was achieved by inserting the deposited substrates in recipients filled with distilled water that were inserted in an ultrasonic bath. The collected CNT were kept inside the distilled water for a few days so that they deposited on the bottom of the recipients. These samples were then placed in an oven at 100°C for 6 hours to evaporate the water. 5 mg of CNT powder were subjected to XRD. Respective diffractograms were captured by a Bruker AXS-D8 advanced powder diffractometer possessing a Bragg-Brentano geometry [Cu K α radiation source ($\lambda = 0.150619$ nm)] with the diffraction patterns registered over a 2θ range from 10° to 70° and at room temperature. The crystalline structure of the stainless steel plates and deposited materials was investigated through scanning electron microscopy (Hitachi S2400 or FEG-SEM, JEOLJSM7001F) while the elemental chemical compositions were obtained by the respective energy dispersive spectrometer (EDS).

2.7 Uncertainties

When performing scientific experiments, uncertainties are always concerning, so they need to be measured and their impact must be accounted for. In the following sections the uncertainties of the flow meters, ϕ , Re , balance mass values, thermocouple, sample positioning measurements and electric equipment are discussed.

2.7.1 Flow Meters

As mentioned in Section 2.1.2 digital flow meters were used to control the flow rate of all the gases involved in the experiments. These possess uncertainties associated with readings and scale of 0.8% and 0.2%, respectively. This means that the overall uncertainty of the flow rates (U_Q) can be calculated by Equation 2.3, where Q_m represents the measured flow rate and Q_{max} stands for the maximum flow rate available for flow meter i.

$$U_Q = 0.008Q_m + 0.002Q_{max}^i \quad (2.3)$$

In addition, an associated relative error (e_Q) can be computed to evaluate its impact on the measurements performed, expected to be higher for the lowest flow rates. Tables 2.3, 2.4 and 2.5 present the results for uncertainties and relative errors for the different values of Reynolds examined.

Table 2.3: Uncertainties and relative error for measurements made while using $Re = 250$.

Gas	Q_{max} [LPM]	Q_m [LPM]	U_Q	e_Q [%]
C ₃ H ₈	5.0	0.224	± 0.0118	5.26
Air	50.0	3.327	± 0.1266	3.81
N ₂	0.5	0.100	± 0.0018	1.80
C ₃ H ₈ + Air	55	3.551	± 0.1384	3.90

Table 2.4: Uncertainties and relative error for measurements made while using $Re = 300$.

Gas	Q_{max} [LPM]	Q_m [LPM]	U_Q	e_Q [%]
C ₃ H ₈	5.0	0.268	± 0.0121	4.53
Air	50.0	3.992	± 0.1319	3.31
N ₂	0.5	0.100	± 0.0018	1.80
C ₃ H ₈ + Air	55	4.260	± 0.1441	3.38

Table 2.5: Uncertainties and relative error for measurements made while using $Re = 400$.

Gas	Q_{max} [LPM]	Q_m [LPM]	U_Q	e_Q [%]
C ₃ H ₈	5.0	0.268	± 0.0129	3.59
Air	50.0	3.992	± 0.1426	2.68
N ₂	0.5	0.100	± 0.0018	1.80
C ₃ H ₈ + Air	55	4.260	± 0.1554	2.74

From the results obtained it is clear that relative errors are low as the maximum error verified is of 5.26% and the measurements can be considered trustworthy. These values could be reduced with a better selection of flow meters. For instance, for air a flow meter with a very high output capacity was used when compared to the flow rates employed. This flow meter was selected on purpose, seeing that high flow rates were necessary to properly extinguish the flame in safe conditions, avoiding any risk of flashback.

2.7.2 Equivalence Ratio

If we rewrite Equation 2.2 in order of the gas volumetric flow rates the impact of the flow rate uncertainties can be accounted for when calculating the equivalence ratio. The result is Equation 2.4:

$$\phi = \frac{a_{st} Q_{C_3H_8}}{x_{O_2}^{air} Q_{air}} \quad (2.4)$$

where a_{st} represents the coefficient of oxygen (O₂) in stoichiometric conditions, $x_{O_2}^{air}$ stands for the average molar fraction of O₂ found in the atmosphere at sea level, Q_{air} and $Q_{C_3H_8}$ are the volumetric flows of air and C₃H₈, respectively.

For the stoichiometric reaction where complete combustion of propane occurs, $a=5$ and $x_{O_2}^{air}=0.2095$ are used [95]. If the uncertainty associated with the density of the fluid is neglected, the uncertainty of the equivalence ratio is obtained by Equation 2.5:

$$U_\phi = \pm \frac{5}{0.2095 Q_{air}} \sqrt{U_{Q_{C_3H_8}}^2 + \left(\frac{Q_{C_3H_8} U_{Q_{air}}}{Q_{air}} \right)^2} \quad (2.5)$$

where $U_{Q_{C_3H_8}}$ and $U_{Q_{air}}$ represent the uncertainty linked to the volumetric flow rate of C₃H₈ and air, respectively. As done for the flow rates, a relative error can be computed (e_ϕ). The resulting errors of the equivalence ratio for the three Reynolds numbers experimented are available in Table 2.6.

Table 2.6: ϕ uncertainties and relative errors associated.

Re	$U_{Q_{C_3H_8}}$	$U_{Q_{air}}$	ϕ	U_ϕ	e_ϕ [%]
250	0.0118	0.1266	1.6	± 0.162	10.13
300	0.0121	0.1319	1.6	± 0.088	5.50
400	0.0129	0.1426	1.6	± 0.072	4.50

2.7.3 Reynolds Number

The Reynolds number was defined in Section 2.1.2 by Equation 2.1. The equation can be rewritten as a function of the total volumetric flow rate, $Q_{total} = Q_{C_3H_8} + Q_{air}$, as per Equation 2.6:

$$Re = \frac{\rho_{mix} D_{burner} Q_{total}}{A_{burner} \mu_{mix}} = \frac{4\rho_{mix}}{\pi D_{burner} \mu_{mix}} Q_{total} \quad (2.6)$$

where, A_{burner} and D_{burner} stand for the area and diameter of the burner outlet, respectively, ρ_{mix} is the mass density of the mixture and finally, μ_{mix} states the dynamic viscosity of the mixture.

From Equation 2.6 it is clear that a proportionality relation between Re and Q_{total} is present, with $4\rho/\pi D\mu$ acting as the constant of proportionality. The same relationship transduces to the relationship between the uncertainties regarding the Reynolds number, U_{Re} , and $U_{Q_{total}}$. Consequently, one can write Equation 2.7 to calculate U_{Re} :

$$U_{Re} = \frac{4\rho_{mix}}{\pi D_{burner} \mu_{mix}} U_{Q_{total}} \quad (2.7)$$

Below follows Table 2.7 listing the Re uncertainties and relative errors for the flow conditions applied throughout this experiments.

Table 2.7: Re uncertainties and errors associated.

Re	$U_{Q_{total}}$	U_{Re}	e_{Re} [%]
250	0.107	± 5.841	1.51
300	0.084	± 5.918	1.97
400	0.130	± 9.158	1.31

The relative associated errors obtained here are extremely low, meaning that these values are precise and of extreme confidence.

2.7.4 Thermocouple Measurements

According to [96], for a thermocouple with length to diameter ratio greater than 200, convection and radiation processes play a huge role on heat transfer, even more so than conduction. Radiation interferes and alters the temperature measurements, and it is stated that variations of $\pm 100K$ are expectable [97]. Since Kelvin and Celsius are related, a variation of $1K$ is the same as $1^\circ C$ so for this work the uncertainty associated with temperature is set as $\pm 100^\circ C$.

2.7.5 Mass Measurements

To evaluate the masses of deposited carbon nanotubes, a Kern analytical balance was used as stated in Section 2.3.2. The balance possesses a readability of 0.1 mg and, according to the equipment manufacturer, the uncertainty of the measurements is about three times the minimum scale interval, meaning $U_{mass} = \pm 0.3 \text{ mg}$ [98].

2.7.6 Height and Distance

The systems employed to dislocate the substrate and thermocouple are characterized by a spatial precision of $\pm 0.1 \text{ mm}$. All other measurements were made through means of a packlist with an associated uncertainty of $\pm 0.5 \text{ mm}$.

2.7.7 Electric Field Equipment

As referred above in Section 2.4.1 a DC power supply was applied to affect the growth process of carbon nanotubes. The power supply had a digital voltmeter integrated and the output values have a setting accuracy that, according to the supplier, can be calculated by Equation 2.8:

$$U_V = \pm(0.05V + 10mV) \quad (2.8)$$

where U_V represents the uncertainty associated with voltage output (V). In Table 2.8 are presented the uncertainties for the different working conditions.

Table 2.8: Voltage uncertainties and errors associated.

ΔV [V]	U_V	e_V [%]
1	± 0.06	6.00
10	± 0.51	5.10
20	± 1.01	5.05
30	± 1.51	5.03

Electric Field Magnitude

Assuming that the electric field generated is uniform the intensity of the field (E) is calculated by the quotient between the applied voltage and the distance between the electrodes ($E = \Delta V/h$). Our burner is not perfectly flat but for simplification, the distance between plate and burner is assumed constant and equal to 12 mm.

Both variables have uncertainties associated hence, to compute the uncertainty of the electric field strength, the fractional uncertainties of ΔV and h are summed, resulting in Equation 2.9:

$$U_E = \pm E \left(\frac{U_{\Delta V}}{\Delta V} + \frac{U_h}{h} \right) \quad (2.9)$$

In Table 2.9 the electric field uncertainties and associated relative errors for the working conditions applied are available.

Table 2.9: Voltage uncertainties and errors associated.

ΔV [V]	h [mm]	E [V/m]	U_E	e_E [%]
1	12	83.33	± 5.69	6.83
10	12	833.33	± 4.94	5.93
20	12	166.67	± 9.81	5.88
30	12	2500.00	± 14.67	5.87

Chapter 3

Results and Discussion

3.1 Substrate Analysis

From the state of art review, it was clear that substrate and catalysts play a critical part on the properties of the synthesized carbon nanotubes. Therefore, a detailed analysis of the substrate utilized was performed. It was of our knowledge from the beginning of the experiments that the sample was made of stainless steel. To complete the description, firstly an X-ray diffraction examination was carried followed by an energy-dispersive X-ray spectroscopy (EDS). In Figure 3.1 is presented the result of the XRD which allows the assessment of the different structures and phases present in the sample. This test yields a graph that plots the intensity of the diffracted X-rays as a function of the scattering angle (2θ).

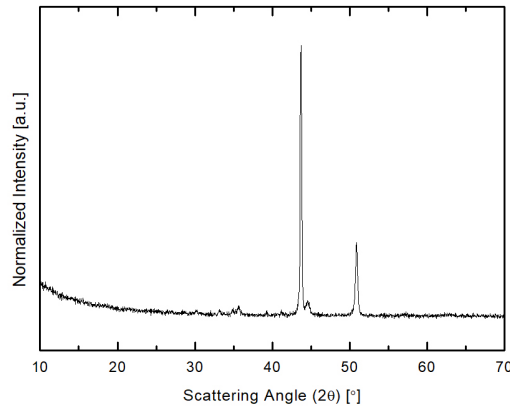


Figure 3.1: Result of the X-ray diffraction of the stainless steel substrate.

Analysing the data from the XRD, two peaks can be clearly identified. At 43.69° and 50.87° . By comparing our data with results found in [99], we can conclude that mostly Austenite (γ -Fe) is found in the structure of our substrate. The peak located at 43.69° identifies the presence of γ -Fe (111), meaning it is arranged in a face centred cubic lattice, while the peak observed at 50.87° denotes the presence of γ -Fe (200).

With the different phases of our steel substrate distinguished, an EDS was performed in order to

evaluate the composition of the steel in terms of the different elements. As reported by the EDS, our steel had a weight composition of 17.5% Chromium, 7.8% Nickel and 1.8% Manganese. From these values one can conclude that the substrate is an austenitic 303L stainless steel. A SEM image for the substrate is available in Figure 3.2.

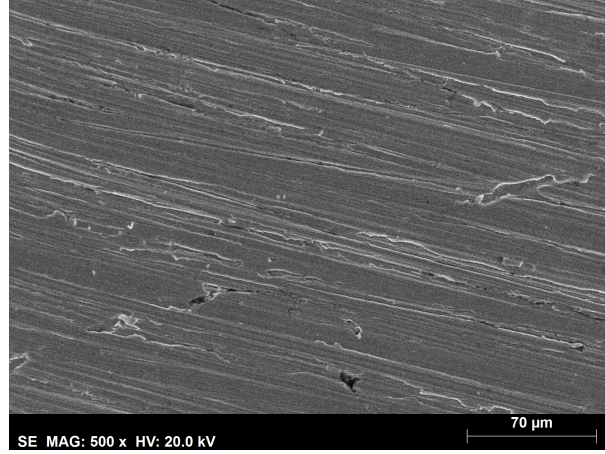


Figure 3.2: SEM image of the stainless steel substrate.

3.2 CNT Synthesized Without Electric Field

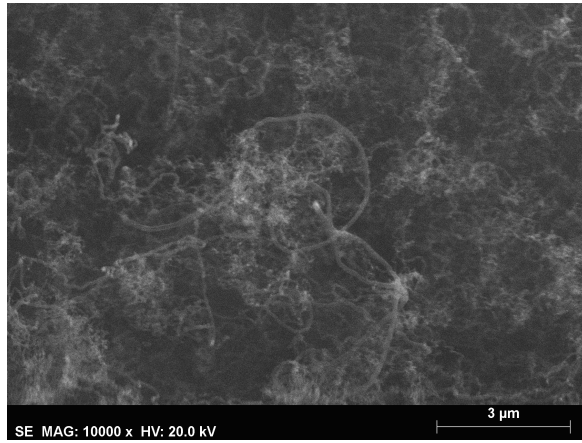
As mentioned in Section 2.5.4, Reynolds number of 300 was known to previously yield carbon nanotubes. Therefore, this was the initial working condition upon which this work based to understand the production and morphology of carbon nanotubes synthesized without application of an electric field. For the working conditions selected, HAB=10mm and $\phi=1.6$, mass measurements and SEM characterization of the yielded CNT was made.

Regarding the mass, 5 consecutive trials with sampling time of 15 minutes at $Re=300$ were performed in order to evaluate the mass production and also the repeatability of the experiment using the flame environment. The results are listed in Table 3.1. The average mass production for 15 minutes was 5.2 mg of carbon nanotubes with a maximum deviation of 0.5 mg.

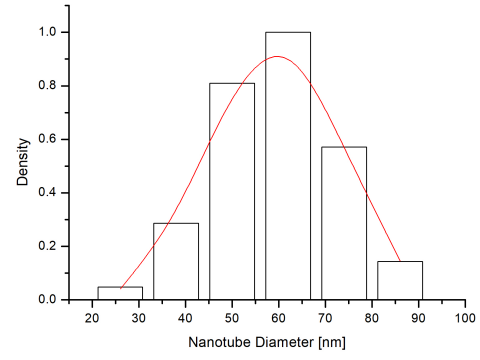
Table 3.1: Mass measurements without electric field for $Re=300$.

ϕ	HAB [mm]	t [min]	Re	Mass [mg]
1.6	10	15	300	5.1
1.6	10	15	300	4.9
1.6	10	15	300	5.4
1.6	10	15	300	4.7
1.6	10	15	300	5.3

SEM images clearly allow the identification of the products yielded as tubular structures with no apparent orientation. Using iTEM software, an expected value for the diameter of the nanotubes was calculated via the implementation of a normal distribution based on 60 values of measured diameters. Both the SEM image and nanotube diameter distribution are visible in Figure 3.3.



(a) SEM

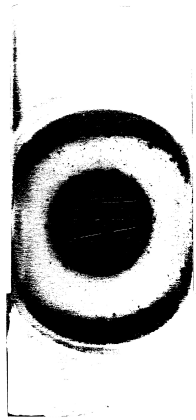


(b) Diameter Distribution

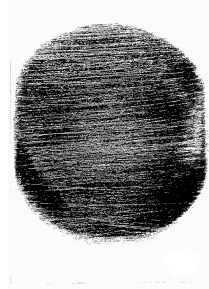
Figure 3.3: SEM image at 10K magnification of CNT produced without electric field and respective normal distribution of the diameters.

From the normal distribution, the expected diameter value for the carbon nanotubes produced without application of an electric field is 60 nm. It is also important to note the wide span of diameters obtained for these conditions, with values ranging between 30 nm and 84 nm.

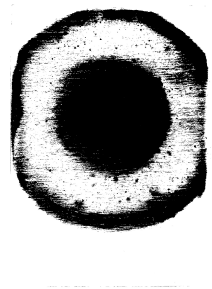
The masses and the deposition areas for the different Reynolds analysed in this work were also studied. The latter were extrapolated from binarized photographs of the substrate after deposition using the software ImageJ. The resulting images for the three different cases are available in Figure 3.4.



(a) 250



(b) 300



(c) 400

Figure 3.4: Binarized photographs of deposited substrates for the different Re and 0V. The black areas correspond to deposited CNT.

In Table 3.2 are displayed the values of mass production and deposition areas for Reynolds numbers of 250, 300 and 400 with no voltage applied for a sampling time of 15 minutes.

Table 3.2: Mass and deposition area measurements without electric field for $Re=250$, 300 and 400.

ϕ	HAB [mm]	t [min]	Re	Mass [mg]	Area [cm ²]
1.6	10	15	250	3.8	9.52
1.6	10	15	300	5.2	19.46
1.6	10	15	400	5.9	19.74

To confirm that in fact the nanotubes produced are mainly composed by carbon atoms, XRD analysis was performed on synthesized nanotubes. To prepare the sample for analysis, the carbon nanotubes were synthesized in the flame environment and removed from the substrate to isolate a powder of CNT according to the procedure mentioned in Section 2.6. The result is visible in Figure 3.5.

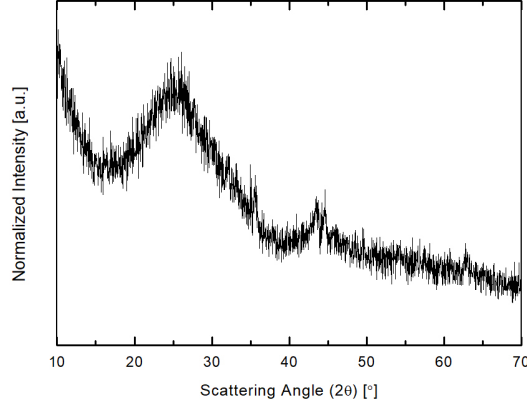


Figure 3.5: Result of the X-ray diffraction of the carbon nanotubes produced.

According to [100], the peaks observed at 26.07° and 44.61° correspond to graphitic peaks related to the (002) and (100) lattices, respectively. The (002) peak is associated with the inter-planar graphitic distance of 0.34 nm, which is the characteristic separation between the concentric tubes in MWCNT. This fact conjugated with the diameters registered ultimately confirm that MWCNT are the resulting products of our experimental conditions.

3.3 Electric Field Simulation

In an ideal situation, the electric field generated between two parallel plates at a very low distance is uniform and perpendicular to the plates, leaving the positive charged plate to the grounded plate. However, in our apparatus the lower plate in the theoretical approach is replaced by the burner assembly which has a non uniform geometry and does not allow the calculation of the electric field magnitude by the simple formula utilized in Section 2.7.7.

We are interested in studying the effect of the electric field on the yielded carbon nanotubes, hence it is important to fully understand not only the magnitude, but also the direction of the electric field. With this in mind, a simulation was performed. A 3D CAD model of the top section of the burner was designed, and a stainless steel plate was introduced on top at HAB=10mm to create a realistic assembly of our setup. The electric field was simulated for $\pm 1V$, $\pm 10V$, $\pm 20V$ and $\pm 30V$.

From the results we confirmed that the electric field near the substrate was uniform and perpendicular to the plate. The resultant electric force has the same direction as the electrostatic field meaning that carbon nanotubes will be under a pulling force while growing with positive voltages and under compressive forces for the opposite polarity. The magnitude of the electric field suffers slight variations due to the non-uniform geometry of the burner and there is also an edge effect that causes discrepancies at the

substrate limits. Magnitudes of E implemented are visible in Table 3.3.

Table 3.3: Average magnitude of E for the different voltages applied based on simulation results.

ΔV [V]	E [V/m]
1	74.4
10	771.4
20	1629.6
30	2414.3

3.4 Influence of Electric Field on Production of CNT

3.4.1 Mass Yield

After testing the Reynolds numbers at which an envelope flame configuration could be established, it was decided to assess the influence of the electric field on mass production at three different Reynolds. 250, 300 and 400 were the values selected, seeing that the outlet velocities increase with Re and that allows the study of the interaction between convection forces of the flow and electrostatic forces, ultimately analysing the behaviour of the mass production when under influence of voltage bias. The tests performed are listed in Table 2.1.

Re number of 250 provides an outlet velocity for the mixture of 0.19 m/s, which translates into the lowest convective forces between the Re values selected. The evolution of mass production with the variation of voltage is depicted in Figure 3.6.

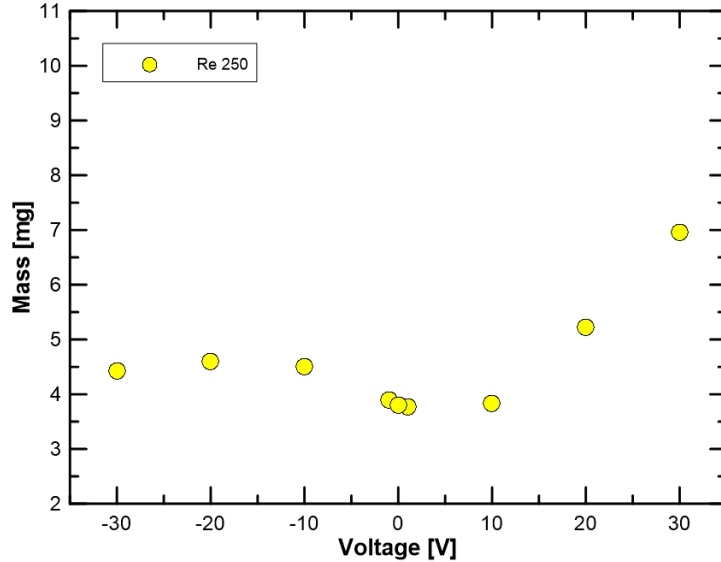


Figure 3.6: Mass measurements for production of carbon nanotubes with ± 1 , ± 10 , ± 20 and ± 30 V, for a Re number of 250.

From the plot some conclusions are withdrawn. The average value for mass production with no voltage was 3.8 mg, which is in line with the value obtained for both 1 and 10 volts. This indicates that for $Re=250$, a positive electric field with magnitude lower than 10V produces no effect on the mass

yielded for the working conditions. The situation changed when 20V were applied to the substrate, with the mass production increasing from 3.8 mg to 5.2 mg. Further augment in the potential difference to 30V provided 7 mg of CNT. This translates to a 37% and 84% increase in mass production, respectively. In regards to negative voltages, despite a very slight increase in mass being documented, there was no clear relationship between the variation of the electric field intensity and mass weighed after 15 minutes. The average mass measurements for -1, -10, -20 and -30 were 3.8, 4.5, 4.6 and 4.4 mg, respectively. It is concluded that positive voltages have a beneficial effect on the mass yield and 30V bias is the ideal situation to obtain significant increase in the mass of carbon nanotubes produced.

To perform a comparison with the results obtained by [93], a Re number of 300 was selected. For this value the outlet velocity of the mixture is 0.23 m/s, thus having slightly higher convective forces than the previous case. The same tests as above were performed and the results are visible in Figure 3.7.

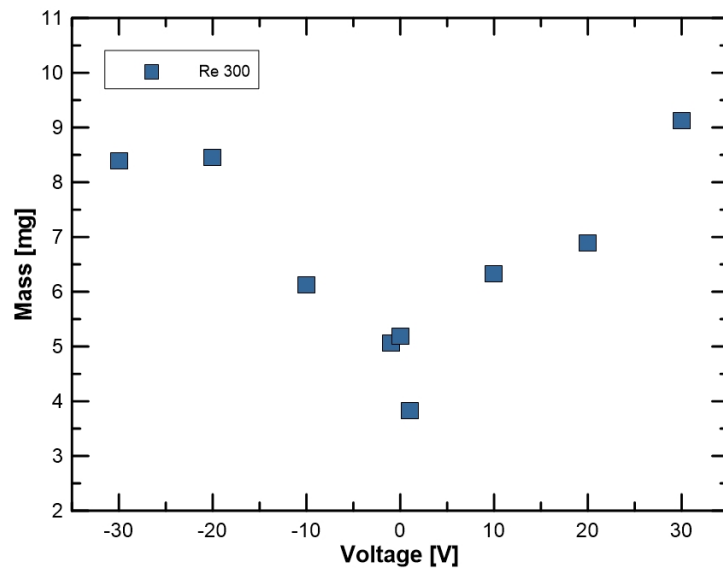


Figure 3.7: Mass measurements for production of carbon nanotubes with ± 1 , ± 10 , ± 20 and ± 30 V, for a Re number of 300.

Again it is important to remember that the value for mass production without voltage bias for this condition was 5.2 mg. Starting with the positive side, applying 1V to the stainless steel plate resulted in decrease of mass production from 5.2 mg to 3.8 mg, although this value is most likely an error associated with the burner. Immediately after igniting the mixture, the flame shape was not adequate and the burner had to be reignited. This was later understood but some erratic values were registered. Subsequent increases in the voltage applied to the substrate transduced into a mass yield increment. At 10V, the yield was 6.3 mg (22% increase), at 20V 6.9 mg (33% increase) and at 30V 9.1 mg (75% increase) were obtained. Contrarily to $Re=250$, for negative potential difference, the tendency of the mass produced was to raise when the magnitude of the electric field was raised (absolute value). At -1V the electric field proved to have no effect on the mass production of carbon nanotubes. Lowering the value to -10V, an increase of 0.9 mg (17%) was obtained. For -20V, 8.5 mg of CNT were measured and stagnation appeared to occur, since the mass for -30V remained almost constant at 8.4 mg, representing a 63.4% raise. With these results, it is concluded that $Re=300$ is relatively insensitive to polarity as well as requiring lower

positive voltages to register a significant mass increase, 10V against 20V. Again, a voltage bias of 30V revealed itself as the optimal condition to improve the production of carbon nanotubes in the flame environment. Comparing the maximum percentage increases between Re 250 and Re 300 when 30V are applied, by increasing Reynolds the maximum increase lowered from 84% to 75%.

The last value of Reynolds subjected to this same experiment was 400. With an outlet velocity for the mixture of 0.3 m/s, the respective flow has the highest convective component from all the values presented above. Again, the voltage was varied between -30V and 30V. The results are available in Figure 3.8.

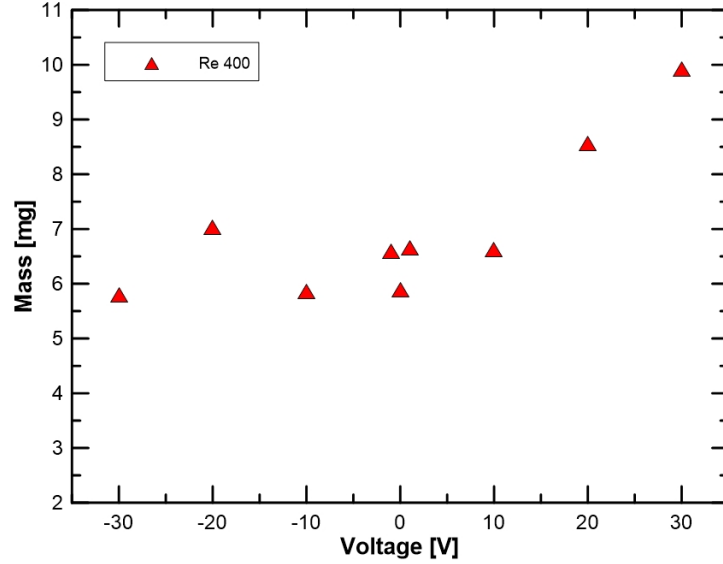


Figure 3.8: Mass measurements for production of carbon nanotubes with ± 1 , ± 10 , ± 20 and ± 30 V, for a Re number of 400.

The reference value at 0V for $Re=400$ is 5.9 mg. Electrifying the substrate with 1V yielded 6.7 mg of carbon nanotubes. For 10V, the increase in voltage did not reveal any gains in mass compared to 1V, with a result of 6.6 mg. Significant effects appeared when 20V and 30V were applied, with production of 8.6 and 9.9 mg for each situation. On the negative side of the voltage axis, the situation was resemblant of the $Re=250$ case. There is no defined relationship between voltage variation and mass production. The mass results for -1, -10, -20 and -30 are 6.6, 5.9, 7 and 5.8 mg. The maximum increase was achieved for -20V, a 19% gain, while for -30V a decrease in mass production was verified. The optimal condition to better the flame synthesis of CNT at $Re=400$ is again charging the substrate with 30V, providing a maximum gain of 68%.

The results above are intriguing, seeing that for negative voltages there is a difference between the outcomes obtained with different Re values. For $Re=300$, negative bias has the capability of increasing mass production in significant amounts, although not as much as the positive equivalents. For $Re=250$ and $Re=400$ that was not the case. Even if small increments in mass production are observed, as registered for $Re=250$, for intense negative electric fields at -20V and -30V the results can not be compared with the positive cases. In search for an explanation for the statements above, the deposited areas for the different conditions were investigated, particularly to understand the evolution when negative voltages are varied and the difference in behaviours between Reynolds. The deposition areas were extrapolated

using the same procedure as in Section 3.2. The resulting images for the three different cases are available in Figures 3.9, 3.10 and 3.11. In Table 3.4 are the values of the areas corresponding to each image.

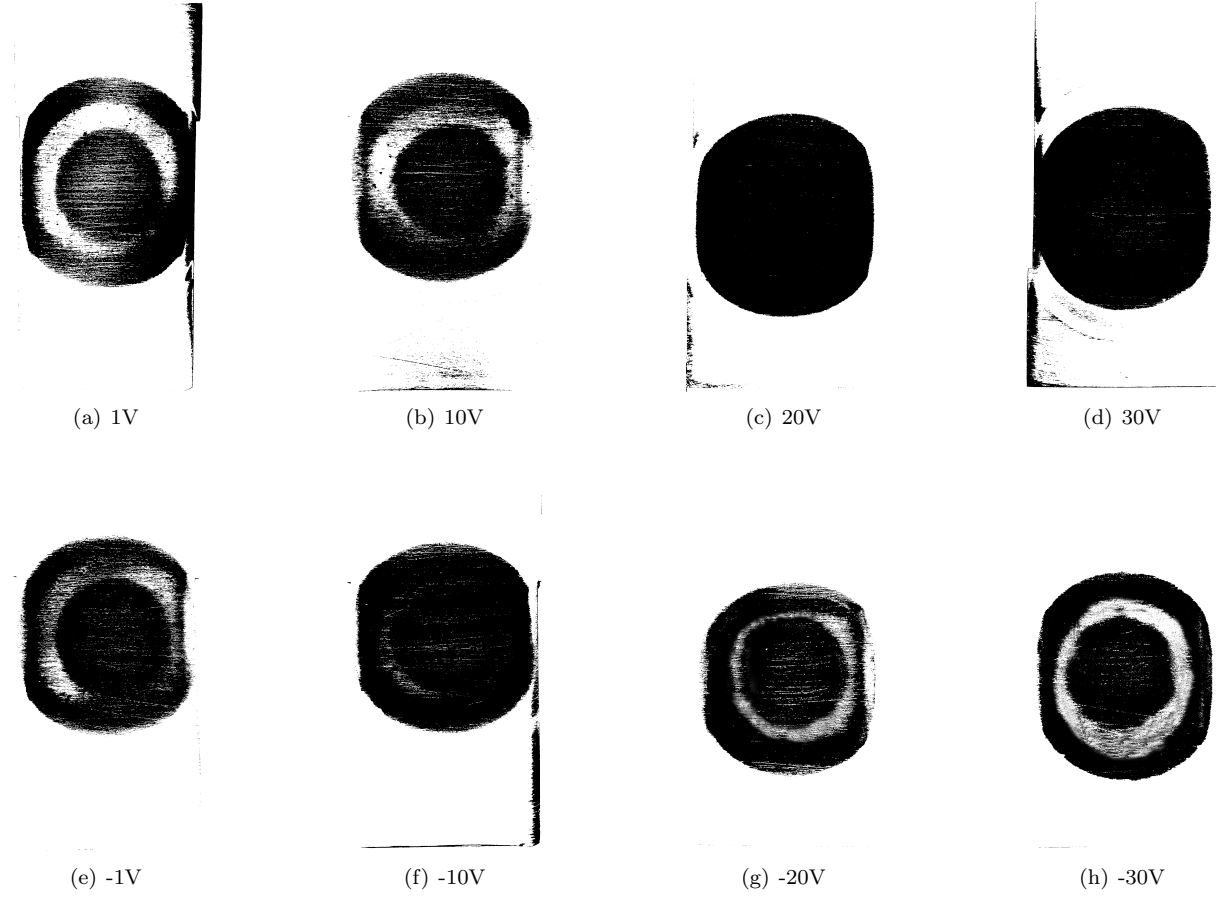


Figure 3.9: Binarized photographs of deposited substrates for the different voltages and $Re=250$. The black areas correspond to deposited CNT.

For $Re=250$, when the substrate is positively charged it is observed that the area covered by carbon nanotubes increases when the voltage raises. Interestingly, the shape of the deposited area also changes when 20V are applied to the substrate. For 1 and 10V, the deposited area consists of a circle in the centre of the substrate of approximately 1 cm radius, and an external annular area with thickness of ≈ 3 to 5 mm. When the voltage applied is 20 and 30V, not only the value of surface coverage calculated increases, the shape transforms to a uniformly covered area with significant increase in mass, as observed in Figure 3.6. For negative bias, the shape of the deposited area coincides with that described for 1 and 10V. Contrarily to the positive voltages, the shape is constant throughout the whole negative voltage range tested. Therefore, the deposited area values calculated remain similar, ranging between 9.69 and 10.59 cm² and explaining the absence of significant mass increments for these conditions.

$Re=300$ is a particularly interesting case. The shape of the deposited area at lower voltages (1 and 10V) differs from the situation for Reynolds 250, with the circle and external crown described for the lower Re being replaced by a notoriously more uniform area. The deposited area is now resemblant to the ones visible in 3.9 (c) and (d), however, in some cases the centre of the sample is where less CNT are observed, completely the opposite of what happened at lower Reynolds. The higher the voltage applied

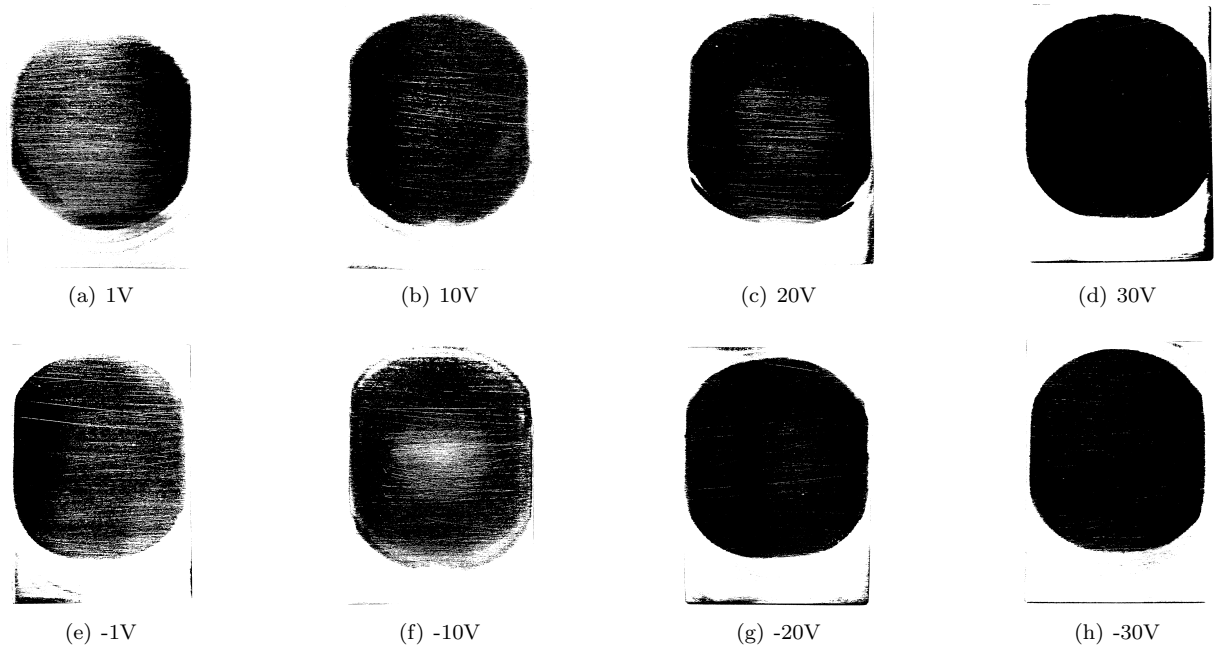


Figure 3.10: Binarized photographs of deposited substrates for the different voltages and $Re=300$. The black areas correspond to deposited CNT.

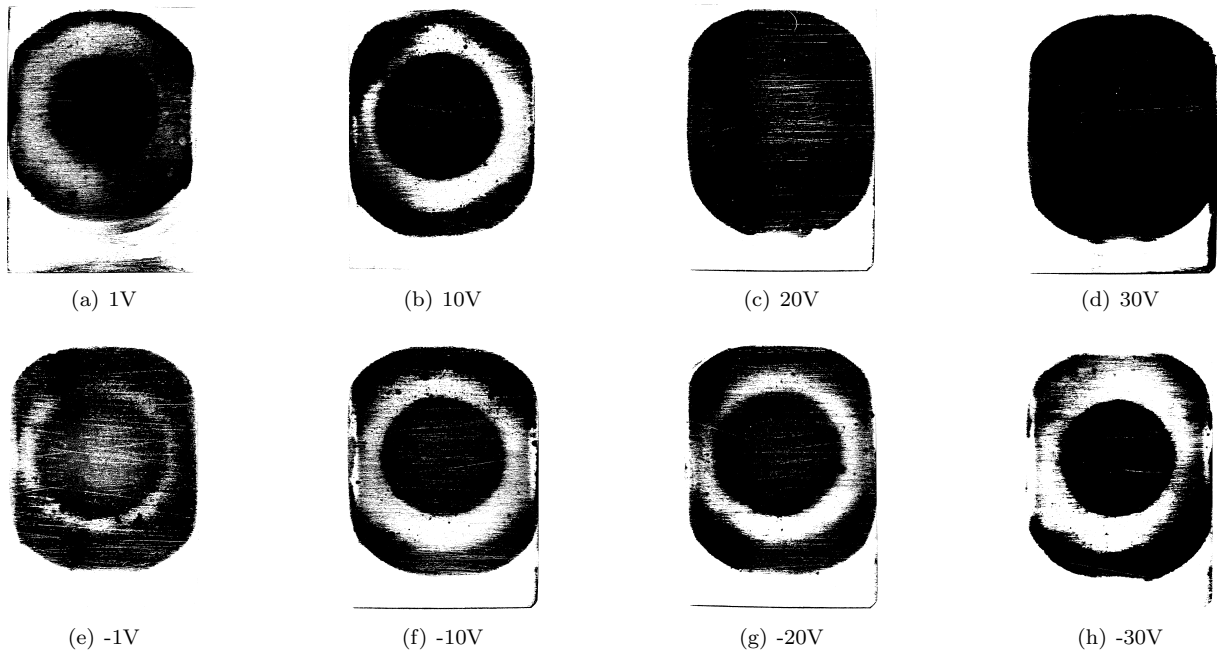


Figure 3.11: Binarized photographs of deposited substrates for the different voltages and $Re=400$. The black areas correspond to deposited CNT.

the denser the deposited area becomes, coherent with the mass increment obtained. The situation is similar when the electric field is inverted, the deposited area is somewhat uniform for all the voltages tested, with higher density of nanotube deposition for higher magnitudes of electric field.

Lastly, $Re=400$ was subject to evaluation. Starting with the positive potential differentials, for 1V and 10V the shape of the deposited area is similar to that described for the same voltages at $Re=250$, with the presence of carbon nanotubes in the centre and in an external crown. A remarkable increment

Table 3.4: Deposition areas calculated for ± 1 , ± 10 , ± 20 and ± 30 volts for a Reynolds number of 250, 300 and 400.

ΔV [V]	Area [cm ²] ($Re=250$)	Area [cm ²] ($Re=300$)	Area [cm ²] ($Re=400$)
1	9.33	18.84	19.91
10	9.10	21.45	20.67
20	11.57	21.71	25.83
30	12.56	24.40	27.38
-1	9.69	19.58	20.94
-10	10.59	20.57	19.87
-20	9.183	22.17	21.15
-30	10.10	22.03	19.12

in deposited area arises when 20V are applied, and likewise reported for $Re=250$, a modification of the deposited area is visible. The substrate is now uniformly covered with carbon nanotubes. This tendency continues, and for 30V the plate has a large and dense circular deposition. The evolution of the areas transduces to the mass evolution. When the trials are conducted under the presence of a negative voltage, the situation is again very similar to that of $Re=250$. The deposition area remains in a confined interval for all the conditions and the shape modification of the area does not occur, hence why there are no significant increments in mass production as for positive voltages.

On a general scope, observing the deposition areas, the higher the flow velocities the more carbon species are available and hence the increase in deposited areas. However, it is noticeable that the behaviours of the flame deposition areas are identical for $Re=250$ and 400. The depositions are very similar in shape and for both instances there is a modification of the deposited surface when 20V or more are applied. Regarding negative voltages there is no change reported, leading to the conclusion that only positive bias has the ability to promote that change. Therefore the mass increments are only obtained when this shape change is viable. The case for Reynolds 300 is unique in the behaviour it presents. The deposition area is different right from the start, with a better distribution of carbon nanotubes deposition, indicative that this flow has the optimum conditions in terms of surface coverage for the setup employed in this study. The different deposition behaviour somewhat isolates this case from the remaining, thus the existence of a different pathway for the mass deposition when negative voltage is applied. The flame shape, temperature and flow properties characteristic for Re 300 are responsible for altering the mechanism of deposition and causing a different behaviour under the influence of electric field.

According to the work of [101], the breakdown of hydrocarbon molecules in the reaction zone culminates in the appearance of electronically unbalanced free radicals such as CH^- , $C\equiv C^-$ and C^- . These molecules suffer attraction from the positive plate and ultimately are the reason for the improvement and enhancement of mass production. They also reported that higher voltages yielded better results, when comparing the application of 5V and 24V. This results are coincident with the ones obtained throughout the experiments in this study, and also explain the change in shape of deposited area observed for $Re=250$ and 400. Voltage induces attraction that allows carbon nanotube growth in areas where no CNT appears in insufficient or absent electric fields. Our results also suggest that for the combination of substrate,

carbon precursor and flame configuration adopted, a voltage equal to or greater than 20V is enough to promote attraction of carbon species. For $Re=300$, the attraction of carbon species translates to a denser deposition area or, in other words, a darker area visible in Figure 3.10. So far there is not an explanation for the enhancement that may occur for negative voltages. Due to the lack of consistency in mass production behaviour, for further experiments this report focuses exclusively on $Re=300$ and positive voltages.

To conclude, for all the Reynolds numbers, the best outcome in improving the mass production of carbon nanotubes was achieved when 30V were applied to the substrate while keeping the burner grounded. The maximum increments obtained for $Re=250$, 300 and 400 were 84%, 75% and 68%, respectively.

3.4.2 Morphology of CNT

For $Re=300$ the analysis of the influence the electric field exerts on the produced CNT was explored beyond mass analysis. Electronic microscopy with diameter measurements was performed. The samples subject to investigation were prepared for positive voltages since those provided the best results, with application of 5V, 20V and 30V. The SEM images were taken in the centre of the samples with 10000x magnification and are available in Figures 3.12, 3.13 and 3.14 with the respective diameter distributions.

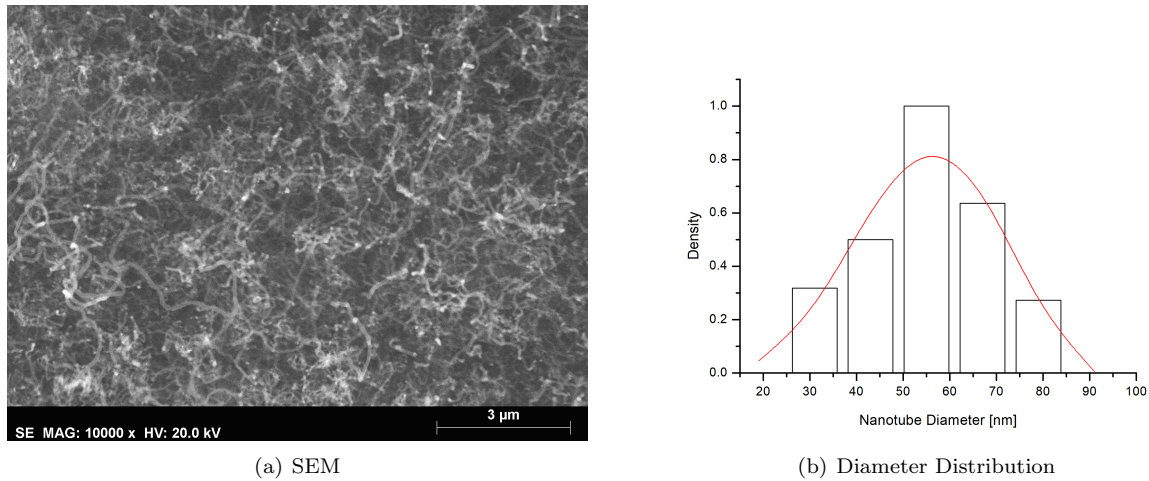
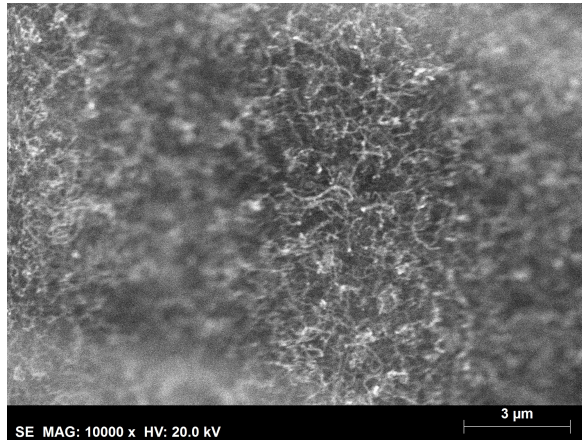
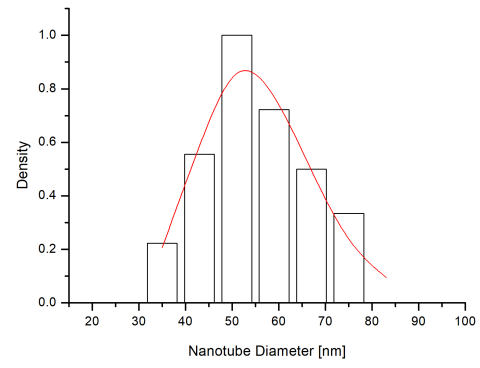


Figure 3.12: SEM image and diameter distribution for 5V.

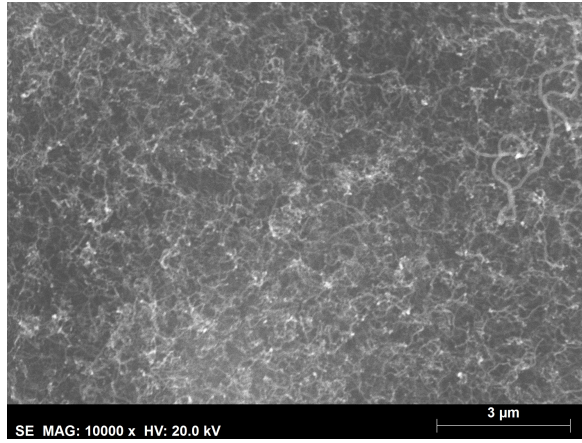


(a) SEM

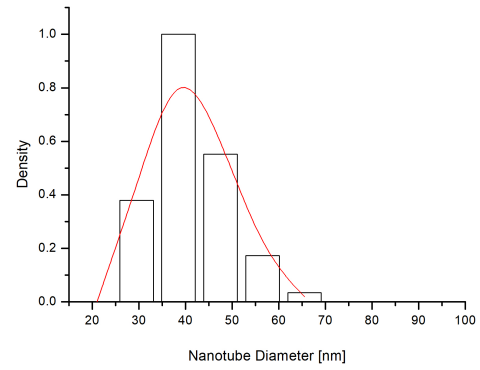


(b) Diameter Distribution

Figure 3.13: SEM image and diameter distribution for 20V.



(a) SEM



(b) Diameter Distribution

Figure 3.14: SEM image and diameter distribution for 30V.

It is important to remember the distribution of diameters with no electrification, with an expected value of 60 nm and ranging between 30 nm and 84 nm. For the situations presented above, expected diameters and range is available in Table 3.5.

Table 3.5: Expected diameters and diameter intervals for $\Delta V=5, 20$ and 30.

ΔV [V]	Expected Diameter [nm]	Diameter Range [nm]
5	56	29 - 77
20	52	33 - 76
30	40	26 - 67

From the data above it can be extrapolated that the expected diameter of the nanotubes decreases with higher voltage values. This effect is significant when 30V are applied to the substrate and this was clear early on by observing the SEM images, where narrower nanotubes appeared. Comparing Figure 3.3 and Figure 3.14 it is visible that higher number of nanotubes are found and that for 30V they also seem to have more uniform diameters.

The diameter of the nanotubes is influenced by the catalyst particles that are formed on the surface of

our substrate. Since in this experiment there is no preparation of a catalyst to be introduced in the flame environment or to be deposited on the substrate, the diameter of the nanoparticles is not controlled prior to reaction. In direct substrate catalyst formation, the origin of the catalyst nanoparticles is complex. In the SEM images captured some bright catalytic particles can be visualized on the tips of some carbon nanotubes, however, that is not the case for the entirety of the sample. This means that base growth also occurs. Since there are no external catalysts introduced, it is assumed that the interaction between substrate and catalyst is strong, being that the catalyst is an integral part of the substrate. According to [102], for CNT growth directly on stainless steel, both mechanisms are also reported, with the type of structure that acts as catalyst being the differentiating factor. For base growth they describe the presence of nano-hills in the metal surface that are most likely in a quasi liquid state. These nano hills derive from the surface roughness of the metal substrate. The distribution of diameters characteristic of the nano-hills is wide, coherent with the variety of diameters obtained in this work. The tip growth is resultant of catalytic particles created by a mechanism denominated as metal dusting. Metal dusting is defined by Young et al. [103] as an aggressive corrosion process of the metal surface caused by the carbonaceous rich atmosphere combined with high temperatures. For austenitic stainless steel, the mechanism is complex and involves three different types of metal dusting described by Szakalos [104]. Firstly, a fast transfer of carbon from the flame environment into the metal surface leads to the formation of a cementite plus chromium-depleted austenite layer on the surface. Then, both Type-III and Type-II metal dusting mechanisms are present. The first one involves dissolution of the Cr-depleted austenite and selective oxidation by oxygen and free carbon, ultimately resulting in austenitic metal nanoparticles and oxides. The latter involves graphitization of the cementite layer resulting in fragmentation and ultimately yielding cementite nanoparticles. To conclude, the nanotube formation is described by the author as a Type-IV dusting mechanism, which represents the catalytic deposition of carbon in the metal dust nanoparticles yielding carbon nanotube growth.

The diameter distribution of the particles formed as a result of the methods described above is hard to predict and control, since there is a high dependency on the structure and composition of the substrate. Nevertheless, it is also stated that the process relies on electron transfer between the carbon containing species and the bulk metal. This transfer may be altered by the charge applied to the substrate, ultimately resulting in catalytic nanoparticles with different attributes and causing the alteration in diameters observed. Not only that, but if the formation process of catalytic nanoparticles is influenced, this can also be the cause for the increase in deposition areas and mass production, however, definite conclusions are out of the grasp of this report.

Another important aspect to consider is that if the particle is required to be in a liquid phase, temperature plays an important role on whether a catalyst particle is active or not. According to [105], the melting temperature of small nanoparticles is lower than the respective bulk metal and given by Equation 3.1:

$$T_p = T_0 - \left(\frac{2T_0}{\Delta H_{fusion} \rho_s r} \right) \left(\sigma_{sl} + \left(1 - \frac{\rho_s}{\rho_l} \right) \sigma_l \right) \quad (3.1)$$

where T_0 stands for the bulk melting temperature of the metal used, ΔH_{fusion} is the latent heat of fusion,

σ_{sl} the solid-liquid interfacial energy, σ_l the surface energy of the liquid phase and r the particle radius. On the other hand, ρ_s and ρ_l represent the density of the solid and liquid metal, respectively.

From the formula it is concluded that the bigger the particle, the higher the melting temperature. This indicates that temperature has a large influence on the catalyst activity and consequently on the resulting carbon nanotubes. It is therefore of relevancy to perform a temperature analysis with and without voltage to discern if it is the cause for the variation in diameters or mass increase. It is important to note that assuming the particle is in liquid form is adopting the VLS model, which is controversial especially for MWCNT and for the nanotube diameters we obtain, that can go as high as 80 nm. If the particle remains in the solid state, the temperature effect on the diameter is not consensual, with multiple outcomes being reported. Some authors claim higher temperatures translate to higher diameters, while others claim the opposite [55]. Nonetheless, temperature variations affect the diameters and measurements are important.

Temperature Distribution

Being a critical parameter on nanotube synthesis, it is essential to understand the effect the electric field has on the temperature of the flame environment. Measurements were taken at 6 different locations spreading the deposition area and immediately below the substrate surface without contact between the thermocouple and the substrate. The points were denominated A, B, C, D, E and F and are visible in Figure 3.15.

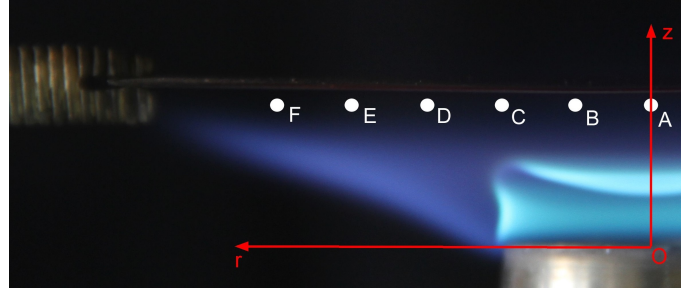


Figure 3.15: Locations for temperature measurements. The coordinates for each point (r,z) are: A(0,10), B(5,10), C(10,10), D(15,10), E(20,10), F(25,10).

The temperatures were measured without electric field and with both 20 and 30V bias. The results can be assessed in Figure 3.16.

In general, the synthesis temperature is in the 900°C to 1050°C interval. In the centre of the sample values of $\approx 1010^\circ\text{C}$ are measured, increasing to $\approx 1040^\circ\text{C}$ on point B located 5 mm away from the centre. From here the temperature decreases with further distance from the origin, with values at the edge of the deposition area (point F) sitting at $\approx 900^\circ\text{C}$. These values are coincident with [67] for the synthesis of MWCNT with rich propane flames and the nanotube production window defined by [78]. Temperature measurements indicate that a moderate electric field has no effect on temperature. For 0, 20 and 30 volts, temperature values are extremely coincident, this indicates that gas phase in the reaction environment is not altered. The facts presented are coincident with the results of Masunaga et al. [106], who claimed that the effects exerted on CNT production by the presence of an electric field did not arise from alterations on the gas distributions or temperatures within the flame environment, but were instead caused by the

presence of the electric field itself. With this conclusion, temperature variations are not the cause of the mass increments reported in Section 3.4.1 nor the diameter alterations observed.

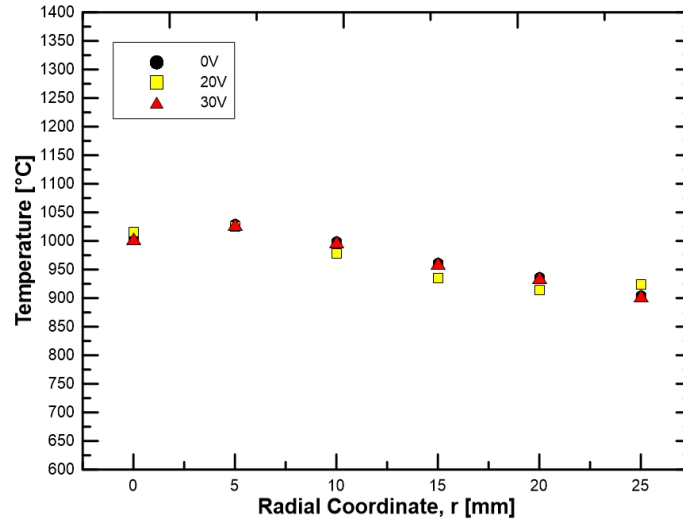


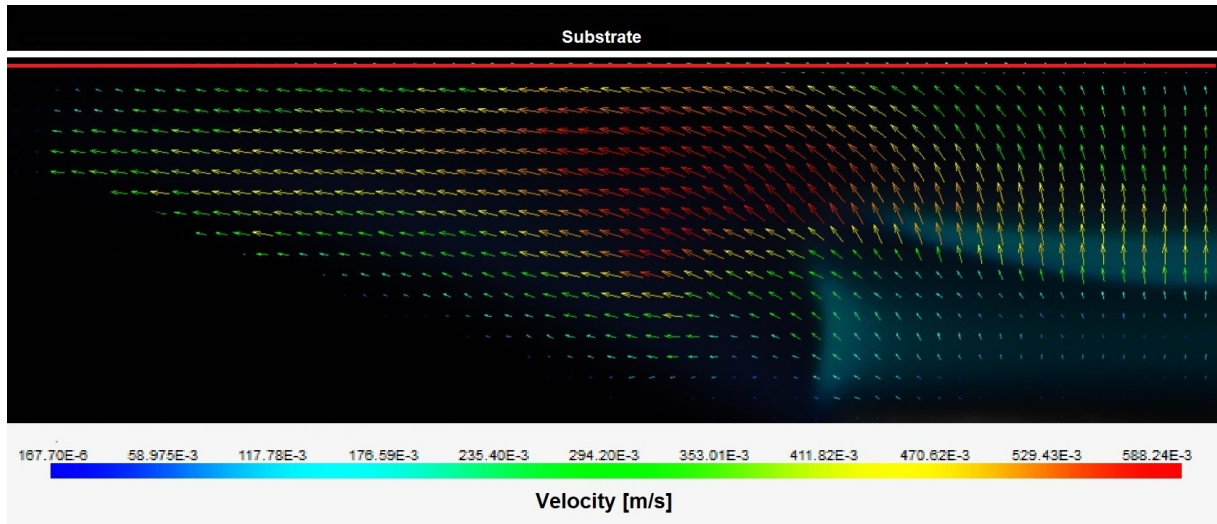
Figure 3.16: Temperatures measured at the six different locations with 0V, 20V and 30V applied to the substrate.

Velocity Fields

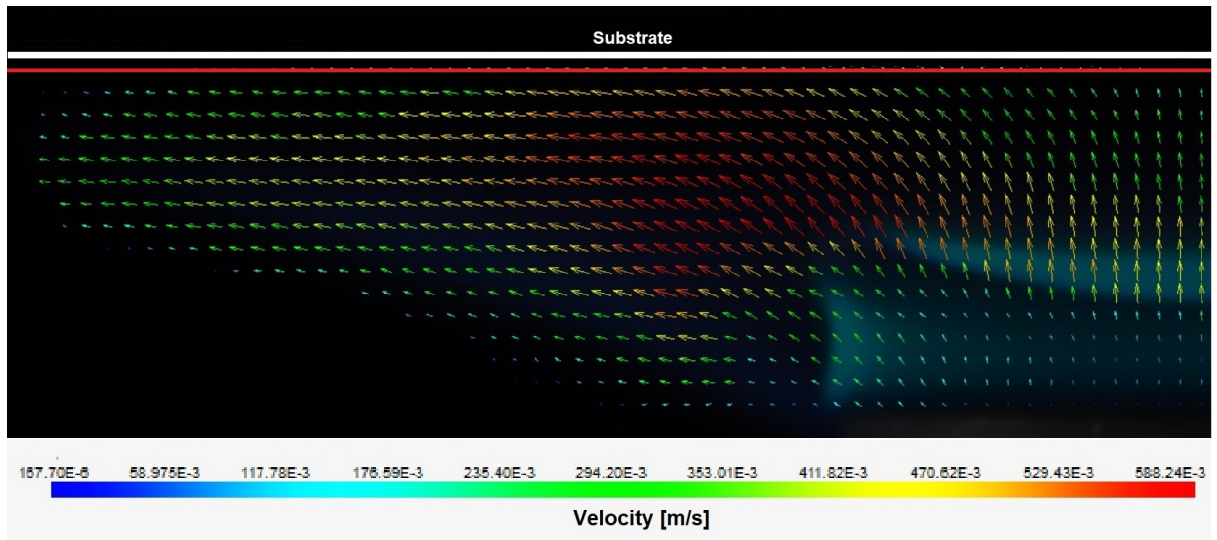
The flow characteristics are rarely debated in the scientific community when the mass production of carbon nanotubes is of concern. Flow properties may influence residence times of carbon materials near the substrate and affect the dynamics of carbon diffusion through the catalyst. Most of the available literature focus on CVD or AD, which are characterized by much lower velocities. Using PIV measurements can be useful to understand whether the uniform electric field affects the flow and ultimately try to comprehend if that is the cause for the increase in mass production achieved.

From previous work performed with the same experimental setup [93], it was concluded that the deposition of carbon nanotubes initiates where lower velocities are found. In fact, when no voltage is applied, for sampling times under 5 minutes the areas where initial carbon nanotube formation occurs are located at the centre of the substrate, $r=0-10$ mm, and an outer ring located at $r=18-20$ mm. If the velocities are low, it is deductible that residence times for carbonaceous materials are high and hence why the deposition is facilitated. Velocity is then important towards the CNT growth process and deposition areas. When high voltage is applied, the deposition area even at initial time frames is altered and, for 20V and 30V, CNT cover the substrate spanning all the radial coordinates between 0 and 20 mm. Even for a sampling time of 15 minutes, the difference between deposition areas is still noticeable when voltage is applied, as depicted in Figure 3.10.

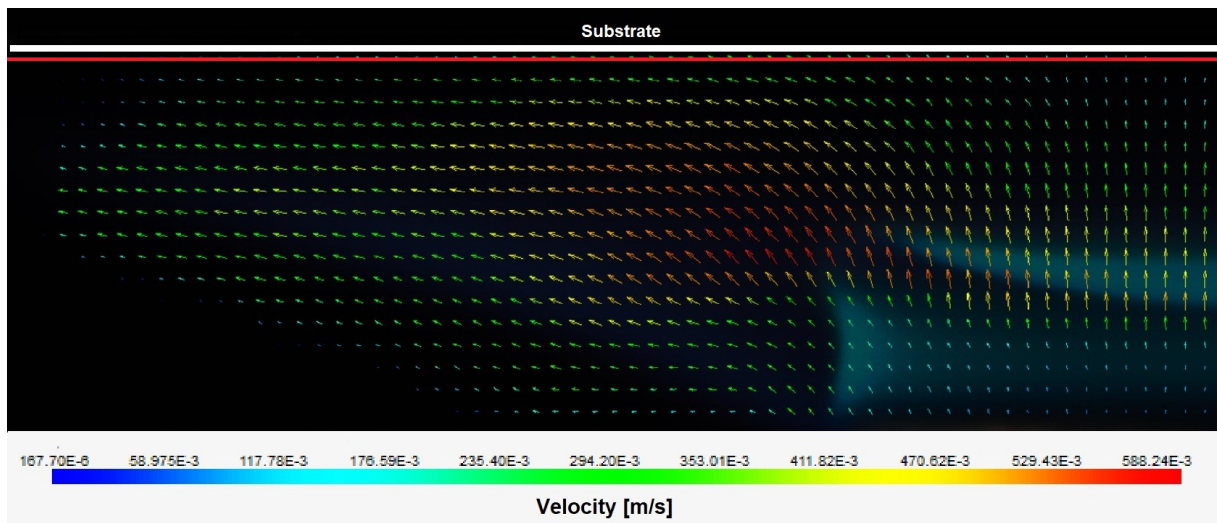
In order to explain the effect reported above, PIV measurements were performed to study the alterations on the velocity fields induced by possible ionic winds. Negative voltages were subjected to this analysis, since useful data might be extracted. The results for 0V, 30V and -30V are available in Figure 3.17, while the other conditions tested can be visualized in Appendix A.



(a) 0V



(b) 30V



(c) -30V

Figure 3.17: 2D velocity map for the flow characterized by Reynolds number of 300 and 0, 30 and -30 V.

The velocity vector maps obtained are fairly similar in all the conditions which is indicative that the

electric field magnitude is not sufficient to cause severe ionic winds and alter the flow. The flame shape was also not altered when the electric field was applied, something that happens when voltages in the order of thousand volts are applied [107]. It is important to note as well that retrieving data on sampling times of 5 minutes or 40 minutes yields the same velocity vector maps, indicating that the flow is not altered over time.

Seeing that the deposition takes place near the substrate and that the process is occurring at nanoscales, the velocity profile near the stainless steel plate is where possible alterations would have repercussions. It is therefore important to study those in better detail. Through the software used, Dantec Dynamic, it is possible to retrieve a plot of the velocity values for a specific z coordinate for the entire range of radial coordinates. The values were taken as close as possible to the substrate, along the red line visible in Figure 3.17. Noting that the flow is characterized by radial symmetry, the resulting plots are presented in Figure 3.18 for half the radial coordinates.

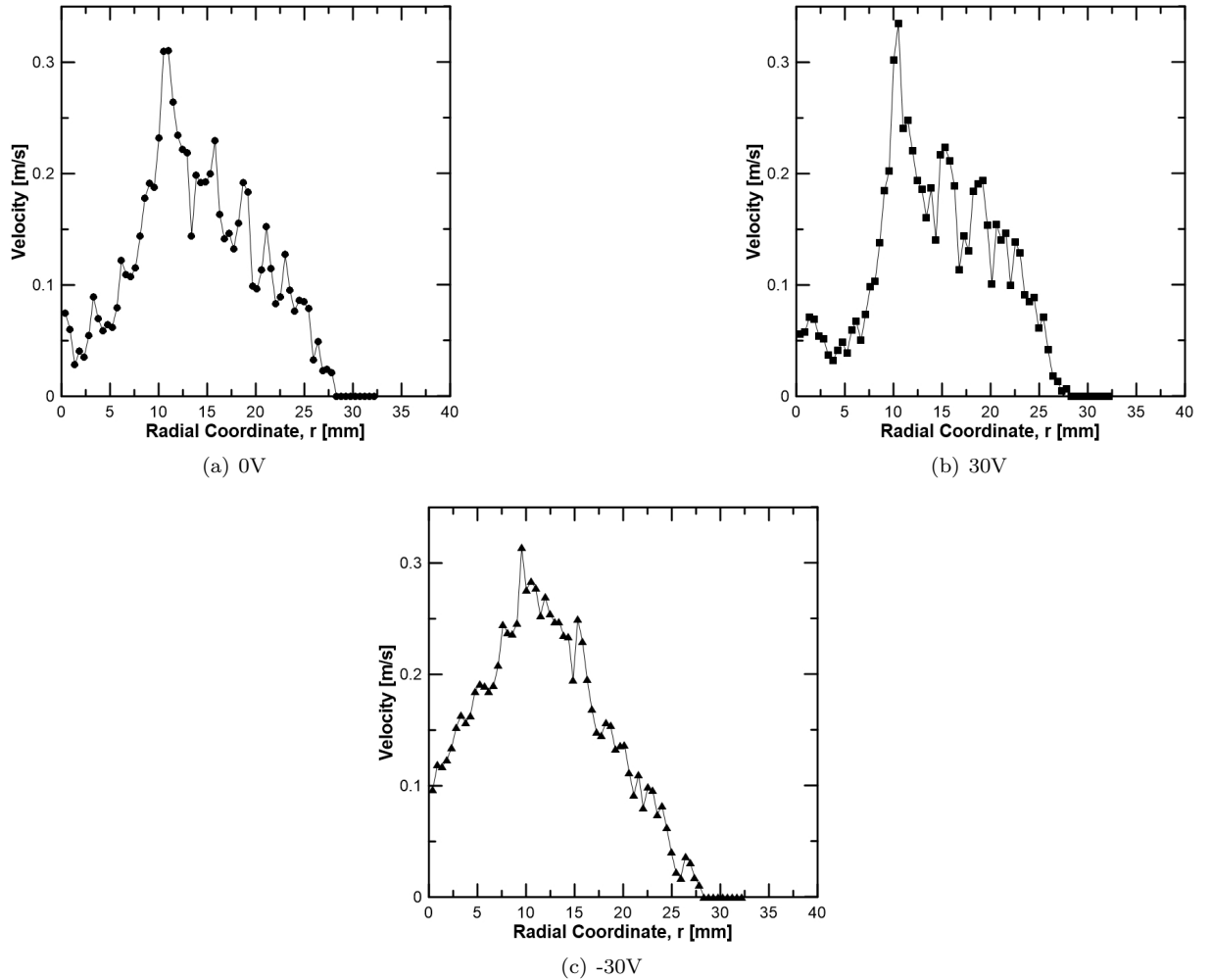


Figure 3.18: Velocity plots near the substrate for 0V, 30V and -30V.

Despite minimal alterations that can be attributed to the software, time of acquisition and other factors, the values obtained for the three conditions are in agreement with each other. In the centre, $r=0$ mm, the velocities approach 0 m/s because of the stagnation point in the plate. From there the velocities increase up to 0.31 m/s, 0.33 m/s and 0.31 m/s for 0V, 30V and -30V, respectively. Those maximum

values are obtained at $r=10.5$ mm. For increasing radial coordinates the velocity decreases until $r=27.5$ mm where the velocities are approaching 0 m/s.

Deposition occurs along the whole radial coordinates between 0 and 20 mm, and after 15 minutes there is high density of carbon nanotube deposition. The low amount of variations in the velocities characterizing the flow in the flame environment leads to the conclusion that changes in the flow are not the cause of the increments registered in mass production.

3.4.3 Vertical Alignment

Electric field was initially implemented to synthesize vertically aligned carbon nanotubes with less impurities as exposed in Section 1.2. From the scarce experiments performed on flame synthesis with DC electric field, aligned carbon nanotubes are attainable with low voltage. By simple observation of the SEM images obtained throughout our experiments, the carbon nanotubes produced do not show signs of alignment. The products appear randomly orientated and with the electric field having no influence on this parameter. There are several relevant points to discuss.

Firstly, only top view images were possible to obtain with our substrate and SEM equipments. Ideally cross-section views would reveal in more detail the different orientations along the electrostatic force acting plane. The SEM images presented in [87] indicate that from a top perspective the alignment may be very difficult to perceive. Also, only in some exclusive areas of the samples VACNT are present. The same perception is obtained from [84, 88].

Secondly, it is important to delve into detail on the catalyst and growth mechanism. Xu et al. [87] only achieved vertically aligned nanotubes when employing transition metal catalytic probes. For an iron probe no alignment was obtained. The other authors [84, 86, 88] also used catalytic probes of Nickel or apply an external catalyst to stainless steel, while a tip growth model is commonly reported. That is coherent with the statement that tip growth is necessary for vertical alignment. In this study, a stainless steel substrate without any external catalyst is inserted in the flame, and both the tip and base growth mechanisms are observed. It is therefore likely that this setup does not grant the formation of VACNT.

Finally, it is also important to note that our substrate and deposition areas are significantly larger than those found in other experiments. The focus of most authors is always on the nanotube itself and how its characteristics evolve with varying environments. In this study high mass production of nanotubes is the priority. The higher quantity of carbon nanotubes and large areas of study may decrease the effectiveness of the electric field in the alignment of carbon nanotubes.

3.4.4 Time Analysis

Flame synthesis has the advantage of being a continuous process with mass production capabilities. It is important to understand the growth dynamics of carbon nanotubes over time so that ideal sampling times can be defined. CNT growth is dependant on the catalyst particles and their ability to adsorb and diffuse carbon. As time passes, the solubility limits of the catalytic particles are reached, they become fully covered with carbon and diffusion no longer occurs. At this point the catalytic activity ceases and

the catalyst is said to be deactivated, without any growth of carbon nanotubes from that point onwards. Based on this information it is predicted that CNT growth ceases over time.

To assess the effect the electric field exerts on the mass rate of carbon nanotubes and catalyst deactivation times the tests mentioned in Section 2.5.4 were performed. The results are plotted in Figure 3.19, where the data measured at 0V by [93] was also inserted for comparison. The values presented are an average of three identical trials.

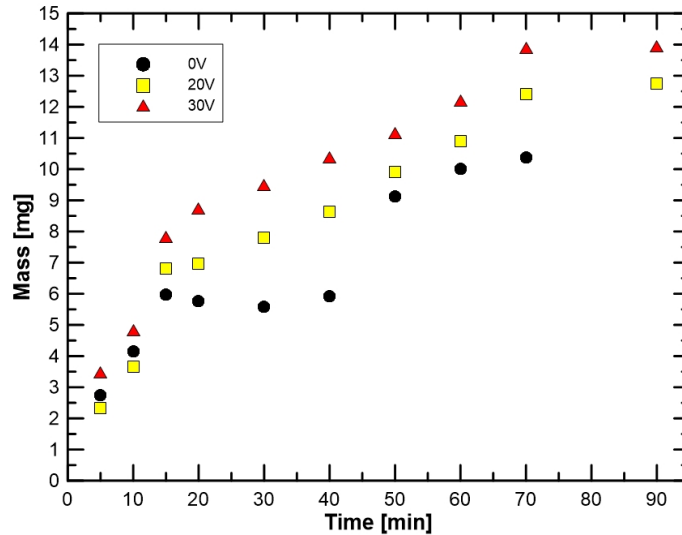


Figure 3.19: Mass measurements vs sampling time for 0, 20 and 30V.

Starting with the 0V plot, we can clearly distinguish two branches with positive mass growth rates, 0 to 15 minutes and 40 to 70 minutes. From 0 to 15 minutes the mass increased up to 5.98 mg and stagnation occurred, given that when the experiment time is 40 minutes the mass value was maintained at 5.9 mg. However, when the sampling time was increased to 50 minutes a significant mass increment was registered, to a value of 9.1 mg. Subsequent increase in sampling time yielded higher mass production until 70 minutes where the growth is ceased, with a maximum mass value of 10.1 mg.

When 20V were applied to the stainless steel substrate the mass evolution against sampling time suffered a substantial change. Until 15 minutes of flame exposure the mass production rate was high, with the mass yield registering 7 mg at 15 minutes. Contrarily to the 0V scenario, stagnation was avoided and the mass increased continuously with sampling time. The mass growth rate diminished after 15 minutes and remained fairly constant until stagnation was verified at 70 minutes. The maximum yield registered was 13.1 mg, representing a 29.7% increase compared with the previous case.

The behaviour when the bias was increased to 30V was very similar to that observed for 20V. Initially, there was mass increase with high mass growth rate until 15 minutes of sampling time, after which the production rate diminished and mass increments with higher sampling times were lower. At 70 minutes mass increase ceased. For 30V important values to register are 7.8 mg at 15 minutes and a maximum production of 14.2 mg, representing a 40.6% gain relative to no voltage.

The mass increment came as no surprise since it was observed when studying the voltage effect for a fixed sampling time. However, in the interval between 15 and 40 minutes the electric field presence is

able to maintain mass production gains with longer sampling times, while the absence of E translates to no mass increase in that interval. According to [93], the stagnation verified in that time frame occurs because of differences in the catalytic particles. In the first segment of the curve, from 0 to 15 minutes, only a small percentage of catalysts are active and produce CNT. Then, 40 minutes is the necessary period of time to activate the remaining catalyst particles with ability to synthesize CNT. For 70 minutes the catalyst activity ceases due to saturation of the particles and no diffusion of carbon is occurring. Based on a deposition area, diameter and temperature analysis, it was also concluded that with increasing sampling times the expected diameters of the carbon nanotubes decreased. This means that large carbon nanotubes are the first to be formed and are subsequently covered with smaller ones, which transduces to bigger catalytic particles being readily active while smaller ones require larger periods of time to become active. This was coincident with the observation that the absolute first nanotubes to be produced are found in the centre of the substrate, suggesting that where the temperatures are higher large catalytic particles are formed with rapid activation. The absence in mass production gains between 15 and 40 minutes is indicative of catalyst deactivation in that interval, meaning that this big particles cease activity and further CNT production is held by particles of smaller diameter.

If we recall the diameter distributions presented in Table 3.5, the expected diameter of the samples decreases with increase in applied voltage. We can conclude with the combination of the diameter change, the mass increments and higher catalytic activity during the 15 to 40 minutes interval, that voltages of 20V and 30V allow early activation of catalytic sites, meaning that even for lower sampling times the small nanotubes are already covering the bigger ones, hence why narrow expected diameters are extrapolated from the SEM images. If it is assumed that bigger catalytic particles have higher activity due to an increase of attraction forces between catalyst and carbon with particle size, the attraction induced by the electric field towards the substrate explains the early activation of smaller catalytic sites, as those need to exert less force to attract carbon. If a higher percentage of catalysts is active, it is therefore explainable why there are mass production increments and why there is no stagnation observed in the period between 15 and 40 minutes. Even if deactivation of some particles occurs at 15 minutes, there are other sites that remain active and allow growth to continue.

To better compare the results all the curves were normalized. This means that two new variables are created to which the designation of t^* and m^* was attributed. For each experiment, the former corresponds to the sampling time divided by the stagnation time registered for that condition, while the latter is the mass obtained divided by the maximum mass for that condition. For 20V and 30V the stagnation time is 70 minutes, while the maximum masses are 13.1 and 14.2 mg, respectively. Because of the different branches of the curve with 0V, these were also divided into separate normalized curves. One with a saturation time of 15 minutes involving sampling times up to 40 minutes, and the second with a saturation time of 70 minutes involving sampling times between 40 and 70 minutes. This means that the parts of the original plot where increase in production is registered can be isolated allowing a better understanding of the growth mechanism of CNT over time. The resulting plot is visible in Figure 3.20. For a complete analysis the results of the three trials performed are inserted in this graph, even though complete data for 0V was unavailable.

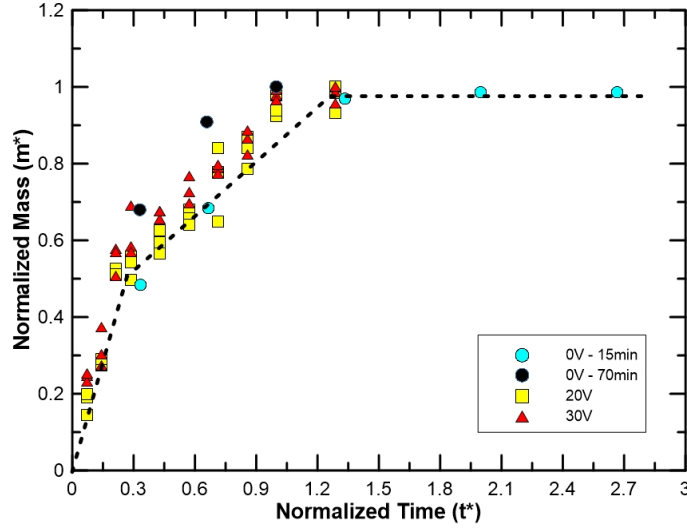


Figure 3.20: Normalized mass measurements vs sampling time for 0, 20 and 30V.

From the normalized plot a very important conclusion is withdrawn. The mechanism of mass growth rate for the different conditions lies in the same regime. The application of electric bias expands the plots, meaning that maximum mass is increased while the pathways up to those values are in agreement with each other. The values of m^* and t^* fall within a specific region for all the situations, so the mass production rates are similar. Furthermore, the plot suggests three different behaviours highlighted by the three tendencies presented. For values below $\approx 55\%$ of the maximum mass, meaning $m^* < 0.55$, the growth rate is high, i.e mass increase with sampling time is significant for the first 30% of t^* . Beyond that point the growth rate diminishes until stagnation occurs where the growth rate becomes zero as CNT production has ceased. This behaviour is coincident whether E is present or not, which is coherent with the fact that neither the temperature distribution nor the flow is affected, maintaining the fundamental characteristics of the growth process unaltered. The excess in mass is resultant of higher attraction of carbon species and earlier catalytic activity.

The growth process of carbon nanotubes has been analytically described previously. According to Bedewy et al. [108] the Gompertz model is the most suited to their results when studying the growth dynamics of a population of carbon nanotubes. The authors highlight the fact that curves based on this model have inflection points and allow the distinction between the initial high growth rates, process they name as crowding, and the moderate ones visible afterwards, in the period they describe as decay, due to decay in catalyst activity. The Gompertz model is described by Equation 3.2.

$$m(t) = \alpha e^{(-e^{-k(t-\tau)})} \quad (3.2)$$

where α is related to the asymptotic final mass growth, k is a reaction rate and finally, τ is the initial time.

The Gompertz model is widely used to describe population growth in natural environments, hence it was tested to assess the possibility of describing our growth rate results. With this model, an approximate curve could be implemented, however, it was not possible to obtain a good fit with our data. All the

possible curves did not pass through the origin of the plot, meaning that for $t^*=0$ there was already mass produced, which is physically impossible. Therefore, this model was abandoned.

In the same report it is also mentioned that for population growth dynamics the monomolecular model is widely employed. In fact, Futaba et al. [109], described the growth of a forest of carbon nanotubes using this model. This model has the disadvantage of not having inflexion points, meaning that the different regimes pointed out in Figure 3.19 are not discerned. Mathematically, the monomolecular model is described by Equation 3.3.

$$m(t) = \alpha(1 - e^{-k(t-\tau)}) \quad (3.3)$$

where again α is related to the asymptotic final mass growth, k is a reaction rate and finally, τ is the initial time.

In an attempt to describe the dynamic growth obtained with this study, the monomolecular model was also tested. An equation was found, however, it stands as a suggestion and not a definite model, since the normalized plot suggests three different growth rates with different characteristic equations. Nonetheless, with the monomolecular model the equation that best suits our data is characterized by $\alpha=0.9812$, $k=2.774$ and $\tau=0$, as per Equation 3.4. This model provides a confidence interval of 0.991. The resulting equation was plotted and the result is visible in Figure 3.21.

$$m^*(t) = 0.9812(1 - e^{-2.774t^*}) \quad (3.4)$$

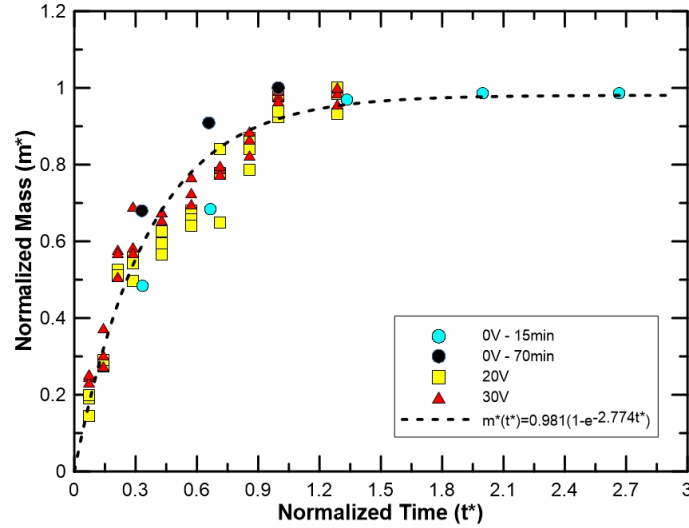


Figure 3.21: Fitment of the monomolecular analytical model to the results obtained in the experiments.

The plot suggests that the model provides good results, being coherent with the evolution obtained for the different conditions tested.

3.4.5 Deposited Substrates

In an attempt to overcome the lack of external catalyst and promote tip growth so that VACNT could be produced, two substrates were deposited with zinc and cobalt, following the procedure described in Section 2.5.4. The sampling time chosen was 10 minutes and with a positive bias of 30V.

The stainless steel plate coated with zinc yielded no nanotubes whatsoever. According to the report of Jourdain and Bichara [110], carbon affinity increases with the number of unfilled d-orbitals. Zn does not have vacancies in the d-orbitals, therefore not constituting an appropriate catalyst for carbon nanotubes production. Carbon solubility in Zn at 700°C is below 0.01%.

On the opposite hand, the substrate coated with a cobalt film provided excellent results in terms of mass production. For a sampling time of 10 minutes, the mass yield registered was 20 mg, an impressive value considering the maximum mass value for bare stainless steel was 14.2 mg for a 70 minutes trial. If we consider that some cobalt was consumed during the process, the actual mass yield might be higher than measured. This was proof that cobalt is a very good catalyst of carbon nanotubes, and that applying external catalytic materials is favourable when comparing to bare stainless steel deposition. In economical terms a study has to be performed as whether it is compensatory. The cobalt samples were analysed with SEM. In Figures 3.22 and 3.23 are presented a few of the SEM images of the cobalt coated substrates after deposition.

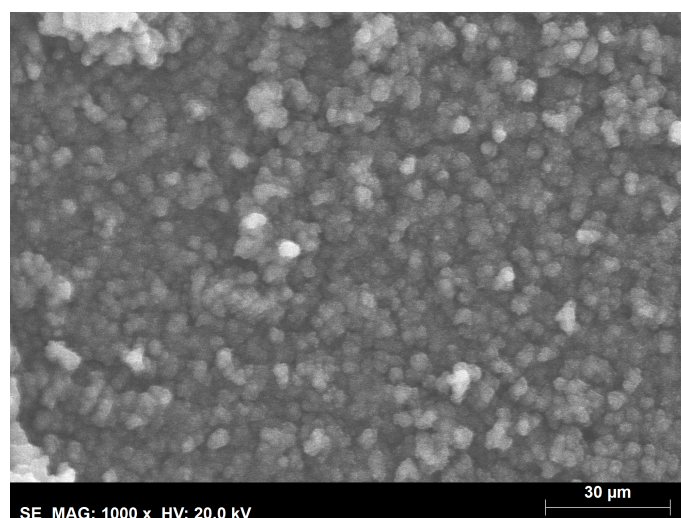


Figure 3.22: SEM image of Cobalt deposited substrate after flame exposure with 1K magnification.

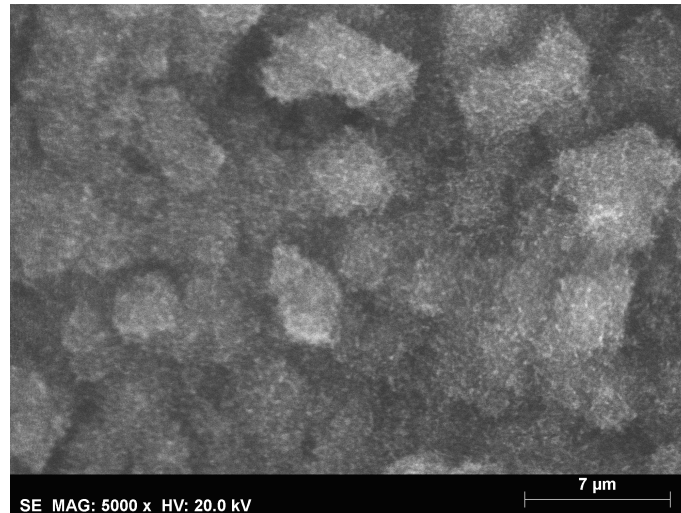


Figure 3.23: SEM image of Cobalt deposited substrate after flame exposure with 5K magnification.

There are differences between these figures and the ones presented for depositions on bare stainless steel. Tubular structures are visible and judging by the top view in Figures 3.22 and 3.23 it appears that there are elevation differences and agglomerates of CNT are formed. Again cross-section images would offer better insight on the alignment of the carbon nanotubes.

Chapter 4

Conclusions

A premixed Propane/Air flame combined with a DC electric field was used in this report to evaluate the effects that electrostatic forces have on the mass production and morphology of carbon nanotubes. Based on initial tests the flame parameters were defined, an equivalence ratio of 1.6, Reynolds number between 250 and 400 and a substrate placement at 10 mm above the burner outlet were selected. It is important to note that the Reynolds values were selected based on the ability to establish an envelope flame configuration favourable towards carbon nanotube production. The substrates employed throughout the experiments were stainless steel plates, that with the help of EDS and XRD were found to be austenitic 303L stainless steel.

The first step was to establish an appropriate basis of comparison for the synthesis with and without influence of the electric field. For the different conditions studied, $Re=250$, 300 and 400 the mass production with no voltage for a sampling time of 15 minutes was registered by averaging the results obtained from 5 consecutive trials. For $Re=300$, SEM images were captured and XRD was performed on the nanotubes, which were successfully removed from the plates to create a powder of CNT. From the SEM images an expected diameter of 60 nm was extrapolated based on a normal distribution of 60 measured diameters. The XRD analysis confirmed that the products yielded were in fact MWCNT.

The application of a DC electric field was made by charging the substrate while maintaining the burner grounded (positive bias) or vice-versa (negative bias). It is important to properly comprehend the details of the electric field applied so that appropriate conclusions can be withdrawn. With that in mind, a simulation of the electric field was computed for which a CAD model of the burner-substrate assembly was designed. It was concluded that a uniform field was created with directions according to the polarity applied. For a positive voltage, E lines point from the substrate towards the burner, following the plus to minus rule. If the polarity was reversed the electric field lines arise from the burner and point towards the substrate. Magnitudes of E utilized in this experiments range between 74.4 and 2414.3 V/m which correspond to 1 and 30 volts, respectively.

With the characterization of carbon nanotubes synthesized at 0V and the electric field defined, the effect voltage exerts on the production was investigated. Firstly, the mass production was registered for ± 1 , ± 10 , ± 20 and ± 30 V for $Re=250$, 300 and 400 and a sampling time of 15 minutes. Since every flow

has convective forces associated, these might influence the effectiveness of the electric field. Therefore low and high Reynolds numbers were studied. For $Re=250$ no mass increments were registered when applying 1 and 10V. For 20 and 30V the mass increased significantly, with a maximum increase of 84% when 30V were charging the substrate. For negative voltages no signs of significant mass gains were registered for any condition. $Re=300$ was subjected to the same analysis. When positive bias was installed and with the exception of 1V, the higher the voltage the higher the mass yield. Like the previous case, the maximum increment was obtained for 30V with a percentage gain of 75%. Negative voltages culminated in a mass gain for all the voltages applied, with mass increasing from -1V to -20V where it stagnated since at -30V the mass was the same. The increase for negative bias was lower than for positive, with a maximum percentage gain of 63.7%. Finally $Re=400$ was tested. The behaviour observed for this condition was similar to that of Reynolds 250, in the sense that charging the substrate only resulted in mass gains for 20 and 30V, with higher gains for higher voltage. 30V transduced to a 68% mass gain. Concerning the negative bias, there was no clear relationship between voltage and mass, while no significant mass gains were reported.

To explain the difference in behaviours between different Reynolds when negative voltages are applied, a comprehensive study of the deposition areas was carried out. This showed that the deposition mechanism of $Re=250$ and 400 was similar, in the way that the deposition areas consisted of a circle in the centre and an outer annular area of 3 to 5 mm thickness, while for $Re=300$ the deposition area was more uniform with CNT found in all regions comprehended between $r=0$ and $r=20$ mm. The mass increments registered from the 20 and 30 volts positive bias for $Re=250$ and 400 arose due to a change in deposition area, the circle and annular region are replaced by a uniform and completely covered area. For negative voltages this change was not present. Thus the deposition shape change and mass increments are attributed to the ability of the electric field to attract free carbonaceous negative radicals present in the flame environment towards the surface, increasing the amount of carbon available to diffuse through the catalytic particles.

SEM images were captured and diameter distributions were extrapolated for $Re=300$ with 5, 20 and 30 Volts. It was concluded that there was no apparent alignment in the nanotubes produced and that the diameter decreased with higher voltages. Seeing that the diameter of the nanotube is directly related to that of the catalytic particle, it is suggested that the electric field may influence the electron transfer responsible for the metal dusting process that forms the catalytic nanoparticles, thus influencing the diameter. Temperature and PIV measurements indicate that the presence of the electrostatic forces do not affect both the gas phase and temperature distributions, as well as the mixture flow. This leads to the conclusion that the effect on mass production results from the attraction of radicals to the substrate and not from possible changes on the flame environment. No cross section SEM images were possible to capture, however there were no hints of vertical alignment. The lack of vertical alignment was attributed to a lack of tip growth due to the absence of appropriate external catalyst, to the large dimension of deposition areas and high mass yield.

The following step was to study how the electric field acted upon the CNT production over longer sampling times. A previous study performed on the same burner and same exact working conditions

without any electrical influence served as basis of comparison. The tests were performed for 20 and 30 volts and up to 90 minutes of sampling time. Significant mass gains were obtained, although this was already expected given the previous conclusions. The CNT growth ceased at 70 minutes with 10.1 mg at 0V, 13.1 mg for 20V and 14.2 mg for 30V. The most notorious improvement was in the interval of sampling times comprehended between 15 and 40 minutes. During this interval nanotube growth ceased for the 0V condition, while the presence of electric bias allowed the mass increment with sampling time to remain continuous from 0 to 70 minutes. The author who performed the study with no voltage concluded that the expected diameter of the carbon nanotubes decreased with the sampling time, and also that the first nanotubes to be formed were the ones with larger diameters, coincident with the big catalytic particles that are formed in the centre of the sample where temperatures are the highest. The growth of these carbon nanotubes ceased at 15 minutes and only at 40 minutes there was activation of the smaller catalytic particles, synthesizing narrower nanotubes that ultimately cover the larger ones formed before. It was assumed that the bigger catalytic particles have higher carbon attraction ability and are readily available to synthesize CNT. With the results obtained with E , it seemed a logical conclusion that the attraction force the electric field exerts on carbonaceous radicals somewhat removes the necessity of the particle to attract carbon, ultimately promoting an earlier catalytic activation. This explains not only why at 15 minutes and 30V the big nanotubes are already covered with smaller ones and the expected diameter is lower, but also the continuous positive growth rate.

By normalizing mass and time dividing them by maximum mass and stagnation time, respectively, it was observed that the dynamics of the growth rates are equal whether there is E or not. The evolutions of t^* and m^* fall within a specific region and the pathway the mass follows up to the maximum value is consistent for all conditions. This enforces the conclusions that the electric field does not alter the deposition dynamics by changing temperature distributions and flow. The presence of the electric field allows earlier catalyst activity and consequent mass increments. Furthermore, an analytical monomolecular model is proposed to describe the dynamics of carbon nanotubes mass growth rates.

In a final attempt to obtain VACNT, two stainless steel plates were deposited with zinc and cobalt layers, respectively. Zinc revealed no capacity to synthesize carbon nanotubes while cobalt showed enormous potential in terms of mass yield. Despite differences in the SEM images obtained comparing to bare steel samples alignment was impossible to verify.

4.1 Achievements

The major achievements accomplished upon conclusion of this study are enumerated below:

- Production of MWCNT on a bare stainless steel substrate without use of an external catalyst.
- Successful improvement of CNT mass production via the implementation of a moderate electric field within the flame environment.
- Mass increments of up to 84% were registered when charging the supported substrate with 30V for a sampling time of 15 minutes, when comparing to synthesis without electric field.

- Proof that positive moderate voltages yield better results when comparing to negative bias.
- Based on the results obtained, it was concluded that the presence of the electric field allows earlier activation of catalytic sites by attracting carbonaceous free radicals towards the substrate, hence the increase in mass produced.
- It was demonstrated that the electric field exerts no effects on the temperature distribution in the flame environment, while also not influencing the mixture flow.
- The expected diameter of the nanotubes synthesized decreased with higher positive voltage.
- An analytical monomolecular model was suggested to describe the dynamics of CNT mass growth rates.

4.2 Future Work

Through the experiments and results presented it was concluded that moderate electric fields have a positive effect on the mass synthesis of CNT, however, alignment of the nanotubes was not observed and the following suggestions are recommended for future studies:

- Implementation of stronger fields, in the order of hundreds or thousands of volts, so that the possibility of higher benefits on mass production is evaluated and higher electrostatic forces can act on the nanotubes ultimately allowing the synthesis of VACNT.
- Extensive use of external catalysts to promote tip growth essential for the electric field to exert sufficient alignment forces and to investigate mass yield benefits.
- Experimenting with the application of a magnetic field. According to Zhang and Pan [111], the introduction of a magnetic field has the capability of aligning carbon nanotubes without the necessity of tip growth. Furthermore, improvements in the graphite crystallinity of the CNT are possible.

Bibliography

- [1] E. Comission. Nanotechnology – the invisible giant tackling europes future challenges. techreport, EU, 2013.
- [2] M. De Volder, S. Tawfick, R. Baughman, and A. J. Hart. Carbon nanotubes: Present and future commercial applications. *Science*, 339(6119):535–539, 2013.
- [3] J. Chen and X. Gao. Recent advances in the flame synthesis of carbon nanotubes. *American Journal of Materials Synthesis and Processing*, 2(6):71–89, 2017.
- [4] H. Kroto, J. Heath, S. Obrien, R. Curl, and R. Smalley. C60 : Buckminsterfullerene. *Nature*, 318(6042):162–163, 1985.
- [5] S. Iijima. Helical microtubules of graphitic carbon. *Nature*, 354(6348):56–58, 1991.
- [6] K. S. Novoselov, A. K. Geim, S. V. Morozov, D. Jiang, Y. Zhang, S. V. Dubonos, I. V. Grigorieva, and A. A. Firsov. Electric field effect in atomically thin carbon films. *Science*, 306(5696):666–669, 2004.
- [7] G. Bhat. 4 - high-performance carbon nanofibers and nanotubes. In *Structure and Properties of High-Performance Fibers*, chapter 4, pages 79–109. Woodhead Publishing, 2017.
- [8] H. Golnabi. Carbon nanotube research developments in terms of published papers and patents, synthesis and production. *Scientia Iranica*, 19(6):2012–2022, 2012.
- [9] E. T. Thostenson, Z. Ren, and T.-W. Chou. Advances in the science and technology of carbon nanotubes and their composites: a review. *Composites Science and Technology*, 61(13):1899–1912, 2001.
- [10] R. Saito, G. Dresselhaus, and M. S. Dresselhaus. *Physical Properties of Carbon Nanotubes*. Imperial College Press, 1998.
- [11] P. Kim, A. Majumdar, P. L. McEuen, and L. Shi. Thermal transport measurements of individual multiwalled nanotubes. *Phys Rev Lett*, 87(21):215502, 2001.
- [12] Q. Zhang, J.-Q. Huang, W. Qian, Y.-Y. Zhang, and F. Wei. The road for nanomaterials industry: A review of carbon nanotube production, post-treatment, and bulk applications for composites and energy storage. *Small*, 9(8):1237–1265, 2013.

- [13] Carbon nanotubes market by regional trend and growth forecast analysis 2024. [Online] <https://www.marketwatch.com/press-release/carbon-nanotubes-market-by-regional-trend-and-growth-forecast-analysis-2024-2019-03-15>, 2019. [Accessed: 23-08-2019].
- [14] M. M. J. Treacy, T. W. Ebbesen, and J. M. Gibson. Exceptionally high young's modulus observed for individual carbon nanotubes. *Nature*, 381(6584):678–680, 1996.
- [15] E. W. Wong, P. E. Sheehan, and C. M. Lieber. Nanobeam mechanics: elasticity, strength, and toughness of nanorods and nanotubes. *Science*, 277(5334):1971–1975, 1997.
- [16] M.-F. Yu, O. Lourie, M. J. Dyer, K. Moloni, T. F. Kelly, and R. S. Ruoff. Strength and breaking mechanism of multiwalled carbon nanotubes under tensile load. *Science*, 287(5453):637–640, 2000.
- [17] M.-F. Yu, B. S. Files, S. Arepalli, and R. S. Ruoff. Tensile loading of ropes of single wall carbon nanotubes and their mechanical properties. *Phys. Rev. Lett.*, 84(24):5552–5555, 2000.
- [18] M. Minary-Jolandan and M.-F. Yu. Reversible radial deformation up to the complete flattening of carbon nanotubes in nanoindentation. *Journal of Applied Physics*, 103(7):073516, 2008.
- [19] W. Merchan-Merchan, A. V. Saveliev, L. Kennedy, and W. C. Jimenez. Combustion synthesis of carbon nanotubes and related nanostructures. *Progress in Energy and Combustion Science*, 36(6):696–727, 2010.
- [20] R. Saito, M. Fujita, G. Dresselhaus, and M. S. Dresselhaus. Electronic structure of chiral graphene tubules. *Applied Physics Letters*, 60:2204, 1992.
- [21] H. Dai, E. W. Wong, and C. M. Lieber. Probing electrical transport in nanomaterials: conductivity of individual carbon nanotubes. *Science*, 272(5261):523–526, 1996.
- [22] S. Hong and S. Myung. Nanotube electronics: a flexible approach to mobility. *Nature nanotechnology*, 2(4):207–208, 2007.
- [23] Z. Han and A. Fina. Thermal conductivity of carbon nanotubes and their polymer nanocomposites: A review. *Progress in Polymer Science*, 36(7):914–944, 2011.
- [24] C. Yu, L. Shi, Z. Yao, D. li, and A. Majumdar. Thermal conductance and thermopower of an individual single-wall carbon nanotube. *Nano letters*, 5(9):1842–1846, 2005.
- [25] J. Hone, M. Llaguno, M. Biercuk, a. t. c. Johnson, B. Batlogg, Z. Benes, and J. Fischer. Thermal properties of carbon nanotubes and nanotube-based materials. *Applied Physics A*, 74(3):339–343, 2002.
- [26] S. Berber, Y.-K. Kwon, and D. Tomanek. Unusually high thermal conductivity of carbon nanotubes. *Physical Review Letters*, 84(20):4613–4616, 2000.
- [27] P. M. Ajayan, T. W. Ebbesen, T. Ichihashi, S. Iijima, K. Tanigaki, and H. Hiura. Opening carbon nanotubes with oxygen and implications for filling. *Nature*, 362(6420):522–525, 1993.

- [28] S. Tsang, P. J. F. Harris, and M. Green. Thinning and opening of carbon nanotubes by oxidation using carbon dioxide. *Nature*, 362(6420):520–522, 1993.
- [29] Y.-P. Sun, K. Fu, Y. Lin, and W. Huang. Functionalized carbon nanotubes: Properties and applications. *Acc. Chem. Res.*, 35(12):1096–1104, 2002.
- [30] D. Qian, E. C. Dickey, R. Andrews, and T. Rantell. Load transfer and deformation mechanisms in carbon nanotubepolystyrene composites. *Applied Physics Letters*, 76(20):2868, 2000.
- [31] G. Mittal, V. Dhand, K. Y. Rhee, S.-J. Park, and W. R. Lee. A review on carbon nanotubes and graphene as fillers in reinforced polymer nanocomposites. *Journal of Industrial and Engineering Chemistry*, 21:11–25, 2015.
- [32] C. Velasco-Santos, A. L. Martínez-Hernández, F. T. Fisher, R. Ruoff, and V. M. Castaño. Improvement of thermal and mechanical properties of carbon nanotube composites through chemical functionalization. *Chemistry of Materials*, 15(23):4470–4475, 2003.
- [33] A. De Vita, J.-C. Charlier, X. Blase, and R. Car. Electronic structure at carbon nanotube tips. *Applied Physics A: Materials Science and Processing*, 68(3):283–286, 1999.
- [34] K. Saeed and I. Khan. Carbon nanotubes-properties and applications: a review. *Carbon Letters*, 14(3):131–144, 2013.
- [35] E. Frackowiak and F. Beguin. Electrochemical storage of energy in carbon nanotubes and nanostructured carbons. *Carbon*, 40(10):1775–1787, 2002.
- [36] P. G. Collins, K. Bradley, M. Ishigami, and A. Zettl. Extreme oxygen sensitivity of electronic properties of carbon nanotubes. *Science*, 287:1801–1804, 2000.
- [37] C. Liu, Y. Fan, M. Liu, H. T. Cong, H.-M. Cheng, and M. S. Dresselhaus. Hydrogen storage in single-walled carbon nanotubes at room temperature. *Science*, 286(5442):1127–1129, 1999.
- [38] S.-J. Park and S.-Y. Lee. Hydrogen storage behaviors of carbon nanotubes/metal-organic frameworks-5 hybrid composites. *Carbon Letters*, 10(1):19–22, 2009.
- [39] C. L. Cheung, S. S. Wong, E. Joselevich, A. T. Woolley, and C. Lieber. Covalently functionalized nanotubes as nanometre-sized probes in chemistry and biology. *Nature*, 394(6688):52–55, 1998.
- [40] A. Durairaj and S. Basak. Carbon nanotubes (cnts) production, characterisation and its applications. *International Journal of Advances in Pharmaceutical Sciences*, 1(3):187–195, 2010.
- [41] M. Kumar. *Carbon Nanotubes Synthesis, Characterization and Applications*. IntechOpen, 2011.
- [42] R. Baker, M. Barber, P. Harris, F. Feates, and R. Waite. Nucleation and growth of carbon deposits from the nickel catalyzed decomposition of acetylene. *Journal of Catalysis*, 26(1):51–62, 1972.
- [43] R. Baker, P. Harris, R. Thomas, and R. Waite. Formation of filamentous carbon from iron, cobalt and chromium catalyzed decomposition of acetylene. *Journal of Catalysis*, 30(1):86–95, 1973.

- [44] R. Baker and R. Waite. Formation of carbonaceous deposits from the platinum-iron catalyzed decomposition of acetylene. *Journal of Catalysis*, 37(1):101–105, 1975.
- [45] J. Li, C. Papadopoulos, J. M. Xu, and M. Moskovits. Highly-ordered carbon nanotube arrays for electronics applications. *Applied Physics Letters*, 75(3):367–369, 1999.
- [46] C. Bower, O. Zhou, W. Zhu, D. J. Werder, and S. Jin. Nucleation and growth of carbon nanotubes by microwave plasma chemical vapor deposition. *Applied Physics Letters*, 77(17):2767–2769, 2000.
- [47] G. G. Tibbetts. Why are carbon filaments tubular? *Journal of Crystal Growth*, 66(3):632–638, 1984.
- [48] W. Hon Tan, S. Lee, W. Chong, and C. T. Chong. Characterization of carbon nanotubes synthesized from hydrocarbon-rich flame. *International Journal of Technology*, 7(2):343–351, 2016.
- [49] F. Geurts and A. Sacco Jr. The relative rates of the boudouard reaction and hydrogenation of co over fe and co foils. *Carbon*, 30(3):415–418, 1992.
- [50] E. T. Turkdogan and J. V. Vinters. Catalytic effect of iron on decomposition of carbon monoxide: I. carbon deposition in h₂-co mixtures. *Metallurgical Transactions*, 5(1):11, 1974.
- [51] R. Das, Z. shahnavaz, M. Ali, M. Islam, and S. B. Abd Hamid. Can we optimize arc discharge and laser ablation for well-controlled carbon nanotube synthesis? *Nanoscale Research Letters*, 11(510), 2016.
- [52] N. Arora and N. Sharma. Arc discharge synthesis of carbon nanotubes: Comprehensive review. *Diamond and Related Materials*, 50:135–150, 2014.
- [53] T. Guo, P. Nikolaev, A. Thess, D. Colbert, and R. Smalley. Catalytic growth of single-walled nanotubes by laser vaporization. *Chemical Physics Letters*, 243(1):49–54, 1995.
- [54] M. P. Kumar and Y. Ando. Chemical vapor deposition of carbon nanotubes: a review on growth mechanism and mass production. *Journal of nanoscience and nanotechnology*, 10(6):3739–3758, 2010.
- [55] N. Hamzah, M. Fairus Mohd Yasin, M. Yusop, A. Saat, and N. A. Mohd Subha. Rapid production of carbon nanotubes: A review on advancement in growth control and morphology manipulations of flame synthesis. *Journal of Materials Chemistry A*, 5(48):25144–25170, 2017.
- [56] K. A. Shah and B. A. Tali. Synthesis of carbon nanotubes by catalytic chemical vapour deposition: A review on carbon sources, catalysts and substrates. *Materials Science in Semiconductor Processing*, 41:67–82, 2016.
- [57] J. Singer and J. Grumer. Carbon formation in very rich hydrocarbon-air flames—i. studies of chemical content, temperature, ionization and particulate matter. *Symposium (International) on Combustion*, 7(1):559–569, 1958.

- [58] J. Howard, D. Chowdhury, and J. Vander Sande. Carbon shells in flames. *Nature*, 370(6491):603, 1994.
- [59] M. D. Diener, N. Nicholson, and J. M. Alford. Synthesis of single-walled carbon nanotubes in flames. *The Journal of Physical Chemistry B*, 104(41):9615–9620, 2000.
- [60] R. Vander Wal. Flame synthesis of substrate-supported metal-catalyzed carbon nanotubes. *Chemical Physics Letters*, 324(1-3):217–223, 2000.
- [61] R. L. Vander Wal, L. J. Hall, and G. M. Berger. Optimization of flame synthesis for carbon nanotubes using supported catalyst. *The Journal of Physical Chemistry B*, 106(51):13122–13132, 2002.
- [62] R. Vander Wal. Fe-catalyzed single-walled carbon nanotube synthesis within a flame environment. *Combustion and Flame*, 130(1-2):37–47, 2002.
- [63] R. Vander Wal and L. J. Hall. Ferrocene as a precursor reagent for metal-catalyzed carbon nanotubes: Competing effects. *Combustion and Flame*, 130(1-2):27–36, 2002.
- [64] R. Vander Wal, L. J. Hall, and G. M. Berger. The chemistry of premixed flame synthesis of carbon nanotubes using supported catalysts. *Proceedings of the Combustion Institute*, 29(1):1079–1085, 2002.
- [65] M. Height, J. Howard, and J. Tester. Flame synthesis of single-walled carbon nanotubes. *Carbon*, 42(11):2295–2307, 2004.
- [66] S. Nakazawa, T. Yokomori, and M. Mizomoto. Flame synthesis of carbon nanotubes in a wall stagnation flow. *Chemical Physics Letters*, 403(1-3):158–162, 2005.
- [67] C. T. Chong, W. Hon Tan, S. Lee, W. Chong, S. S. Lam, and A. Valera-Medina. Morphology and growth of carbon nanotubes catalytically synthesised by premixed hydrocarbon-rich flames. *Materials Chemistry and Physics*, 197:246–255, 2017.
- [68] K. Saito, A. S. Gordon, F. A. Williams, and W. F. Stickle. A study of the early history of soot formation in various hydrocarbon diffusion flames. *Combustion Science and Technology*, 80(1-3):103–119, 1991.
- [69] L. Yuan, K. Saito, C. Pan, F. Williams, and A. Gordon. Nanotubes from methane flames. *Chemical Physics Letters*, 340(3-4):237–241, 2001.
- [70] L. Yuan, K. Saito, W. Hu, and Z. Chen. Ethylene flame synthesis of well-aligned multi-walled carbon nanotubes. *Chemical Physics Letters*, 346(1):23–28, 2001.
- [71] V. W. Randall L., T. Thomas M., and C. Valerie E. Diffusion flame synthesis of single-walled carbon nanotubes. *Chemical Physics Letters*, 323(3):217–223, 2000.

- [72] W. Hu, L. Yuan, Z. Chen, D. Gong, and K. Saito. Fabrication and characterization of vertically aligned carbon nanotubes on silicon substrates using porous alumina nanotemplates. *Journal of Nanoscience and Nanotechnology*, 2(2):203–207, 2002.
- [73] T. Li, K. Kuwana, K. Saito, H. Zhang, and Z. Chen. Temperature and carbon source effects on methane–air flame synthesis of cnts. *Proceedings of the Combustion Institute*, 32(2):1855–1861, 2009.
- [74] J. Camacho and A. Choudhuri. Effects of fuel compositions on the structure and yield of flame synthesized carbon nanotubes. *Fullerenes Nanotubes and Carbon Nanostructures*, 15(2):99–111, 2007.
- [75] W. Merchan-Merchan, A. Saveliev, L. A. Kennedy, and A. Fridman. Formation of carbon nanotubes in counter-flow, oxy-methane diffusion flames without catalysts. *Chemical Physics Letters*, 354(1):20–24, 2002.
- [76] W. Merchan-Merchan, A. V. Saveliev, and L. A. Kennedy. Metal catalyzed synthesis of carbon nanostructures in an opposed flow methane oxygen flame. *Combustion and Flame*, 135(1):27–33, 2003.
- [77] T. Li, H. Zhang, F. Wang, Z. Chen, and K. Saito. Synthesis of carbon nanotubes on ni-alloy and si-substrates using counterflow methane–air diffusion flames. *Proceedings of the Combustion Institute*, 31(2):1849–1856, 2007.
- [78] G. W. Lee, J. Jurng, and J. Hwang. Formation of ni-catalyzed multiwalled carbon nanotubes and nanofibers on a substrate using an ethylene inverse diffusion flame. *Combustion and Flame*, 139(1):167–175, 2004.
- [79] F. Xu, H. Zhao, and S. D. Tse. Carbon nanotube synthesis on catalytic metal alloys in methane/air counterflow diffusion flames. *Proceedings of the Combustion Institute*, 31(2):1839–1847, 2007.
- [80] C. Unrau, R. Axelbaum, P. Biswas, and P. Fraundorf. Synthesis of single-walled carbon nanotubes in oxy-fuel inverse diffusion flames with online diagnostics. *Proceedings of the Combustion Institute*, 31(2):1865–1872, 2007.
- [81] S.-S. Hou, W.-C. Huang, and T.-H. Lin. Flame synthesis of carbon nanostructures using mixed fuel in oxygen-enriched environment. *Journal of Nanoparticle Research*, 14(11):1243, 2012.
- [82] A. Moisala, A. Nasibulin, and E. Kauppinen. The role of metal nanoparticles in the catalytic production of single-walled carbon nanotubes — a review. *Journal of Physics Condensed Matter*, 15(3):3011–3035, 2003.
- [83] J. P. Gore and A. Sane. *Flame Synthesis of Carbon Nanotubes*, chapter 7. IntechOpen, 2011.
- [84] W. Merchan-Merchan, A. V. Saveliev, and L. A. Kennedy. High-rate flame synthesis of vertically aligned carbon nanotubes using electric field control. *Carbon*, 42(3):599–608, 2004.

- [85] G. I. Taylor and M. D. Van Dyke. The force exerted by an electric field on a long cylindrical conductor. *Proceedings of the Royal Society of London. Series A. Mathematical and Physical Sciences*, 291(1425):145–158, 1966.
- [86] W. Merchan-Merchan, A. V. Saveliev, and L. A. Kennedy. Flame nanotube synthesis in moderate electric fields: From alignment and growth rate effects to structural variations and branching phenomena. *Carbon*, 44(15):3308–3314, 2006.
- [87] F. Xu, X. Liu, and S. D. Tse. Synthesis of carbon nanotubes on metal alloy substrates with voltage bias in methane inverse diffusion flames. *Carbon*, 44(3):570–577, 2006.
- [88] Q. Bao and C. Pan. Electric field induced growth of well aligned carbon nanotubes from ethanol flames. *Nanotechnology*, 17(4):1016–1021, 2006.
- [89] B. M. Sun, W. H. Cao, Y. H. Guo, Y. Wang, J. T. Luo, and P. Jiang. Flame pyrolysis synthesis of self-oriented carbon nanotubes. *AIP Advances*, 3(9):092102, 2013.
- [90] M. Raffel, C. Willert, and J. Kompenhans. *Particle Image Velocimetry: A Practical Guide*. Springer, 1998.
- [91] A. Melling. Tracer particles and seeding for particle image velocimetry. *Measurement Science and Technology*, 8(12):1406, 1997.
- [92] D. S. Jayakrishnan. Electrodeposition: the versatile technique for nanomaterials. In *Corrosion Protection and Control Using Nanomaterials*, pages 86–125. Woodhead Publishing, 2012.
- [93] A. F. K. Duarte. Mass analysis of carbon nanotubes synthesized by impinging flames. Master’s thesis, Instituto Superior Tecnico, 2019.
- [94] E. Fernandes and R. Leandro. Modeling and experimental validation of unsteady impinging flames. *Combustion and Flame*, 146(4):674–686, 2006.
- [95] E. W. Lemmon, R. T. Jacobsen, S. G. Penoncello, and D. G. Friend. Thermodynamic properties of air and mixtures of nitrogen, argon, and oxygen from 60 to 2000 k at pressures to 2000 mpa. *Journal of Physical and Chemical Reference Data*, 29(3):331–385, 2000.
- [96] D. Bradley and K. J. Matthews. Measurement of high gas temperatures with fine wire thermocouples. *Journal of Mechanical Engineering Science*, 10(4):299–305, 1968.
- [97] M. Heitor, A. Taylor, and J. Whitelaw. Simultaneous velocity and temperature measurements in a premixed flame. *Experiments in Fluids*, 3(6):323–339, 1985.
- [98] Analytical balance abt. [Online] <https://www.kern-sohn.com/shop/en/laboratory-balances/analytical-balances/ABS-N/ABJ-NM/>, 2018. [Accessed: 02-10-2019].
- [99] M. Dadfar, M. Fathi, F. Karimzadeh, M. Dadfar, and A. Saatchi. Effect of tig welding on corrosion behavior of 316l stainless steel. *Materials Letters*, 61(11):2343–2346, 2007.

- [100] A. Cao, C. Xu, J. Liang, D. Wu, and B. Wei. X-ray diffraction characterization on the alignment degree of carbon nanotubes. *Chemical Physics Letters*, 344(1):13–17, 2001.
- [101] E. Plaza, H. Briceño, J. Arevalo-Fester, R. Atencio, and L. Corredor. Electric field effect in the growth of carbon nanotubes. *Journal of Nanoparticle Research*, 17(6):1–11, 2015.
- [102] M. Hashempour, A. Vicenzo, F. Zhao, and M. Bestetti. Direct growth of mwcnts on 316 stainless steel by chemical vapor deposition: Effect of surface nano-features on cnt growth and structure. *Carbon*, 63:330–347, 2013.
- [103] D. J. Young, J. Zhang, C. Geers, and M. Schütze. Recent advances in understanding metal dusting: A review. *Materials and Corrosion*, 62(1):7–28, 2011.
- [104] P. Szakalos. *Mechanisms of Metal Dusting*. KTH, 2004.
- [105] M. V. Kharlamova. Investigation of growth dynamics of carbon nanotubes. *Beilstein Journal of Nanotechnology*, 8:826–856, 2017.
- [106] K. Masunaga, H. Ito, and O. Fujita. Investigation of applying dc electric field effect on carbon nanotube synthesis. *Asia-Pacific Journal of Chemical Engineering*, 8(2):246–253, 2013.
- [107] Y. Gan, M. Wang, Y. Luo, X. Chen, and J. Xu. Effects of direct-current electric fields on flame shape and combustion characteristics of ethanol in small scale. *Advances in Mechanical Engineering*, 8(1), 2016.
- [108] M. Bedewy, E. R. Meshot, M. J. Reinker, and A. J. Hart. Population growth dynamics of carbon nanotubes. *ACS Nano*, 5(11):8974–8989, 2011.
- [109] D. Futaba, K. Hata, T. Yamada, K. Mizuno, M. Yumura, and S. Iijima. Kinetics of water-assisted single-walled carbon nanotube synthesis revealed by a time-evolution analysis. *Physical review letters*, 95(5):056104, 2005.
- [110] V. Jourdain and C. Bichara. Current understanding of the growth of carbon nanotubes in catalytic chemical vapour deposition. *Carbon*, 58:2–39, 2013.
- [111] J. Zhang and C. Pan. Magnetic-field-controlled alignment of carbon nanotubes from flames and its growth mechanism. *The Journal of Physical Chemistry C*, 112(35):13470–13474, 2008.

Appendix A

Velocity Plots

In this appendix the remaining velocity plots obtained from PIV measurements are presented.

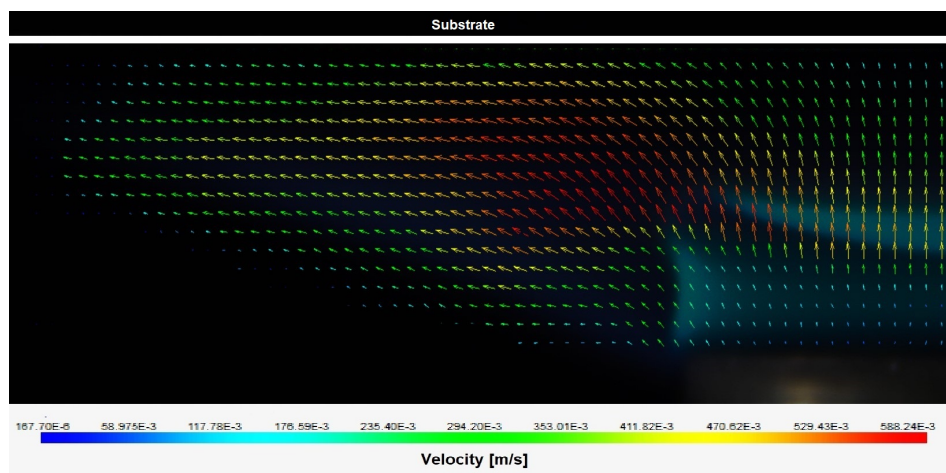


Figure A.1: 2D velocity plot obtained from PIV for 1V.

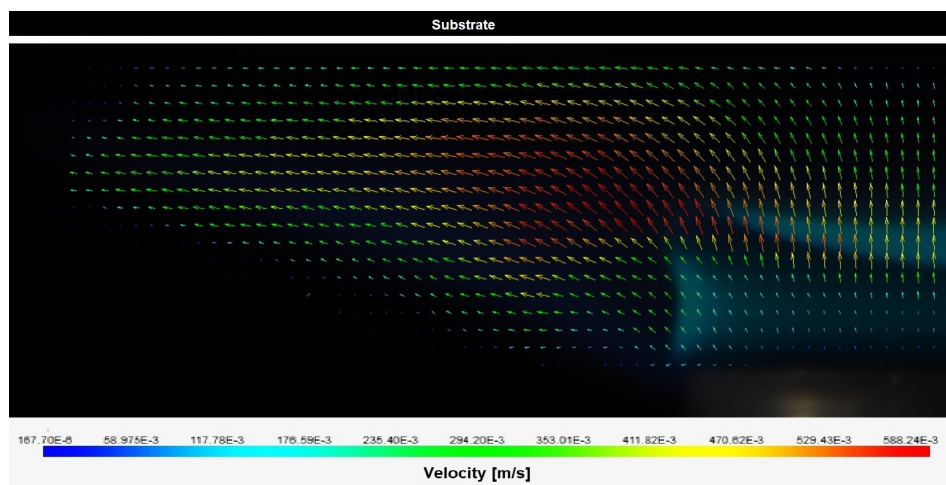


Figure A.2: 2D velocity plot obtained from PIV for 10V.

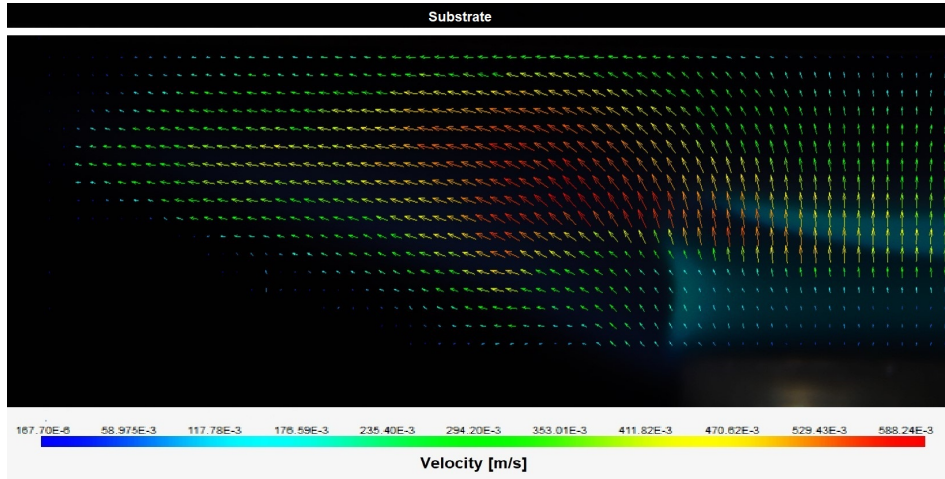


Figure A.3: 2D velocity plot obtained from PIV for 20V.

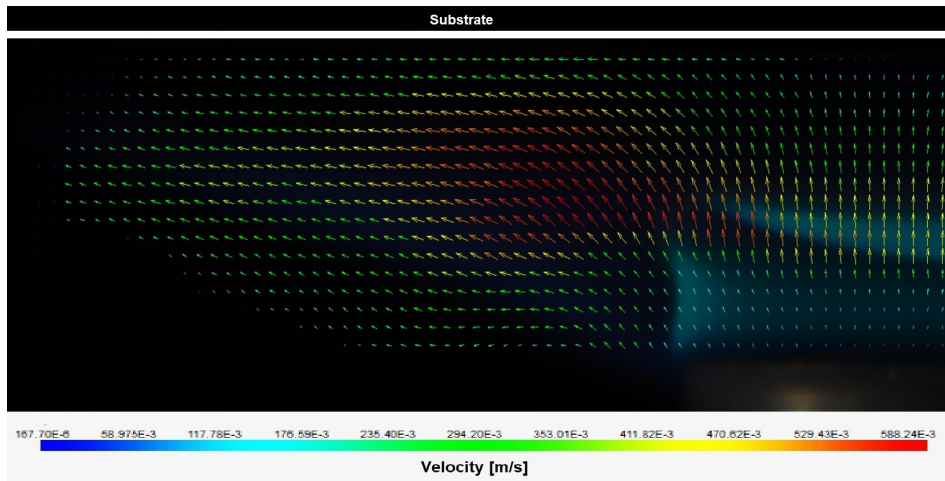


Figure A.4: 2D velocity plot obtained from PIV for -1V.

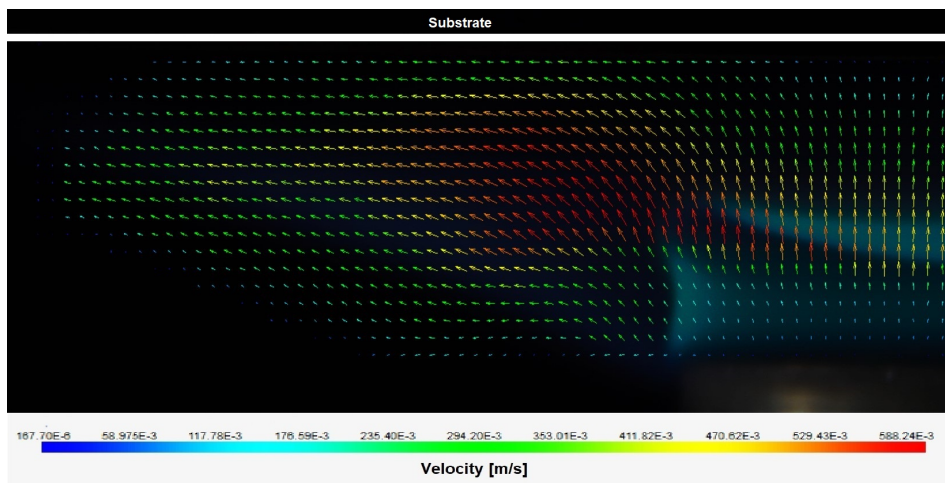


Figure A.5: 2D velocity plot obtained from PIV for -10V.

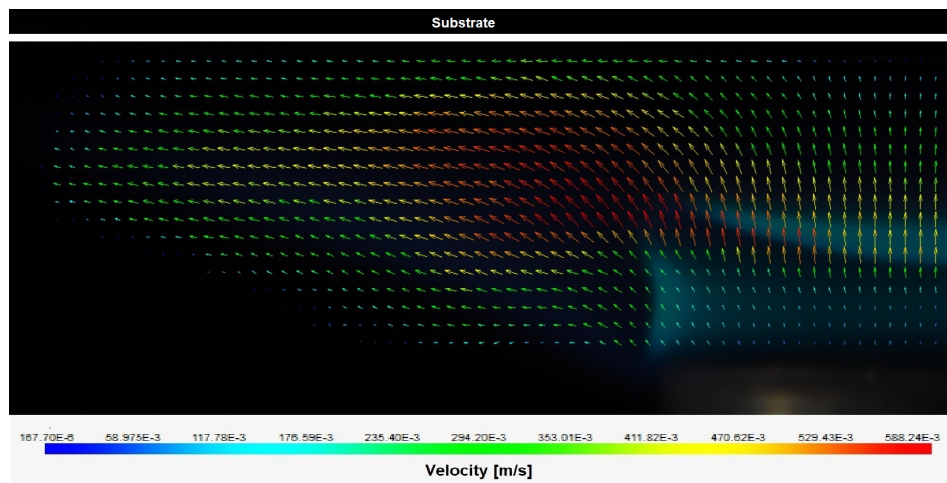


Figure A.6: 2D velocity plot obtained from PIV for -20V.

